UNIVERSITY OF CALIFORNIA
RIVERSIDE

Development and Application of Dispersion Models to Understand the Impact of Sources of Air Pollution

A Dissertation submitted in partial satisfaction
of the requirements for the degree of

Doctor of Philosophy

in

Mechanical Engineering

by

Yifan Ding

December 2023

Dissertation Committee:
Dr. Akula Venkatram, Chairperson
Dr. Bhargav Rallabandi
Dr. Marko Princevac

The Dissertation of Yifan Ding is approved:

_____

_____

_____

Committee Chairperson

University of California, Riverside

ACKNOWLEDGEMENTS

I would like to express my deepest gratitude and appreciation to the many people who have supported and guided me throughout the course of my research and the completion of this thesis. First and foremost, I want to thank my advisor, Dr. Akula Venkatram, for his technical support, career guidance, and essential resources. Additionally, I have learned invaluable lessons from him, including strong work ethics, meticulous research skills, and exceptional communication abilities, all of which have been integral to the completion of this dissertation. Without his guidance and assistance, this dissertation would have been not possible.

I thank my committee members, Dr. Bhargav Rallabandi and Dr. Marko Princevac, who not only taught me the practical application of turbulence theory, but also emphasizing the significance of understanding the fundamental of a subject.

I would like to express my very great appreciation to my parents Bo Ding, and Xiaomei Yuan for their encouragement, understanding, support, and love. Without their dedication, reaching the end of this road would have been impossible.

I would like to thank my colleague and friend Dr. Ranga Rajan Thiruvenkatachari. We spent countless hours during field measurements, lab analysis, meetings, and conferences. I want to extend my thanks to Dr. Javier Gonzalez-Rocha for his strong leadership and management work in the projects. I would like to thank Dr. Faraz Enayati Ahangar who answered my questions and provided lab resources. I would like to offer my special thanks to my student and friend Hongpufan Huang for his invaluable assistance during our field work. I wish to convey my deepest appreciation to

Dr. Francesca Hopkins, Dr. Roya Bahreini, Dr. Frank Freedman, Dr. Guoyuan Wu, Dr. Manvendra Dubey, and Dr. Seongeun Jeong for their constructive suggestions on my research. I also thank Dave Pankratz, Sajjan Heerah, Dr. Isis Frausto-Vicencio, Amir Saeidi, Bradley Ries, Sergio Beltran, Michelle Carr, Dr. Susan O'Neill, Dr. Sean Raffuse, Dr. Alison R. Marklein, Dr. Ji Luo, Dr. Nidia Rojas Robles, Dr. Peggy A Mauk, Alondra Moreno, and Isa Cruz for their important help with field work and resources.

The research in chapter 2 was supported by the NASA Health and Air Quality Applied Science Team (HAQAST) with Contract No: NNX16AQ91G. The research in chapter 3 was supported by the University of California Office of the Presidents Grant LFR 18-548581, Contractor Supporting Research (CSR) funding from Berkeley Lab, provided by the Director, Office of Science, under Contract No.DE-AC02-05CH11231 with the U.S. Department of Energy. The research in chapter 4 was supported by the Center for Advancing Research in Transportation Emissions, Energy, and Health (CARTEEH), project number 05-49-UCR. The research in chapter 5 was supported by the California Department of Transportation (CALTRANS), and we acknowledge and are thankful for the support from the South Coast Air Quality Management District (SCAQMD) and UCR Agricultural Operations (Ag-Ops).

The text in chapter 2 of this dissertation is in part a reprint as it appears in Ding, Y., Cruz, I., Freedman, F., Venkatram, A., 2021b. Improving spatial resolution of PM2.5 measurements during wildfires. Atmos. Pollut. Res. 12, 101047. https://doi.org/10.1016/j.apr.2021.03.010.

The text in chapter 4 of this dissertation is in part a reprint as it appears in Ding, Y., Zhao, X., Luo, J., Wu, G., Venkatram, A., 2022. Field Study to Estimate Exposure to Vehicle Exhaust During Idling and Starting. Atmos. Pollut. Res. 14, 101632. https://doi.org/10.2139/ssrn.4063435.

ABSTRACT OF THE DISSERTATION

Development and Application of Dispersion Models to Understand the Impact of Sources of Air Pollution

by

Yifan Ding

Doctor of Philosophy, Graduate Program in Mechanical Engineering
University of California, Riverside, December 2023
Dr. Akula Venkatram, Chairperson

Atmospheric dispersion models play a critical role in the management of air quality. They are used to estimate the impact of sources of air pollutants on air quality. They are also used to infer emissions from sources from measurements of pollutant concentration. Regulatory agencies used air quality models to determine whether existing or proposed industrial facilities comply with regulatory requirements.

In my research, I developed a class of dispersion models to study four problems. I developed two Lagrangian dispersion models to estimate emissions of wildfires using data from PM monitoring networks and the High-Resolution Rapid Refresh (HRRR) meteorological model. By integrating data from ground-based monitors and NASA's Moderate Resolution Imaging Spectroradiometer (MODIS), I created a comprehensive model that enables improved spatial and temporal resolution for assessing $PM_{2.5}$

concentrations during wildfires. This integrated technology, capable of evaluating concentrations at 1 km spatial resolution with 1 hour temporal resolution, has significant implications for health risk assessment, evacuation planning, and policy development related to wildfire impacts.

I next demonstrated the application of a dispersion model to estimate emissions of methane (CH_4) using total column measurements from four field campaigns conducted in the San Joaquin Valley of California during four seasons from March 2019 until January 2020. The atmospheric column dry mixing ratios of CH_4 were retrieved from multiple EM27/SUN solar spectrometers deployed upwind and downwind of a cluster of dairy farms. These measurements were complemented with satellite observations of column-averaged CH_4 from the S5P/TROPOMI satellite instrument over the same area to extend the analysis to larger scales and periods.

The next study involved the development and application of a model to estimate the impact of vehicle tailpipe emissions on people waiting next to idling vehicles. We conducted a field study designed to collect CO_2 concentration data at distances of a few meters from the tailpipe of a vehicle: the accelerator pedal was controlled to simulate idling and acceleration from a stop. Analysis of the data shows that the measurements are described within a factor of two with a dispersion model that uses micrometeorological variables as inputs and includes plume rise associated with the buoyancy of the exhaust plume. The data suggest that people situated a few meters from an idling vehicle are likely to be exposed to levels of NO_2 that are above the Clean Air Act 1-hour standard of 100 ppb.

The final study examined the application of a dispersion model to estimate PM_{10} emissions from roads. This involved sampling silt loadings on roads using a mobile dust collection system that I helped to design and build. The sampling was conducted on two freeways and two city roads in Riverside, California. PurpleAir PM monitors and PICARRO CO_2 monitors were deployed on the mobile platform to measure road dust concentrations, which was then used to infer emission factors with a line source dispersion model, and carbon mass balance approach. The results indicated that freeways have lower emission factors compared to the city roads. The data from the field studies was used to propose a new model for emission factors, which improves upon the currently used regulatory model.

Table of Contents

List of Figures

List of Tables

1. Background, Motivation, and Objective

This thesis addresses the application of dispersion models to four different problems related to air quality. This chapter provides the motivation for studying these problems and states the objectives of the associated research. Details of the research conducted to accomplish these objectives are described in subsequent chapters. Each of these problems involved adapting existing models or developing new dispersion models. This required evaluating these models with available data or data collected in field studies in which I played an active role.

1.1 Improving Spatial Resolution of $PM_{2.5}$ Measurements during Wildfires

U.S. Environmental Protection Agency (EPA) sets National Ambient Air Quality Standards (NAAQS) for six pollutants, including particulate matter, ozone, carbon monoxide, sulfur dioxide, nitrogen dioxide, and lead (US EPA, 2023a). These pollutants can harm public health and the environment. The Clean Air Act delineates two categories of national ambient air quality standards. Primary standards are designed to safeguard public health, with a focus on protecting "sensitive" populations, such as individuals with asthma, children, and the elderly. The secondary standards aim to safeguard public welfare, addressing concerns such as diminished visibility and potential harm to animals, crops, vegetation, and buildings. Large wildfires pose a significant threat to air quality, endangering public health by releasing harmful substances found in wildfire smoke, primarily fine particulate matter ($PM_{2.5}$) which is one of the criteria pollutants (Fann et

al., 2018). Exposure to over standard $PM_{2.5}$ can cause adverse health effects such as cardiovascular diseases, lung cancer, asthma and so on (Youssouf et al., 2014).

To effectively monitor and predict the impact of wildfire smoke on air quality, it is crucial to assess $PM_{2.5}$ concentration levels. The U.S. Clean Air Act (CAA) requires nationwide monitoring compliance monitors for PM must be officially classified as either Federal Reference Methods (FRMs) or Federal Equivalent Methods (FEMs) (US EPA, 2019). These regulatory monitoring networks have poor spatial resolution, and they are typical expensive to establish (Levy Zamora et al., 2019).

The Moderate Resolution Imaging Spectroradiometer (MODIS), situated on the TERRA and AQUA satellites in polar orbits, were launched in 2000 and 2002, respectively. MODIS supply daily data on AOD, extensively employed to enhance spatial coverage in the estimation of ground-level $PM_{2.5}$ concentrations. AOD represents the column-integrated sum of total ambient particle extinction and is notably correlated with surface $PM_{2.5}$ (Liu et al., 2005). Many studies have applied statistical models using AOD to predict PM2.5 concentrations and yielded high linear correlation (Geng et al., 2018). MODIS AOD products could provide 3-10 km spatial resolution (Li et al., 2020). Multi-Angle Implementation of Atmospheric Correction MAIAC retrieval products provides an advanced algorithm for gridding MODIS AOD measurements to improve accuracy of cloud detection aerosol retrievals and atmospheric correction (Lyapustin et al., 2011). Each daily MAIAC file (MCD19A2) contains gridded AOD retrievals from both Terra and Aqua and the product shows good accuracy within 1 km resolution (Lyapustin and Wang, 2018). Satellite remote sensing provides Aerosol Optical Depth (AOD) to estimate

$PM_{2.5}$ concentrations in areas not covered by ground-level monitors (Hoff and Christopher, 2009). The column integrated value measured by AOD divided by the boundary layer height is likely to be correlated with the surface $PM_{2.5}$ concentration if material is well mixed through the depth of the boundary layer (Liu et al., 2005).

However these daily observations are roughly five-minute snapshots occurring around 1030 local sidereal time (LST) for Terra observations, and around 13:30 LST for Aqua observations, and only are available for cloud-free conditions. Since ground-based monitors provide limited spatial coverage, while satellite observations, being five-minute snapshots only available for cloud free pixels, is not consistently available to follow the time evolution of the ground-level impact of wildfire plumes (Sifakis et al., 2003). Because of limited spatial resolution of ground monitoring networks and limited temporal resolution of satellite observations for $PM_{2.5}$ information during wildfires, several studies have been conducted to create high spatial resolution maps for particulate matter during wildfires. Wu et al. (2006) estimated daily particulate matter concentrations at a zip-code level for southern California and assigned valid estimated PM concentrations at air quality stations to the created smoke polygon. Gupta et al. (2018) used multiple regression method to predict and interpolate the concentration by fitting over 3000 of satellite observed AOD and low-cost sensors measured $PM_{2.5}$ pairs at the nearest locations.

The previous studies applied the purely statistical method to improve the spatial resolution of surface PM concentrations. There exists a need for a method including the

underlying physical plume structure that can evaluate health risks associated with wildfires at the community level, offering enhanced spatial and temporal resolution.

This thesis aims to address this gap by integrating ground monitor measurements with satellite observations using dispersion models. This integrated technology can assess $PM_{2.5}$ concentrations at 1 ×1 km grid with 1 hour temporal resolution, enabling better evaluation of health risks and offering the potential for predicting wildfire impacts to aid in public health assessment and wildfires management.

1.2 Quantifying and Monitoring Methane Emissions from Dairy Farms in California Using TROPOMI and EM27/SUN Measurements

The environmental community appropriately identifies global warming as a significant threat to the planet. Atmospheric methane (CH_4), a greenhouse gas contributing to global warming, is emitted from various sources and it has increased by 150% since preindustrial times, causing the second largest radiative forcing of the long-lived greenhouse gases after carbon dioxide (IPCC, 2013; Karakurt et al., 2012). Increased anthropogenic emissions now account for 50 to 65% of the total emissions (IPCC, 2013), which are likely to be part of the reasons for the renewed rise since 2007 (Kirschke et al., 2013; Luther et al., 2019; Saunois et al, 2016b). CH_4 emissions from agriculture and waste are estimated at 195 Tg/yr globally, accounting for 57% of total anthropogenic emissions (Saunois et al., 2016a). Inventory of greenhouse gas (GHG) emissions suggests that CH_4 emissions increase by 16% between 2000 and 2015 in California (CARB, 2020). The state of California has taken legislative action to address

this issue with Senate Bill 1383, which mandates the reduction of livestock manure methane emissions below 2013 levels by 2030 (CARB, 2016a).

Several methods to estimate methane emissions from dairy facilities are based on atmospheric column measurements. Gisi et al. (2012) illustrated the use of compact solar-tracking Fourier transform spectrometers (EM27/SUN) for measurements of the column-averaged dry-air mole fractions of CH_4. Since the entire atmospheric column is measured, column-averaged measurements are believed to be less sensitive to vertical and near-surface transport of methane that affect interpretation of point methane concentrations (Heerah et al., 2021; Lauvaux and Davis, 2014). Solar column gradients have been utilized previously to assess CH_4 emissions from dairy farms in Southern California through the application of the differential column measurement technique using EM27/SUN (Chen et al., 2016; Viatte et al., 2017). Chen et al. (2016) employed multiple solar column instruments to mitigate the impact of long-range influences through simultaneous measurements at upwind and downwind locations within urban scales and applied mass balance approach to verify the inventory emissions. Viatte et al. (2017) measured the differential CH_4 from four EM27/SUN and assessed the fluxes of the dairies using the mass balance approach and high resolution WRF-LES simulations.

The TROPOspheric Monitoring Instrument (TROPOMI) serves as the satellite instrument aboard the Copernicus Sentinel-5 Precursor satellite launched in October 2017, which can measure a wide range of atmospheric pollutants including nitrogen dioxide (NO_2), ozone (O_3), sulfur dioxide (SO_2), and methane (CH_4). TROPOMI measures the column-averaged gas concentration using backscattered sunlight in the

shortwave-inferred (SWIR) spectral range (Butz et al., 2012). TROPOMI provides daily global measurements at approximately 13:30 local solar time. The spatial resolution provided by TRPOMI was 7×7 km^2 during the first part of the study and was then to upgraded to 5.5×7 km^2 after August 2019 (Siddans and Smith, 2018). Lorente et al. (2021) and Hasekamp et al. (2019) have assessed the global mean bias and station-to-station variability between TROPOMI and the ground-based Total Carbon Column Observing Network (TCCON). The estimated CH_4 values are -3.4 ± 5.6 ppb and -4.3 ± 7.4 ppb, respectively. Despite challenges such as hazy atmospheres or low surface reflectance limiting the usefulness of only 3% of the data over land (Jacob et al., 2022), TROPOMI measurements have been employed in various studies to estimate CH_4 emissions (Qu et al., 2021; Varon et al., 2019).

However, current models used to infer emissions from column measurements make assumptions about the wind fields and source geometry lead to high uncertainty in the corresponding emission estimates (Chen et al., 2016; Jacob et al., 2016). There is a need to reduce these uncertainties in currently used methods by including considerations of the geometry of sources, the geometry of column measurements, and governing micrometeorological conditions. My research addresses this need by developing and applying a method based on dispersion models to estimate dairy farms methane emissions for the column measurements.

1.3 Field Study to Estimate Exposure to Vehicle Exhaust During Idling and Starting

Exposure to vehicle pollutants including carbon monoxide (CO), particulate matter (PM), nitrogen oxides (NO_x), black carbon (BC), and volatile organic compounds

(VOCs) has been linked to a range of adverse health effects. such as cardiovascular morbidity, asthma, respiratory illnesses, lung function and chronic obstructive pulmonary disease (HEI, 2010; Laumbach et al., 2012). Several studies have been conducted to examine the impact of vehicle emissions on roadways. Heist et al. (2009) conducted wind tunnel studies to examine the effect of different road configurations including noise barriers on the dispersion of traffic related pollution and observed a reduction in the pollution when a barrier was present. A tracer gas study conducted by Finn et al. (2010) examined the effect of noise barriers by simulating roadway emissions using a line source releasing a tracer gas and observed reduction of up to 80%. Schulte et al., (2014) developed two semi-empirical models to explain the effect of downwind solid barriers. Thiruvenkatachari et al. (2022) conducted the real-world tracer gas field studies to estimate the dispersion of vehicular emissions for downwind barrier case. These studies have led to the development of dispersion models like RLINE and CALINE, used to estimate how new road construction affects local air quality (Kenty et al., 2007; Snyder et al., 2013; Yura et al., 2007).

Limited studies have explored the dispersion of vehicle emissions within a few meters from stationary vehicles. Deng et al., (2020) found that vehicle-induced turbulence becomes more significant with increasing ambient wind speed, leading to 2.6-3 times higher particle exposure for pedestrians 3 m away from the vehicle. Ning et al. (2005) observed rapid concentration drops within 5 m from an idling vehicle, attributing it to turbulence induced by exhaust momentum and buoyancy. McNabola et al. (2009) supported these findings in a congested traffic study, using a CFD model to confirm a

quick decrease in exhaust concentrations to background levels within 3 m from the source.

The existing dispersion models employed for estimating the impact of road traffic, such as RLINE and CALINE, have not investigated areas within a few meters of vehicle exhaust sources. This is crucial for people near idling or accelerating vehicles. Frequently encountered exposure scenarios include children waiting at school pick-up points, pedestrians at traffic intersections, and individuals awaiting ride-sharing services. Therefore, there is a need to conduct a field study to collect the data required to evaluate the performance of existing dispersion models in estimating the near-source impact of emissions from stationary idling vehicles in varying atmospheric conditions. In summary, the objective of my research is to design and conduct a field study that focuses on dispersion at scales of a few meters from a source of buoyant emissions, and adapt and improve, if necessary, current models to describe data from the field study.

1.4 An Assessment of Paved Road Dust Emissions Modeling

Particulate matter (PM) is one of the six criteria air pollutants established by U.S. EPA, consisting of solid particles and liquid droplets suspended in the air (US EPA, 2023b). PM emissions from roadway can be classified as exhaust emissions and non-exhaust emissions (also called road dust). Recent studies show a growing trend in the contribution of road dust to roadway PM concentrations (S. Reid et al., 2016), which emphasizes the need for accurately quantifying the road dust emissions. Numerous studies have been conducted to try to distinguish the exhaust emissions and non-exhaust emissions. Matthaios et al. (2022) used the PMF method with mobile platform

measurements to suggest that non-exhaust sources can account for 65.6% of the $PM_{10-2.5.}$ Harrison et al. (2012) also conducted the study to integrate size distribution and tracer elements to distinguish brake dust, tire dust, and resuspension, and these non-exhaust sources contribute to 104.1% of $PM_{10-2.5}$ mass in traffic. These evidences support the assumption made in chapter 5 that road dust is the primary contributor to $PM_{10-2.5}$ size fraction emissions.

The U.S. Clean Air Act (CAA) requires nationwide monitoring compliance monitors for PM must be officially classified as either Federal Reference Methods (FRMs) or Federal Equivalent Methods (FEMs) (US EPA, 2019). Since the regulatory PM monitoring networks are impractical to deploy near road ways, low-cost PM sensors can help us overcome this challenge (Kumar et al., 2015). They have the advantages of easy deployment on mobile platforms or any road sections, with relatively low power consumption for monitoring purposes. However, the accuracy and precision of the low-cost monitors remain a concern (Kuula et al., 2017). Kelly et al. (2017) and Morawska et al. (2018) conducted the outer-calibration with low-cost sensors and FEM/FRM instruments. A multi-variable regression approach has been used to calibrate the low-cost sensors with the parameters including raw sensor measurements, ambient temperature, and relative humidity measurements (Barkjohn et al., 2021; Le et al., 2020).

The currently used regulatory model to estimate emissions of road dust is described in “Compilation of Air Pollutant Emissions Factors” (AP-42) and published by U.S. Environmental Protection Agency (EPA). First formulated in 1968, it is routinely updated with new versions (US EPA, 2011a). This semi-empirical road dust model has

been widely used by worldwide researchers for decades (Bogacki et al., 2018; Bukowiecki et al., 2010; Chen et al., 2019), but also criticized due to its uncertainty, impracticality, and safety issues associated with collecting input data for the model. (Fitz et al., 2020; Venkatram et al., 1999; Zhang et al., 2017).

The objective of my research is to develop a model for paved road dust emission factors that improves upon the current AP-42 model for estimating emission factors of road dust for California freeways with high traffic volume. The model is based on data collected in field studies that I helped to design and implement.

2. Improving Spatial Resolution of $PM_{2.5}$ Measurements during Wildfires

2.1 Introduction

Large wildfires deteriorate air quality, adversely affecting human health (Fann et al., 2018). Several studies (Reid et al., 2016; Youssouf et al., 2014) conclude that the main health effects of wildland fire smoke are cardiorespiratory resulting from high short-term exposure to concentrations of pollutants associated with the smoke. Populations at greatest risk include people with chronic lung disease, older individuals, children, pregnant women and fetuses (Cascio, 2018). Between 2008 and 2012, the economic impact of wildfires in the U.S. were estimated to be between tens to hundreds of billions of US$ (Fann et al., 2018). Additionally, Hurteau et al., (2014) predicted that California wildfire emissions would increase by 19-101% by 2100. Such studies have motivated the development of methods to estimate the ground-level impact of wildfires at spatial and temporal scales relevant to health effects.

The composition of wildfire smoke depends on multiple factors, such as fuel type, moisture content, fire temperature, wind conditions and other weather-related influences (Lipsett et al., 2008). The key air pollutants that are emitted during wildfire events include ambient air particles such as fine and coarse particulate matter (PM), and gases, carbon monoxide (CO), nitrogen oxides (NOx), volatile organic carbon (VOC) and other air toxics (Cascio et al., 2018). However, particulate matter is the principle pollutant of concern for exposures lasting hours to weeks (Lipsett et al., 2008); around 80%-90% of

mass particulate matter consists of $PM_{2.5}$ with high black carbon, organic carbon, and brown carbon content (Gyawali et al., 2009; Youssouf et al., 2014).

Large wildfires, such as the one studied here, produce highly buoyant plumes that can rise well above the mixed layer. The literature on this topic suggests that a significant fraction of the emissions can be transported above the boundary layer. Using Cloud-Aerosol Lidar with Orthogonal Polarization (CALIOP) data from CALIPSO satellite, Amiridis et al., (2010) examined emissions from agricultural fires over SW Russia and Eastern Europe between 2006 and 2008. For low intensity fires, the data indicate that biomass burning plumes are injected within the mixing layer. However they found that the smoke from approximately 50% of the 163 fires examined were above the mixing layer, with the injection heights ranging from 1.6 to 5.9 km. Paugam et al, (2016) concluded that weakly burning landscape-scale fires appear to inject most of their smoke into the PBL, but larger and/or more intense wildfires produce smoke columns that can rise rapidly and semi-vertically above the PBL. Martin et al, (2018) presents an analysis over 23,000 wildfire smoke plume injection heights derived from Multi-angle Imaging Spectro Radiometer (MISR) space-based, multi-angle stereo imaging and shows that plumes occur preferentially during the northern mid-latitude burning season, and the dominance of near-surface injection is evident in AOD-weighted and pixel-weighted digital data. However, some smoke is injected to altitudes well above 2 km at times in nearly all the regions and biomes in the heavily forested regions of North and South America, and Africa.

$PM_{2.5}$ mass concentration is monitored for regulatory compliance by either a federal reference method (FRM) or a federal equivalent method (FEM) (Noble et al., 2001). Due to the high cost of expansion of networks with this currently accepted instrumentation, most of the monitoring networks maintained by state and federal agencies do not provide sufficient spatial and temporal coverage to assess the health impacts for special events such as a wildfire (Ahangar et al., 2019).

Satellite remote sensing capabilities have been improving especially in terms of assessing $PM_{2.5}$ mass concentrations. The Moderate Resolution Imaging Spectroradiometer (MODIS) aboard both NASA's Terra and Aqua polar-orbiting satellites makes near-global daily observations of solar reflected radiances at the top of the atmosphere at a resolution between 1 and 10 km depending on specific retrieval product that is used to derive spectral Aerosol Optical Depths (AOD) (Remer et al., 2005). These observations are roughly five-minute snapshots occurring around 1030 local sidereal time (LST) for Terra observations, and around 1330 LST for Aqua observations, and are only available for cloud-free conditions. A recent study (Gupta et al., 2018) showed that under wildfires conditions, FEM $PM_{2.5}$ values and satellite-estimated values determined from geographically weighted regression models showed good agreement.

Because the short-term impact of the high concentrations of $PM_{2.5}$ associated with wildfire smoke is of concern, air quality management authorities require ground-level information on $PM_{2.5}$ at kilometer scale resolution to address the health concerns of the affected community. However, ground-based monitors provide limited spatial coverage, while satellite maps, being five-minute snapshots, only available for cloud free pixels, are

not consistently available to follow the time evolution of the ground-level impact of wildfire plumes (Sifakis et al., 2003). This chapter presents an approach to improve the spatial and temporal resolution of ground-based monitors by using information from satellite images and dispersion models.

2.2 Study Cases

We illustrate our approach by applying it to the analysis of data from a wildfire complex in northern California that started on 8 October 2017 and the Camp Fire that occurred in Butte County in northern California that ignited on 8 November 2018. We first provide brief descriptions of the fires and their impacts on air quality in the surrounding areas.

2.2.1 Northern California Wildfire

The five fires in this complex are known as the Atlas, Nuns, Tubbs, Pocket, and Redwood Valley fires. Over the course of two weeks, these wildfires, illustrated in Figure 1, consumed a total of 198,867 acres (CALFIRE, 2017) and resulted in 44 fatalities and about $9 billion worth of insurance claims (Kasler et al., 2017). Furthermore, the heavily polluted skies caused schools and universities to close and hundreds of flights at San Francisco Airport to be delayed or canceled (Gupta et al., 2018).

Table 2.1 shows the statistics of the 24 hour averaged $PM_{2.5}$ concentrations measured by the California Air Resources Board Air Quality Management and Information System (AQMIS), shown in Figure 2.1. During October 10 to October 13, when the fires were at their peak (Mass and Ovens, 2019), the mean concentration over

the 22 monitors was above the EPA 24-hour average standard of 35 $\mu g/m^3$; the highest concentration of 55 $\mu g/m^3$ was recorded on October 13.

Figure 2.2 shows the wind roses constructed using hourly meteorological data from the Remote Automatic Weather Stations at Middle Peak (37.9308, -122.591). We see that except for October 10, 14, and 15, the dominant wind blew was from the northwest bringing wildfire smoke into the Bay area that led to the severe deterioration of air quality.

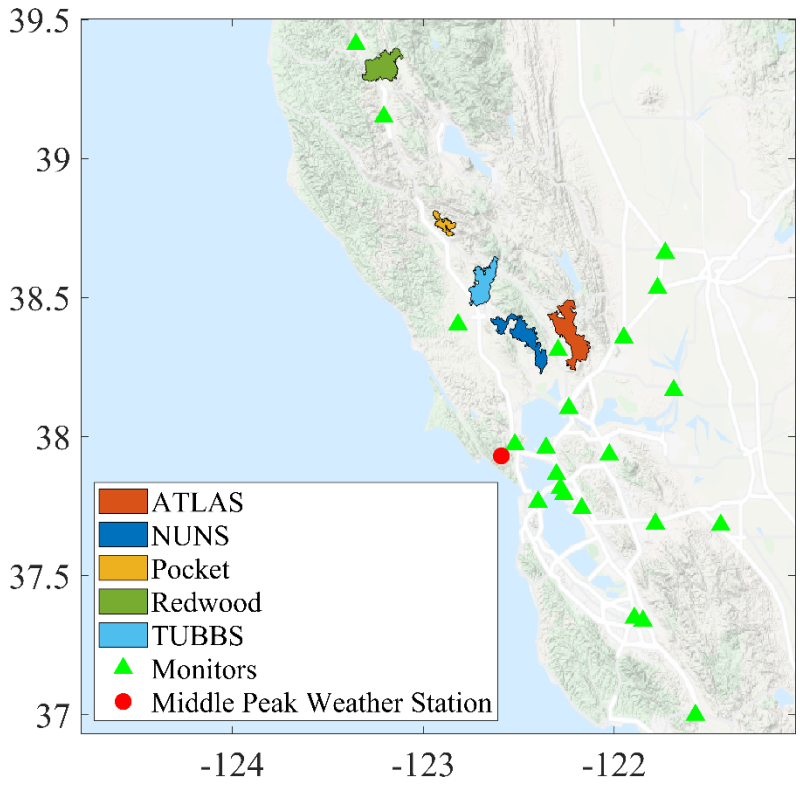

Figure 2.1. Map of routine state-agency surface $PM_{2.5}$ monitors and fire sources in the San Francisco Bay area. Monitor data obtained from the AQMIS

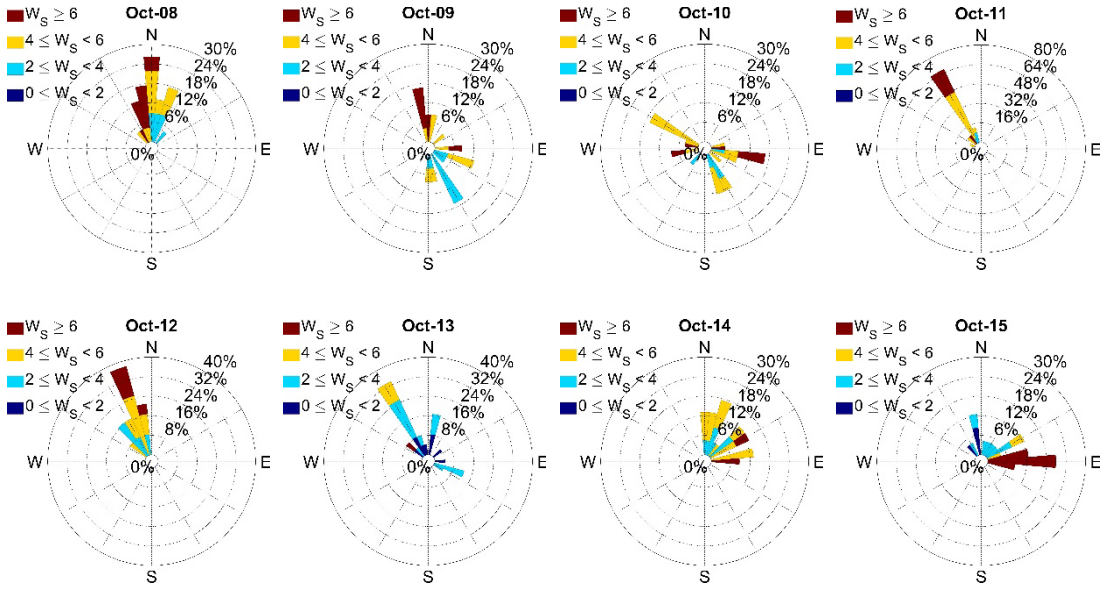

Figure 2.2. Wind rose of hourly data at Middle Peak California. The color represents the wind speed in meters per second, and the percent number at the top right corner represents the wind direction frequency

Table 2.1. Statistics of Daily Averaged Concentrations measured at AQMIS monitors in San Francisco Bay area

Date	24 hours Averaged Measured Concentration ($\mu g/m^3$)	Standard deviation of Measured Concentration ($\mu g/m^3$)
Oct-8	11	6
Oct-9	29	19
Oct-10	55	43
Oct-11	44	27
Oct-12	42	24
Oct-13	49	41
Oct-14	21	9
Oct-15	16	14

2.2.2 The Camp Fire

The Camp Fire, which broke out in Butte County, California, was first reported on 8 November 2018 and reached 100 percent containment on 25 November 2018

(CALFIRE, 2018). Over a period of two weeks, the fire destroyed 18,804 structures and burned 62,052 hectares(CALFIRE, 2018). It has been designated as the most destructive and deadly wildfire in California state history.

Measurements from 17 regulatory agency stations from AQMIS in Sacramento Valley are shown in Figure 2.3. Figure 2.4 shows the wind roses constructed using hourly meteorological inputs from the Automated Surface Observing System at Yuba County (39.1020, -121.5688). The most frequent wind direction is north except for November 12 as Figure 2.4. Moreover, strong winds that exacerbated the spread of the fire occurred on November 8 and 11, when average wind speeds were above 7 m/s. Table 2.2 shows that the highest mean value of $PM_{2.5}$ of 197$\mu g/m^3$ was measured on November 15, and the mean concentrations were above the EPA 35 $\mu g/m^3$ 24-hour average standard after November 9.

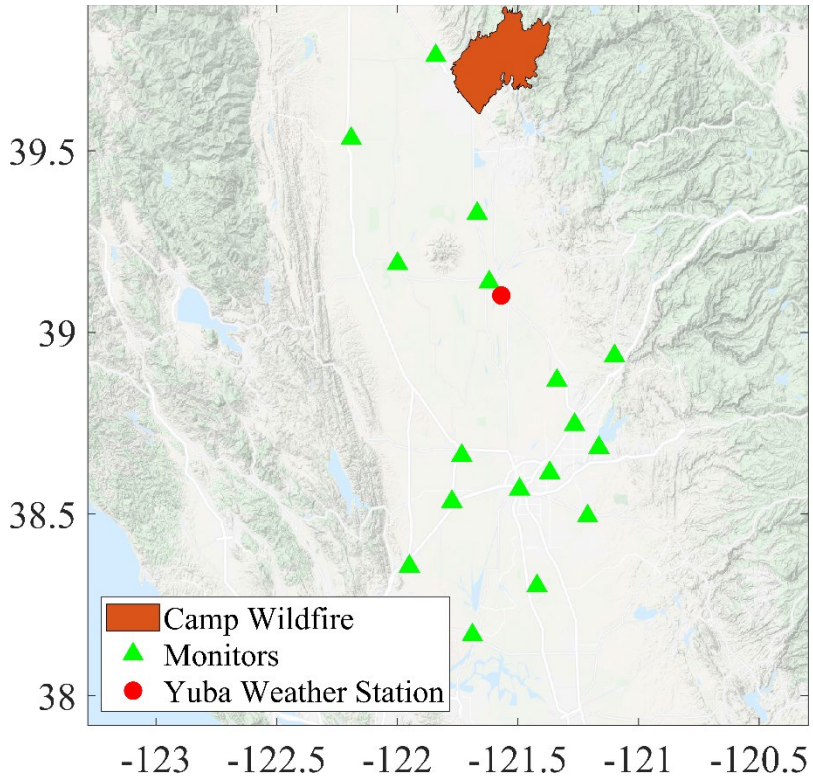

Figure 2.3. Map of routine state-agency surface PM2.5 monitors and fire source in Sacramento Valley. Monitor data obtained from the California Air Resources Board Air Quality Management and Information System (AQMIS)

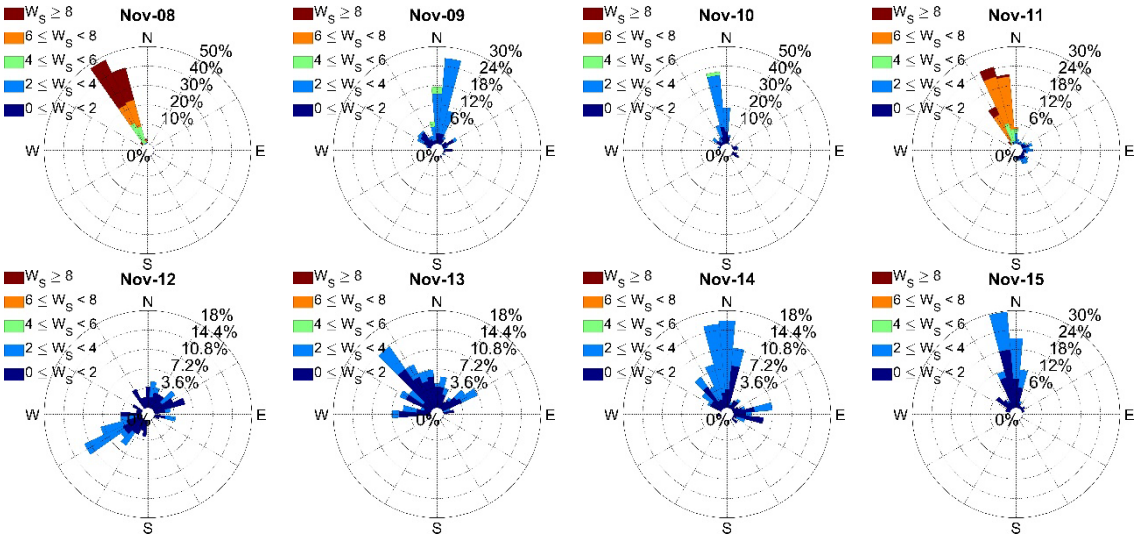

Figure 2.4. Wind rose of hourly data at Yuba California

Table 2.2. Statistics of Daily Averaged Concentrations measured at AQMIS monitors in Sacramento Valley

Date	24 hours Averaged Measured Concentration ($\mu g/m^3$)	Standard deviation of Measured Concentration ($\mu g/m^3$)
Nov-8	16	7
Nov-9	39	28
Nov-10	116	61
Nov-11	76	47
Nov-12	72	44
Nov-13	88	54
Nov-14	159	67
Nov-15	197	86
Nov-16	122	88
Nov-17	114	52
Nov-18	74	28

2.3 Methodology

2.3.1 Technical Approach

A common approach to improving the the spatial resolution of ground-based $PM_{2.5}$ measurements by is interpolation of the observed concentrations at monitors, C_o, using a purely statistical interpolation technique such as Kriging, or one based on statistical models that linearly combine meteorological and land-use variables that are considered relevant by Gupta et al. (2018). The problem with these approaches is that they do not account for the underlying physical structure of the smoke plume that governs the concentration field. For example, Kriging cannot account for the anisotropy of the concentration field associated with the large smoke plumes associated with wildfires. We can improve upon simple Kriging by using an estimate from a transport and dispersion model, C_p, to remove the structure in observed concentration to leave behind a residual,

which can then be interpolated using Kriging (Venkatram, 1988;Schneider et al., 2017).We can express the observed concentration C_o at a monitor as

$$C_o = C_p + \varepsilon \tag{2.1}$$

where ϵ is the residual whose statistics are spatially isotropic. Then the estimate of the concentration, C_o^e, at a receptor of interest (not at a monitor) is estimated through

$$C_o^e = C_p + Kriged(\varepsilon) \tag{2.2}$$

The spatial resolution of C_o^e is determined by that of the dispersion model used to calculate C_p, and its uncertainty is determined by the spatial statistics of ϵ.

The accuracy of this approach depends on the ability of the chosen dispersion model to describe the underlying structure. In the case of a wildfire, this structure depends on a host of processes, including emissions which can be one of the most uncertain. To avoid specifying its value, we treat it as a model parameter whose value is obtained by minimizing $\sum \varepsilon^2$ at the ground monitors. We rewrite Equation (2.1) as

$$C_{oi} = \sum_j T_{ij} E_j + \varepsilon_i \tag{2.3}$$

where C_{oi} is the measured concentration at monitor 'i' , T_{ij} is the model estimate of the concentration at *'i'* due to unit emission rate at *'j'*, and E_j is the inferred emission rate obtained by minimizing $\sum_i \varepsilon_i^2$ with the constraint that their values are greater than or equal to zero. To achieve this, we used the MATLAB function *lsqnonneg* described in Lawson and Hanson (1995). We compute the transport coefficients, T_{ij}, using two different dispersion models, which are described in the next section.

In summary, improvement of the spatial resolution of the information from the ground-based monitors involves the following steps:

1. The concentration estimates from a transport/dispersion model are fitted to the $PM_{2.5}$ measurements at the AQMIS monitors. The inputs to the model are the a) locations of the sources and their sizes, b) locations of the AQMIS monitors, and c) wind speed and direction and boundary layer height from a meteorological model. The outputs from this step are emission rates that provide the best fit between model estimates of concentrations and corresponding measurements (Equation (2.3)).
2. The model with the emissions derived from step 1 is used to compute concentrations on a grid with the desired spatial resolution.
3. The residuals between model estimates and measurements at the *AQMIS monitors* are interpolated using Kriging to the fine mesh grid where concentrations are estimated in step 2 (Equation (2.2)). The final product is a map of $PM_{2.5}$ concentrations at the desired spatial resolution. We also examined the value of using satellite information to enhance the information from the ground-based AQMIS monitors.

The following sections provide details of the model and the methods used these steps. We applied two transport-dispersion models, which are described next.

2.3.2 The Backward Lagrangian Model

The model applied here is similar to the Lagrangian model used in Pournazeri et al.,(2014). This model estimates concentrations by tracing the history of the air parcel

released at different hours in a day from a receptor of interest. Each backward trajectory from a receptor is extended backward in time for 12h using 0.25h time steps. The concentration along each back trajectory is computed from

$$T_k = T_{k-1} \cdot min\left(\frac{z_{bl}(k-1)}{z_{bl}(k)}, 1\right) + \frac{q_k \cdot \Delta t}{z_{bl}(k)} \tag{2.4}$$

where T_k is the concentration at the $\mathrm{k^{th}}$ step, z_{bl} is the boundary layer height, Δt is the time step, and q_k is the emission rate per unit area injected into the air parcel. The term within the parenthesis ensures that the concentration does not increase if the box shrinks. The transport coefficient in Equation 3 for each trajectory is computed from Equation 4 by taking $q_i = 1 \frac{\mathrm{g}}{\mathrm{m^2}} / s$ over the area of the fire of interest. The 24 hourly transport coefficients corresponding to a 24-hour period are averaged to obtain an averaged transport coefficient.

Much of the emitted carbon from a wildfire is initially present in the gas phase, with potential to condense and form fine particulates over time. Recent research(Ahern et al., 2019) shows that the total organic aerosol mass (primary mass plus secondary mass) enhancement could be between factor 1 and 3 after 1.5 aging hours based on different fuel types. Thus, the emissions inferred by fitting model estimates to ground-level concentrations represent "effective" emissions which can differ from "bottom-up emissions" based on fuel types and consumption rates(Larkin et al., 2009).

In our calculations, we assume that $PM_{2.5}$ originates from the five areas corresponding to the Atlas, Nuns, Tubbs, Pocket, and Redwood fires comprising the fire complex, shown in Figure 2.2. Each day of the fire is associated with a background

emission density that is associated with the entrainment of emissions from smoke above the boundary layer that is not accounted for in the dispersion model. To account for this background $PM_{2.5}$, we introduce a background emission rate, q_b, in fitting model estimates to observations

$$C_{oi} = \sum_j T_{ij} E_j + q_b \tau \left\langle \frac{1}{z_{bl}} \right\rangle + \varepsilon_i \tag{2.5}$$

where the angle brackets refer to an average over all 24 trajectories, and $\tau = 24h$. The emission rates, E_j, from the fires as well as q_b are treated as parameters whose value is obtained by fitting model estimates to corresponding 24-hour averaged $PM_{2.5}$ observations.

2.3.3 Plume Model

In this model, we estimate the 24-hour averaged concentration by describing the dispersion of emissions from the fire as a plume whose horizontal dimensions are determined by the spread of the 24 trajectories. The transport coefficient is computed from a segmented plume model

$$T_{ij} = \frac{1}{\sqrt{2\pi}} \frac{1}{\sigma_y} \frac{1}{\langle U z_{bl} \rangle} exp\left(-\frac{y^2}{2\sigma_y^2} \right) \tag{2.6}$$

where the origin of the co-ordinate system is at the center of the fire. The horizontal spread, σ_y, is computed relative to the mean of the 24 1-hour trajectories emanating from the fire source; the angle brackets refer to the mean along this trajectory. The horizontal distance, y, at each time step is taken to be the perpendicular distance between the midpoint of each instantaneous trajectory segment and the mean trajectory segment at the same time step. The standard deviation of these horizontal distances at

each time step provides the horizontal spread as a function of travel time from the source (Haan and Rotach, 1995). These values are then fitted to an equation of the form $\sigma_y = \sigma_v t$, where t is the travel time, and σ_v is an effective horizontal turbulent velocity. The size of the fire is accounted for in the total horizontal spread, σ_{yt}, through $\sigma_{yt}^2 = \sigma_y^2 + \sigma_{yfire}^2$, where $\sigma_{yfire}^2 = R^2/2$,where R is the radius of the fire which can be approximated according to the actual size of the fires.

2.3.4 Data Input

The two models were fitted to the the surface $PM_{2.5}$ concentrations obtained from state agency routine surface monitors (AQMIS).The meteorological inputs for the models were obtained from the High-Resolution Rapid Refresh (HRRR) model (Blaylock et al., 2017; Rolph et al., 2017). The HRRR model provides 3-km resolved, hourly updated meteorological data field that includes the model inputs: ten-meter wind speed (U), wind direction (θ), and the boundary layer height (z_{bl}).

We also examined the value of satellite data in improving the accuracy of the modeled $PM_{2.5}$ concentration field by incorporating an empirical model based on the aerosol optical depth (AOD) measured by the Moderate Resolution Imaging Spectroradiometer (MODIS), which is carried by NASA's Terra and Aqua satellites. We utilized MODIS-based AOD from the MAIAC (Multi-Angle Implementation of Atmospheric Correction) retrieval products, which uses a new advanced algorithm for gridding MODIS measurements to improve accuracy of cloud detection aerosol retrievals and atmospheric correction (Lyapustin et al., 2011). Each daily MAIAC file (MCD19A2)

contains gridded AOD retrievals from both Terra and Aqua and the product shows good accuracy within 1 km resolution (Lyapustin and Wang, 2018).

2.3.5 AOD Model

Figure 2.5 shows an example of the AOD at 0.47μm at the starting and middle days of the fires. We clearly see that the AOD increased significantly after the fires began on October 13, 2017 and on November 15, 2018, which is consistent with the air quality data presented in Table 2.1and Table 2.2. Although the satellite data capture the $PM_{2.5}$ gradients of the spatial distribution during the fires on October 13 they miss a substantial fraction of the pixels. Furthermore, the data, based on interpretation of column integrated AOD, is only roughly correlated with surface $PM_{2.5}$ concentrations and is thus uncertain (Gupta et al., 2006; Marsha & Larkin, 2019; Donkelaar et al, 2006). However, the satellite data provides useful information at areas not covered by ground-level monitors, and can add value to the results from the dispersion model. So it is worthwhile to examine the situation in which AOD data can improve estimates from the dispersion models.

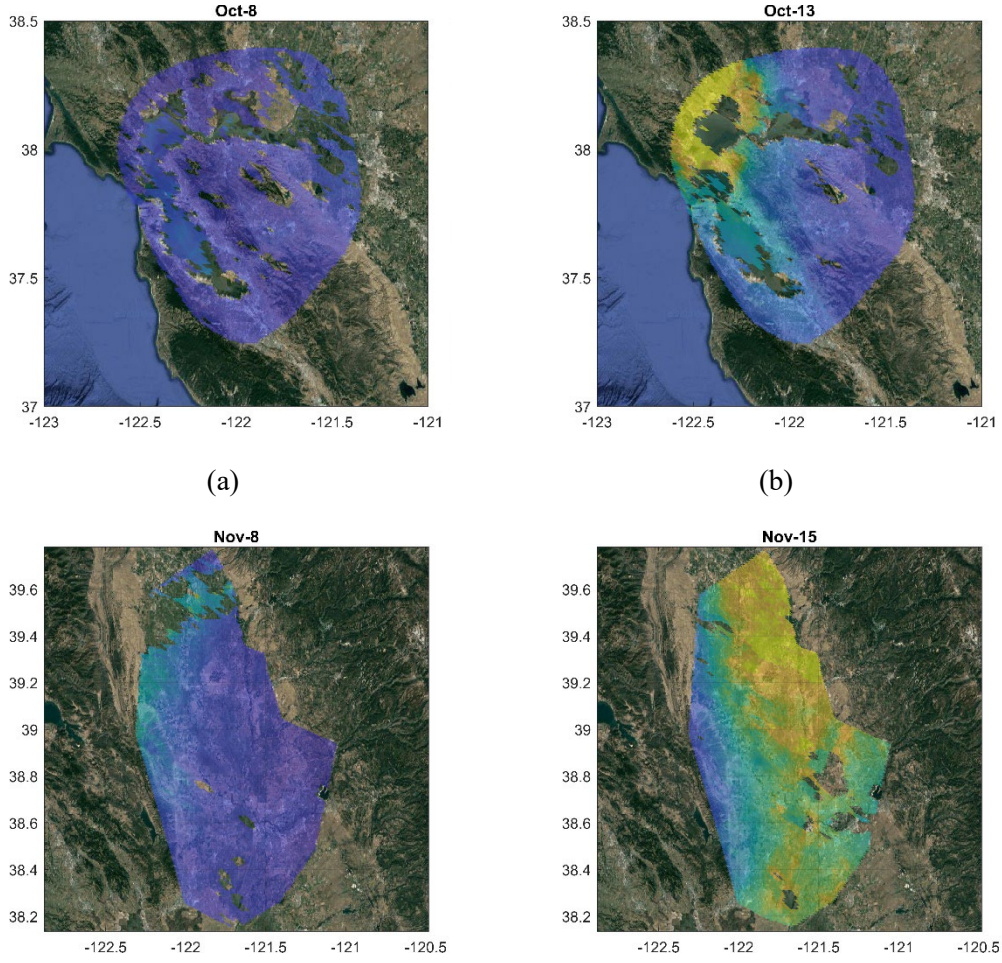

Figure 2.5. Aerosol optical depth observation from MAIAC MCD19A2 at 0.47$\boldsymbol{\mu}$m at (a) October 8, 2017, (b) October 13, 2017, (c) November 8, 2018, and (d) November 15, 2018

We fitted the measured AOD to the ratio of 24-hour $PM_{2.5}$ concentration to planetary boundary layer (PBL) height using a power curve as in (Liu et al., 2005); the column integrated value measured by AOD divided by the boundary layer height is likely to be correlated with the surface $PM_{2.5}$ concentration if material is well mixed through the depth of the boundary layer. Figure 2.6 (a) and (c)shows the performance of the ratio of AOD to PBL in describing daily $PM_{2.5}$ concentrations. The performance of the models is evaluated by geometric mean (m_g) and the geometric standard deviation (s_g) of the ratios

of the modeled predictions to the observations (Venkatram, 2008); m_g=1 indicates no bias, m_g greater (less) than unity indicates overestimation (underestimation) from the model, and s_g^2 is an approximate measure of the 95% confidence interval. Figure 2.6 (b) and (d) shows that the coefficient of determination, R^2, between observations and model estimates from the AOD model is 0.53 and 0.51 in the 2017 Northern CA Fires and 2018 Camp Fire respectively. The estimates from the AOD model are correlated with both low and high $PM_{2.5}$ measurements, which suggests that AOD data can be useful in analyzing the wide range of $PM_{2.5}$ concentrations observed during the evolution of a fire. However, the scatter between model estimates and measurements is not small: $s_g^2 = 2.98$ and 3.77 for the 2017 Northern CA Fires and 2018 Camp Fire respectively.

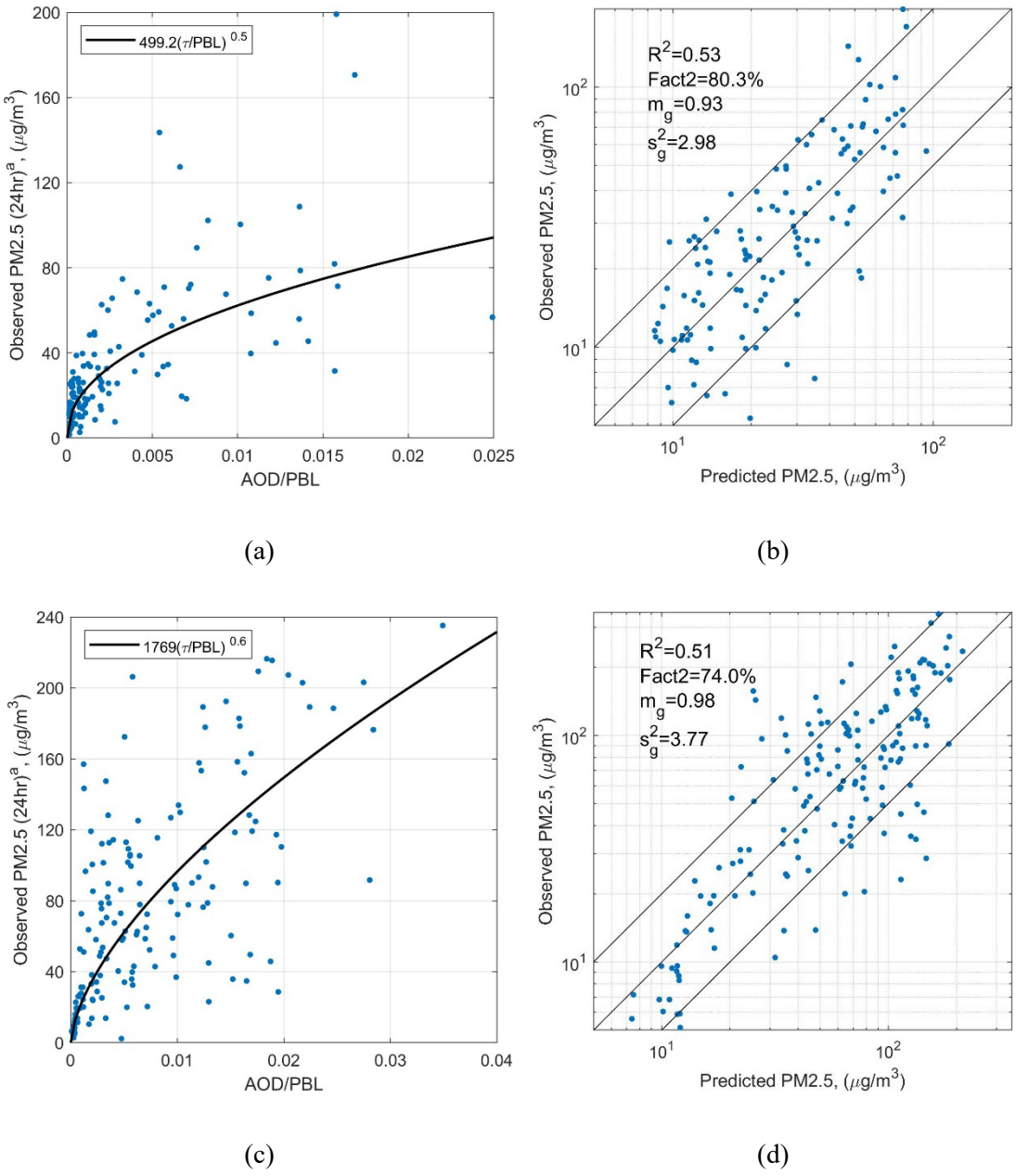

Figure 2.6. Relationship between measured $PM_{2.5}$ and AOD/PBL at the nearest satellite pixel to the measurement station. (a) AOD model fitted to observations in 2017 Northern CA Fires, and (b) performance of model in 2017 Northern CA Fires (c) AOD model fitted to observations in 2018 Camp Fire, and (d) performance of model in 2018 Camp Fire

2.4 Results and Discussion

2.4.1 Modeling Results

We estimated the daily emission rates for each of the five fires in the complex by fitting estimates from both the backward Lagrangian model and the plume model to concentrations at the 22 AQMIS receptors using Equation (2.4) and Equation (2.6). Distributions of emission estimates were created by bootstrapping the residuals between model estimates and corresponding observations: 1500 sets of pseudo observations were created by randomly adding these residuals to model estimates, and fitting each set of pseudo observations to the model estimates. The 95% confidence intervals were derived from the resulting distributions of emissions.

The results from the analysis are shown in Figure 2.7. In the 2017 Northern CA Fires, we see that both models provide similar descriptions of the measured concentrations with the Lagrangian model yielding a higher R^2 while the Plume model overestimating less as shown in Figure 2.7 (a) and (b). The Figure 2.7 (a) and (c) show that the Plume model yields $R^2 = 0.70$ for the 2017 Northern CA Fires and $R^2 = 0.59$ for the 2018 Camp Fire.

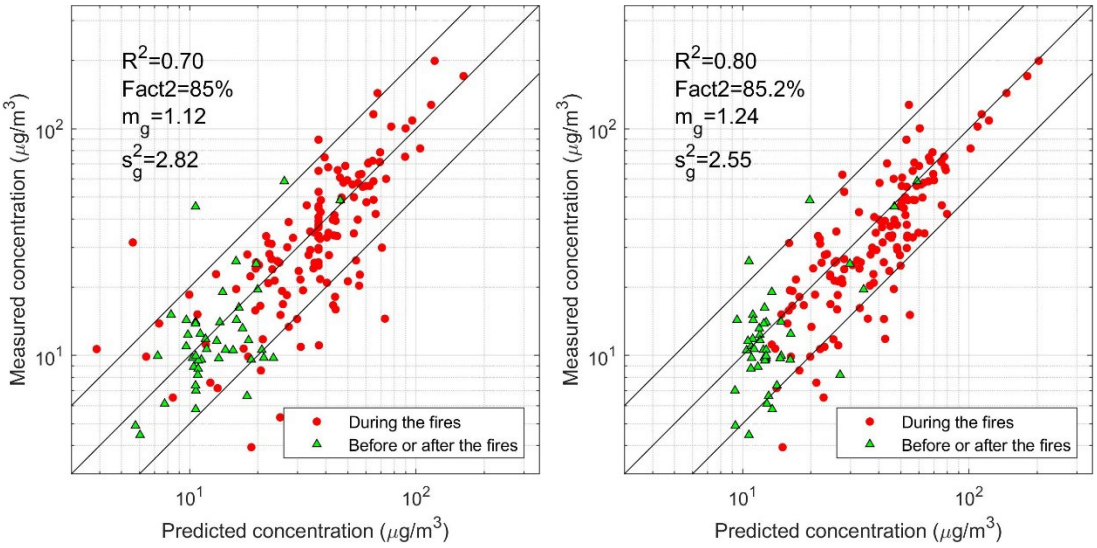

(a) (b)

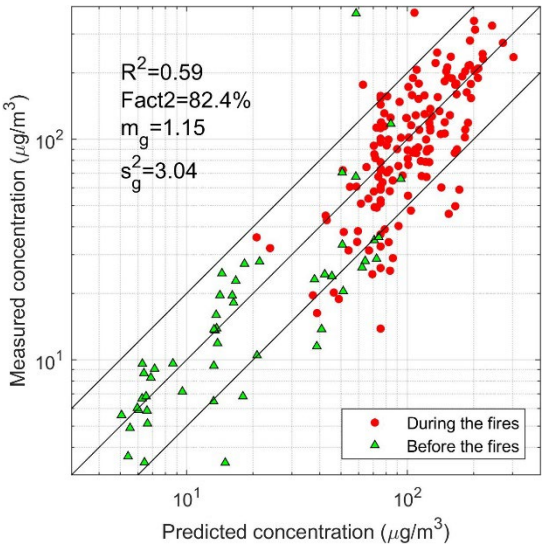

(c)

Figure 2.7. Measured $PM_{2.5}$ concentrations fitted to model estimates from (a) Plume Model in 2017 Northern CA Fires. (b) Lagrangian Model in 2017 Northern CA Fires. (c) Plume Model in 2018 Camp Fire

Figure 2.8 compares time series of $PM_{2.5}$ estimates from the Plume Model at selected receptors to corresponding measured concentrations. We see that the Plume Model captures the peak concentrations, and model estimates compare well with measurements during the whole time period of the fire.

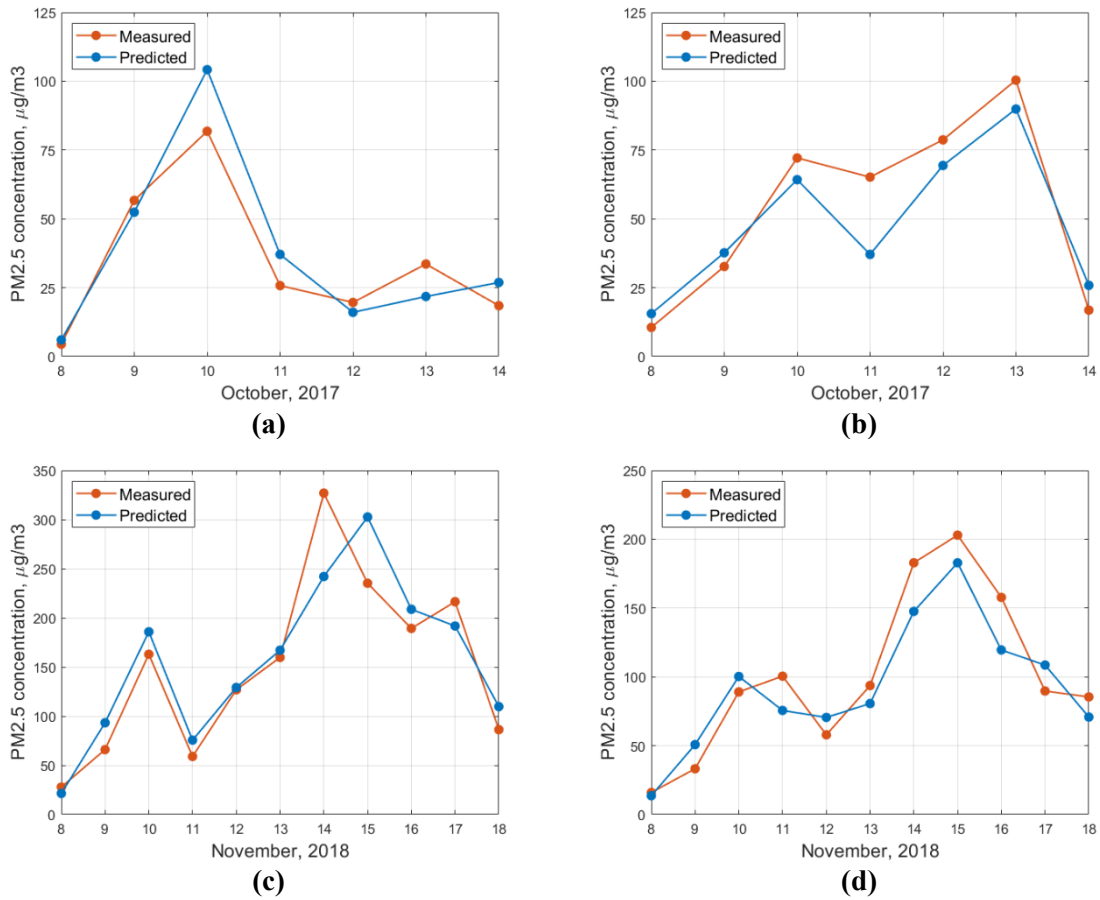

Figure 2.8. Time Series of the predicted and observed concentrations from (a) Sebastopol-103 Morris Street in 2017 Northern CA Fires, (b) Vallejo-304 Tuolumne Street in 2017 Northern CA Fires, (c) Gridley-Cowee Avenue in 2018 Camp Fire, and (d) Elk Grove-Bruceville Road in 2018 Camp Fire

Figure 2.9 compares the sum of the inferred emission rates over the fires with independent, bottom-up estimates made by US Forest Service (USFS) using fuel information (Larkin et al., 2009).We see that in the 2017 Northern CA Fires, the inferred emission rates from the two models are consistent with each other. However, during the

2017 Northern CA Fires and the first two days of 2018 Camp Fire, the model inferred emissions are well below the fuel-based estimates. This is reasonable because the inferred emission rates only include those that directly affect surface concentrations at monitors, which are predominantly those emissions that stay confined through the depth of the boundary layer. On the other hand, the injection height can typically reach a few kilometers (Amiridis et al., 2010; Martin et al., 2018), which is much larger than the daily averaged PBL in our study cases which are range from 100 to 400m obtained by HRRR model. The USFS estimates refer to total emissions, some of which are likely to stay above the boundary layer and do not affect ground-level concentrations at the AQMIS monitors. During the Nov 10 to Nov 18, most of the model inferred emissions are larger than the bottom-up emissions. This discrepancy could be related to the formation of secondary aerosols that are not accounted for in the bottom-up estimates (Ahern et al., 2019).

The modeled concentrations at downwind monitors account for the background emissions which are determined by least square fitting to concentration measurements. Notice that on October 10, 2017, the inferred emission rates from both models are relatively low even though the average measured surface concentration is higher than that of any other day (See Table 2.1). This is because the wind directions indicated that most monitors were not affected by the fire, which also appears to be supported by the wind rose in Figure 2.2. However, the inferred background concentration on this day is high to account for the high $PM_{2.5}$ concentrations at the upwind ground monitors on this day.

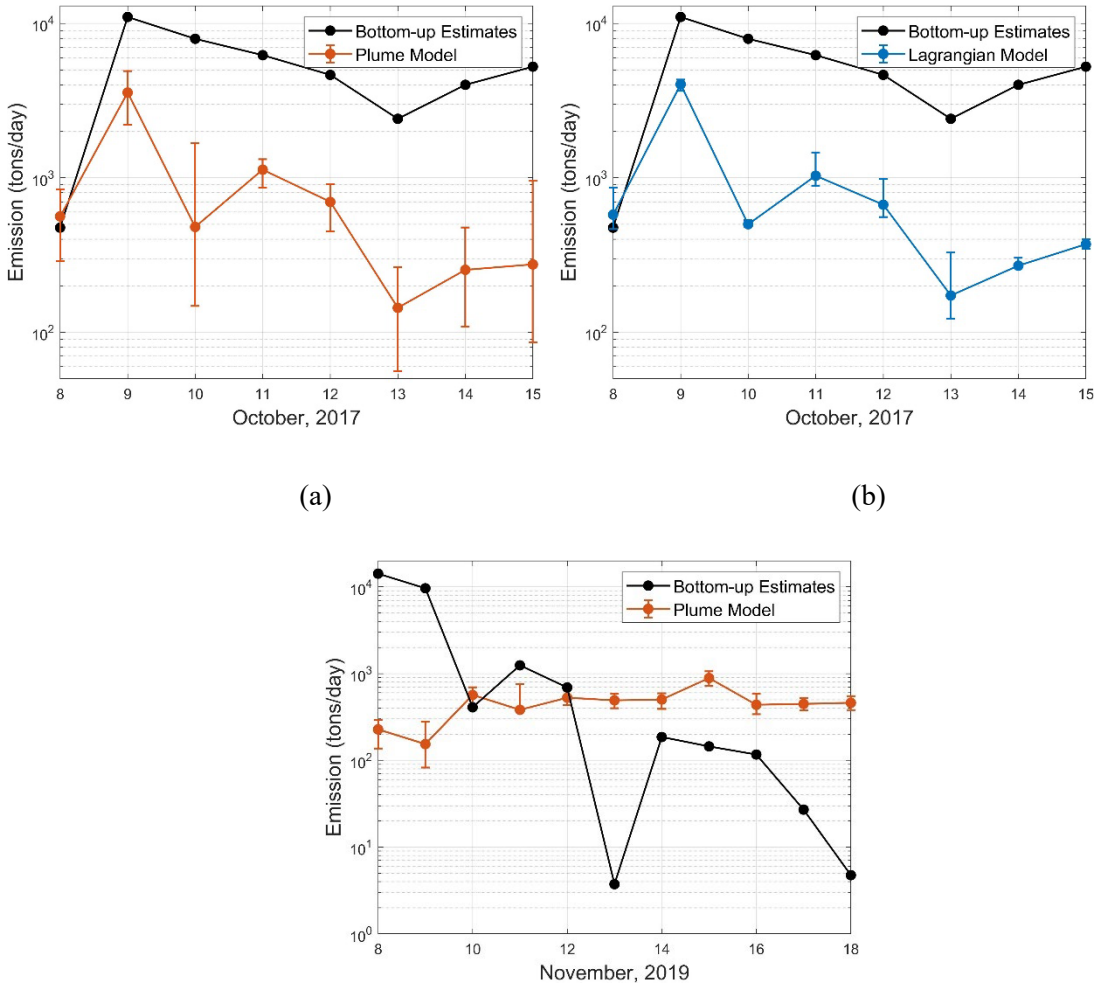

Figure 2.9. Emissions from the models compared with those from USFS bottom-up estimates from (a) Plume model in 2017 Northern CA Fires, (b) Lagrangian model in 2017 Northern CA Fires, and (c) Plume model in 2018 Camp Fire. The vertical bars indicate 95% confidence intervals derived from bootstrapping, as discussed in text.

Table 2.3 shows that the emission estimates from the two models differ for each of the sources but the sum of the estimated emissions are similar as indicated in Table 2.4. In the 2017 Northern CA Fires, the largest emissions are estimated to be 3566 and 4032 tons/day, and both of them appeared on October 10, which correlated with the statistics results shown in Table 2.1. In the 2018 Camp Fire, Table 2.5 shows that the

highest emissions were estimated to be 890 tons/day on November 15, which showed an agreement with results from Table 2.2.

Table 2.3. Emissions rates and 95% confidence intervals on Oct 9 calculated by the Plume model and the Lagrangian model

Source	Plume Model Emission Rates (Tons/Day)	Plume Model 95% Confidence Interval (Tons/Day)	Lagrangian Model Emission Rates (Tons/Day)	Lagrangian Model 95% Confidence Interval (Tons/Day)
ATLAS	872	458-1632	640	289-962
NUNS	0	0-1328	2371	270-4036
POCKET	828	113-1009	0	0-0
REDWOOD	0	0-584	531	150-831
TUBBS	2030	754-2892	493	0-1163

Table 2.4. Sum of the emissions in 2017 Northern CA Fires inferred from models. The lower and upper limits, LL and UL refer to 95% confidence limits normalized by the mean sum of emissions from all fires

Date	Plume Model			Lagrangian Model		
	Mean sum (tons/day)	LL	UL	Mean sum (tons/day)	LL	UL
Oct-8	563	0.51	1.49	578	0.81	1.50
Oct-9	3566	0.62	1.38	4032	0.91	1.07
Oct-10	481	0.31	3.49	501	0.96	1.06
Oct-11	1129	0.76	1.17	1032	0.86	1.42
Oct-12	698	0.64	1.30	670	0.83	1.47
Oct-13	144	0.39	1.84	173	0.71	1.89
Oct-14	254	0.43	1.89	270	0.96	1.12
Oct-15	275	0.31	3.47	372	0.93	1.07

Table 2.5. Emissions from 2018 Camp Fire inferred from models. The lower and upper limits, LL and UL refer to 95% confidence limits normalized by the mean sum of emissions from all fires

Date	Plume Model		
	Mean sum (tons/day)	LL	UL
Nov-8	227	0.60	1.28
Nov-9	154	0.54	1.82
Nov-10	568	0.78	1.23
Nov-11	383	0.00	1.97
Nov-12	528	0.82	1.24
Nov-13	492	0.81	1.19
Nov-14	503	0.78	1.18
Nov-15	890	0.82	1.19
Nov-16	437	0.78	1.34
Nov-17	448	0.85	1.17
Nov-18	461	0.82	1.19

2.4.2 Concentration Maps

We next examined the value of the AOD based model in improving the estimates from the dispersion model. The measured concentrations were fitted to a linear combination of the two models as follows

$$C_o = \boldsymbol{A}C_{plume} + \boldsymbol{B}C_{AOD} + \varepsilon \tag{2.7}$$

where C_{plume} is the estimate from the plume model, C_{AOD} is the estimate from the AOD model, $\boldsymbol{A}$ and $\boldsymbol{B}$ are non-negative regression coefficients. Non-negative least squares regression is then used to fit $\boldsymbol{A}$ and $\boldsymbol{B}$ to daily concentrations over all the AQMIS stations. We see from Table 2.6 and Table 2.7 that the Combined Model R^2 usually increased compared to those from the Plume Model when the satellite term makes a

contribution. In the 2017 Northern CA Fires, the largest R^2 improvement was from 0.41 to 0.59 on October 9, and in the 2018 Camp Fire the largest improvement was from 0.38 to 0.73 on November 12. Figure 2.10 shows this improvement on November 12.

Table 2.6. Contributions of Plume and AOD model estimates to Observed Concentrations in 2017 Northern CA Fires. The value of *B* relative to that of *A* indicates the contribution of the AOD model.

Date	***A***	***B***	Plume Model R^2	Combined Model R^2
Oct-8	0.86	0.16	0.40	0.43
Oct-9	0.65	0.35	0.41	0.59
Oct-10	0.82	0.32	0.70	0.71
Oct-11	0.92	0.16	0.34	0.36
Oct-12	0.97	0.05	0.83	0.83
Oct-13	0.74	0.42	0.61	0.66
Oct-14	1.00	0.00	0.28	0.28
Oct-15	0.72	0.20	0.33	0.39

Table 2.7. Contributions of Plume and AOD model estimates to Observed Concentrations in 2018 Camp Fire

Date	***A***	***B***	Plume Model R^2	Combined Model R^2
Nov-8	0.57	0.27	0.13	0.15
Nov-9	1	0	0.37	0.37
Nov-10	1	0	0.20	0.20
Nov-12	0.35	0.67	0.38	0.73
Nov-13	1	0	0.49	0.49
Nov-14	0	1.07	0.29	0.57
Nov-15	0.34	0.84	0.24	0.33
Nov-16	0	1.28	0.22	0.53
Nov-17	0.52	0.80	0.49	0.68
Nov-18	1	0	0.32	0.32

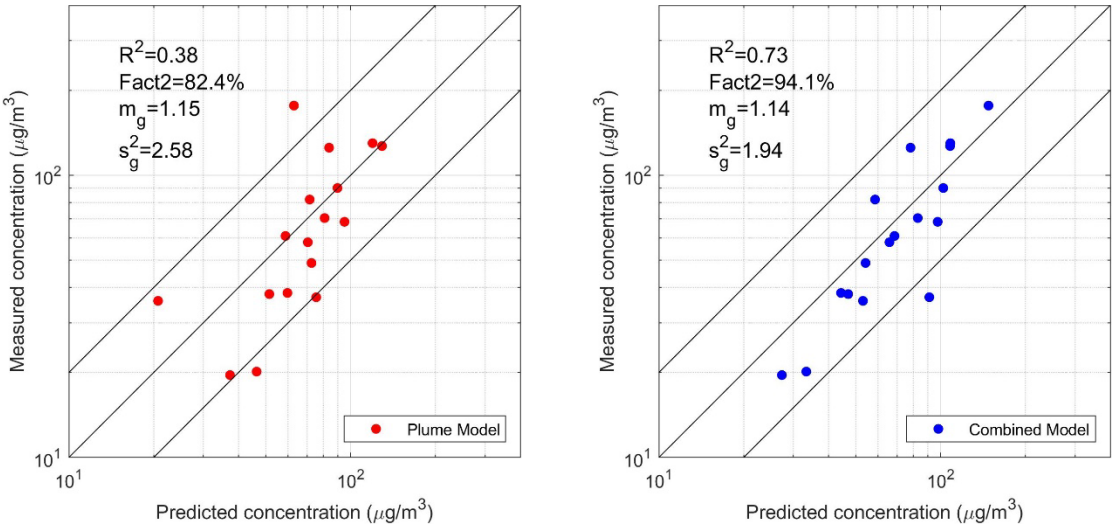

(a) (b)

Figure 2.10. Scatter with improved R^2 on November 12 from (a) Plume Model and (b) Combined Model

To use the residual Kriging method that we mentioned in Chapter 2.3.1, we generated the 100×100 grid (approximate 1km resolution) in the area we are interested in. Figure 2.11 shows the semivariograms used in the residual Kriging; each pair of locations were placed into 15 bins to fit spherical models shown in the figure

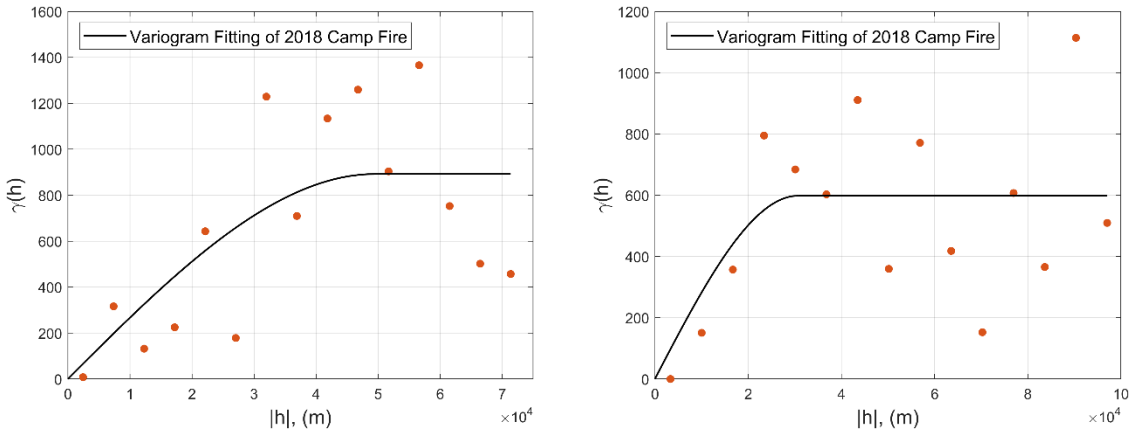

(a) (b)

Figure 2.11. Semivariogram by grouping each pair of locations into 15 lag bins from (a) Residual kriging 2017 Northern CA Fires on October 13, and (b) Residual kriging 2018 Camp Fire on November 13

This combined model was then used to create a concentration map as described previously using Equations (2.1) and (2.2). Figure 2.12 compares the map with a spatial resolution of 1 km created using Equation 7 with that created by simple Kriging of observations on October 13, 2017 and November 13, 2018, two of the high PM days during the fires. Visually, there appears to be little difference between the maps, but Figure 2.12 (e) and (f) show differences as large as 10 $\mu g/m^3$ at several locations. Figure 2.12 (e) shows that the most negative residuals and positive residuals appear at the place where satellite information was missing at most locations as seen in Figure 2.5 (b).

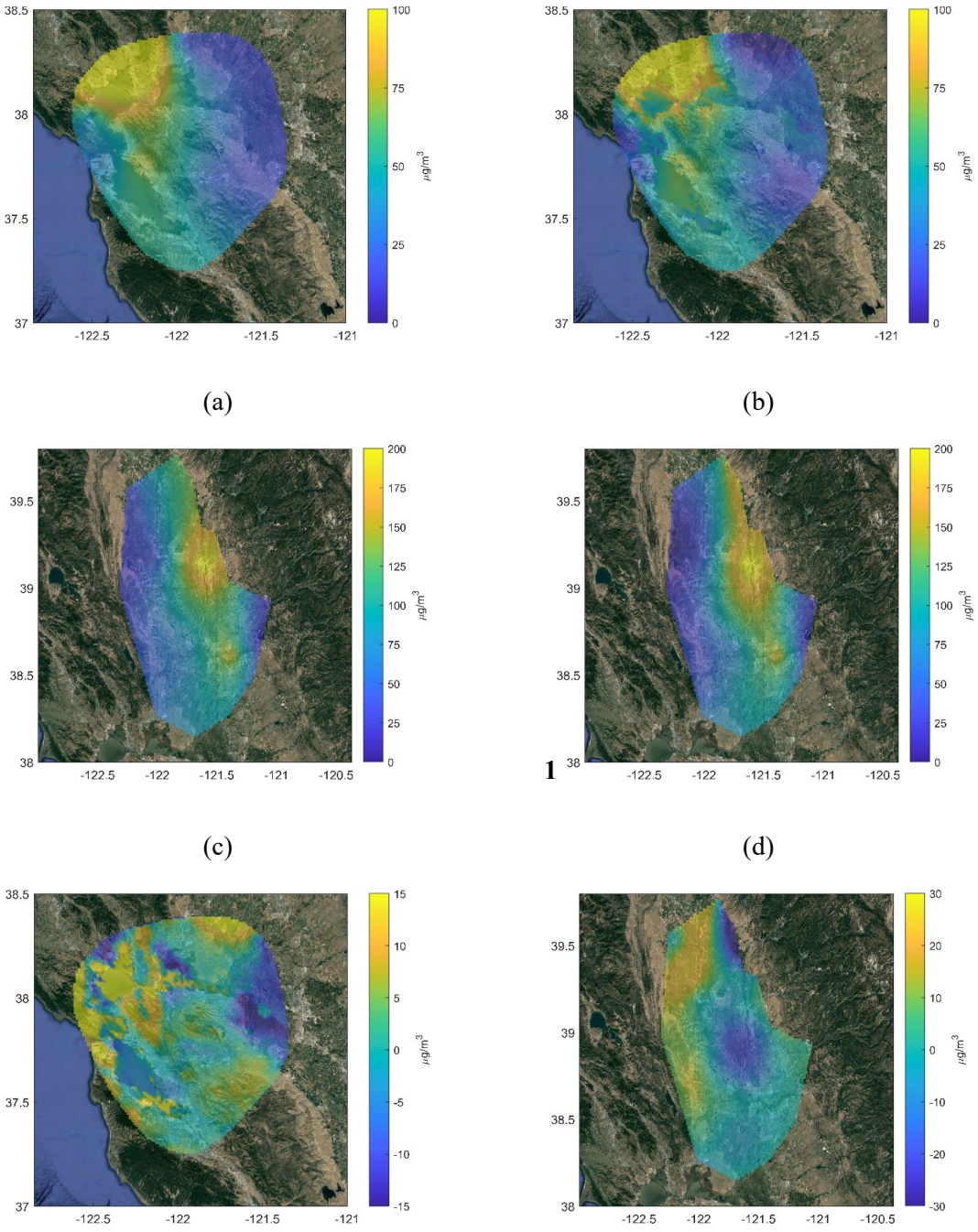

Figure 2.12. $PM_{2.5}$ maps created by (a) Kriging Observations in 2017 Northern CA Fires, (b) Model estimates combined with Kriged residuals for 2017 Northern CA Fires, (c) Kriged Observations in 2018 Camp Fire, (d) Model estimates combined with Kriged residuals in 2018 Camp Fire, (e) Residuals of Kriged Observations minus Combined model in 2017 Northern CA Fires, and (f) Residuals of Kriging Observations minus Combined model in 2018 Camp Fire

Figure 2.13 indicates that the concentration field determined from the combined model shows greater spatial variation than that from simple Kriging. This is expected because Kriging can only reflect the variance of the observations. The differences can be above 10 $\mu g/m^3$ or below -10 $\mu g/m^3$ because the model introduces the variance associated with the underlying transport processes that produce the structures of the fire plumes.

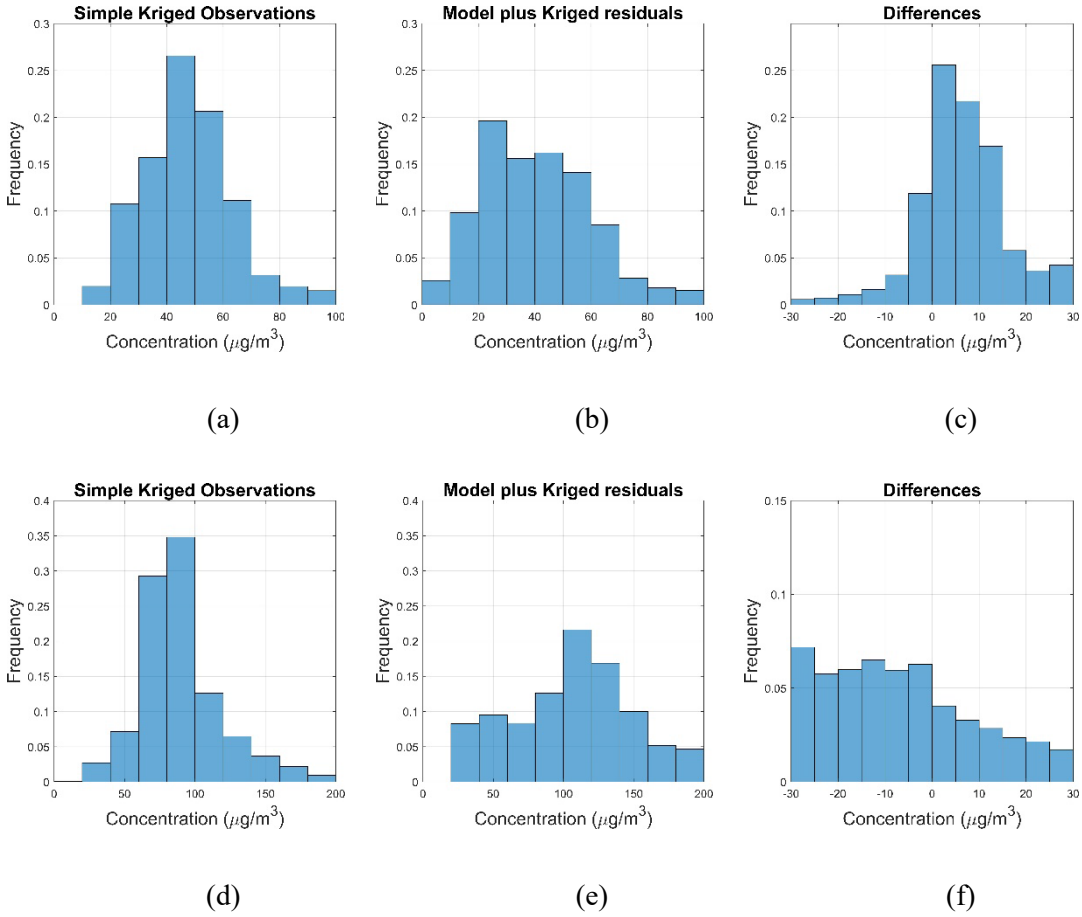

Figure 2.13. Histograms of PM2.5 concentrations created by (a) Simple Kriged Observations on October 13, (b) Model (Equation 7) plus Kriged residuals on October 13, (c) Differences between the two estimates on October 13, (d) Simple Kriged Observations on November 13, (e) Model (Equation 7) plus Kriged residuals on November 13, (f) Differences between the two estimates on November 13

2.5 Conclusions

This chapter presents an approach to construct highly resolved surface $PM_{2.5}$ maps by combining observations made at surface monitors and satellite data collected during wildfires. The method uses models to fill in the gaps in the measured data. Surface observations are first described using two dispersion models: a Lagrangian model based on backward trajectories from source to receptor and a segmented plume model that transports emissions from the source within a large-scale plume, whose horizontal dimensions are governed by trajectories originating from the sources. Estimates from these two models are fitted to surface observations to obtain emissions rates from sources. The satellite measurements of AOD, which measures column integrated $PM_{2.5}$, are also fitted to surface observations using an empirical power law model. Because the results from the Lagrangian model are similar to those from the Plume model, the computationally efficient Plume model is used in most of the analysis.

The AOD model and the Plume model are then combined linearly to describe surface $PM_{2.5}$ observations. The AOD model makes a contribution to the correlation, R^2 ,between model estimates and surface observations; the contribution is relatively small on most days, but can be significant on some days.

This model is used to construct 1 km resolved maps of surface $PM_{2.5}$ concentration during the October 2017 fires and the 2018 Camp Fire in Northern California. These maps interpolate between observations by combining model estimates with Kriged residuals between model estimates and observations. The residual Kriging

maps show greater spatial variation than that from simple Kriging, which just interpolates the measured concentrations.

The proposed approach to creating highly resolved maps (1 km by 1 km grid size) of surface $PM_{2.5}$ is a valuable contribution to estimating health risks associated with wildfires, when ground-level concentrations of $PM_{2.5}$ can be well above the 24 hour standard of 35 $\mu g/m^3$. In principle, the plume dispersion model is simple enough to allow updating of the parameters, horizontal plume spread and effective emission rate, in real time, which suggests that it can complement or be incorporated into a system (Marsha & Larkin, 2019 for example) to forecast ground-level $PM_{2.5}$ during wildfires.

3. Quantifying and Monitoring Methane Emissions from Dairy Farms in California Using TROPOMI and EM27/SUN Measurements

3.1 Introduction

Atmospheric methane (CH_4) concentrations have increased by a factor of 2.5 since preindustrial times and is now responsible for the second largest radiative forcing after carbon dioxide (IPCC, 2013). Anthropogenic CH_4 emissions are estimated to account for 50 to 65% of the total CH_4 emissions globally (IPCC, 2013), and they may be responsible for the increase in global CH_4 concentrations since 2007 (Kirschke et al., 2013; Luther et al., 2019). CH_4 emissions from agriculture and waste are estimated at 195 Tg/yr globally, accounting for 57% of total anthropogenic emissions (Marielle Saunois et al., 2016). The US national greenhouse gas emission inventory reports that CH_4 emissions from US agricultural activities increased by 16.2% between 1990 and 2018 (EPA, 2020). Additionally, from 2000 to 2017, dairy farm emissions in California have increased by 16% in the state's inventory (CARB, 2020). Dairy facilities account for roughly 60% of agricultural GHG emissions, while livestock contributes nearly half of the CH_4 emissions in California (CARB, 2020; Maasakkers et al., 2016). California's Senate Bill 1383 requires livestock manure CH_4 emissions to be reduced below 2013 levels by 2030 (CARB, 2016a).

Despite the significance of global and regional CH_4 emissions, estimates of CH_4 emissions from point sources are highly uncertain due to lack of sufficiently fine

resolution observations from either space-based or in situ observations (Jongaramrungruang et al., 2019). Jeong et al. (2016) and Cui et al. (2019) applied a Bayesian inverse model to multitower observations in California to suggest that total state annual CH_4 emissions are 1.2 - 1.8 and 1.14 - 1.47 times higher than the California Air Resources Board (CARB) emission inventories.

Methane emissions are commonly estimated by bottom-up methods or top-down methods. Bottom-up methods refer to methods that use the physical and chemical characteristics of the source to estimate CH_4 emissions (Allen, 2014). For example, the US Environmental Protection Agency (US EPA) (US-EPA, 2017) and the CARB (CARB, 2015) suggest methods that estimate CH_4 emissions from manure lagoons using number of livestock animals house at a dairy farm, manure management information, and an empirical factor that converts volatile solids to CH_4. These bottom-up methods have large uncertainties due to uncertainty in cow population, manure management strategies, and most importantly the empirical CH_4 emission factor based on a small sample of measurements (Marklein et al., 2020).

Top-down methods estimate CH_4 emissions from ambient observations of CH_4 made on towers, mobile platforms, and satellites (Amini et al., 2022; Chen et al., 2016; Cui et al., 2017; Heerah et al., 2021; Jeong et al., 2016; Viatte et al., 2017). This chapter focuses on a method to infer methane emissions from column averaged CH_4 mixing ratios measured with satellites and a surface-based instrument, the EM27/SUN, which uses solar absorption spectroscopy along the atmospheric path from the instrument to the sun. Heerah et al. (2021) used EM27/SUN measurements to infer CH_4 emissions from the San

Joaquin valley, a spatial scale that is an order of magnitude larger than that addressed in this study. A number of studies have estimated methane emissions from CH_4 mixing ratios averaged over atmospheric columns measured using a variety of instruments, such as ground-based spectrometers (Chen et al., 2016; Gisi et al., 2012; Viatte et al., 2017), aircraft remote sensing instruments (Frankenberg et al., 2016; Thorpe et al., 2016), and satellites (Jacob et al., 2022; Jacobs et al., 2020; Qu et al., 2021). Because the entire atmospheric column is measured, column-averaged measurements are believed to be less sensitive to vertical and near-surface transport of methane that affect interpretation of point methane concentrations (Heerah et al., 2021; Lauvaux and Davis, 2014).

Several methods have been used to estimate point source or area source CH_4 emission rates from column observations. Chen et al. (2016) and Jacob et al. (2016) used a simple mass balance to infer area source emission rates. This balance essentially equates the difference in the mole fractions of CH_4 between the downwind and upwind receptors to the product of unknown emission rate, the time taken for air to travel over the source and the total source area. Frankenberg et al. (2016) inferred emissions from a point source by assuming that the integral of the product of the vertical profiles of concentration and horizontal wind speeds is approximated by the product of an effective wind speed and the vertically integrated methane enhancement retrieved from a remote instrument (Bovensmann et al., 2010; Varon et al., 2018).

Methods that infer emissions from column average methane concentrations make assumptions about the wind fields and source geometry that lead to uncertainty in the corresponding emission estimates. Varon et al. (2018) has developed a semi-empirical

method that purports to overcome some of the major uncertainty in currently used methods of estimating emissions from point sources especially when the estimates are based on instantaneous images of plumes. The motivation to develop the method described in this chapter is to account for the geometry of the source, the geometry of the column measurements, and the micrometeorology of the atmospheric boundary layer. The detailed treatment of the governing processes avoids some of the assumptions made in previous estimates of emission rates. We estimate CH_4 emissions from sources distributed over scales of the order of 10 kilometers using remotely sensed column measurements of methane enhancements. The data originate from four field campaigns conducted near Visalia, California located in central part of the state where the majority of dairy farms in the state are located. The objectives of this chapter are to: 1) show how a dispersion model with a detailed treatment of transport and dispersion can be used to quantify CH_4 emissions from area sources and the associated uncertainty using column-based measurements and 2) compare CH_4 emission estimates derived from two different sources: TROPOMI and the EM27/SUN instruments. This chapter is spilt into two major parts. The first part of the chapter describes the field campaigns and details of the numerical model (chapter 3.2). Then the second part discusses the emission results from EM27/SUN and TROPOMI sequentially (chapter 3.3).

3.2 Data and Methods

3.2.1 Site

We measured the column-averaged dry-air mole fractions of CH_4 (XCH_4) in an area with a cluster of dairy farms north of Visalia located in California's San Joaquin

Valley (SJV) (Figure 3.1). We deployed EM27/SUN instruments at the northwest (NW) and southeast (SE) corners of the study area. Because the dominant wind direction in Visalia during the study was northwest, instruments were well positioned to make simultaneous $XCH4$ measurements of the background and downwind of the dairy farms. The direct distance between the NW and SE sites is approximately 15 km. Surface micrometeorology was measured using a CSAT3 3-D sonic anemometer on a 10 m tower located in one of the dairy farms in the cluster.

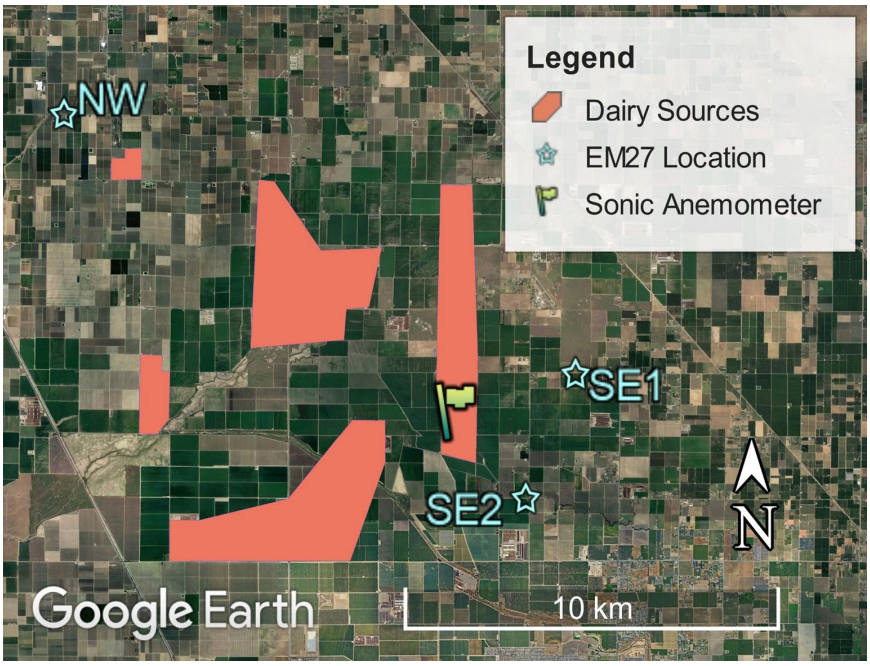

Figure 3.1. Locations of dairy facilities and deployed instruments in the study area. SE1 and SE2 are two different setup locations at southeast corners.

Four field campaigns were conducted to monitor the change in the CH_4 emissions from the dairy farms. The EM27/SUN deployment schedule and placement is listed in Table 3.1. We deployed two EM27/SUN owned by Los Alamos National Lab and NASA's Jet Propulsion Lab in the first three campaigns (March 2019, June 2019, and

September 2019). An additional EM27/SUN provided by Harvard University was deployed in January 2020.

Table 3.1. EM27/SUN working schedule and setup configuration

Date	Measurement Time (Local Time)	Location
03/25/2019	10:50 to 18:11	SE2, NW
03/26/2019	10:45 to 17:45	SE2, NW
03/29/2019	11:00 to 18:20	SE2, NW
06/21/2019	10:00 to 18:00	SE2, NW
06/22/2019	11:00 to 19:00	SE2, NW
09/11/2019	11:00 to 18:00	SE2, NW
09/13/2019	11:00 to 18:00	SE2, NW
09/14/2019	8:00 to 17:00	SE2, NW
09/17/2019	10:30 to 18:00	SE2, NW
01/23/2020	11:30 to 16:00	SE1 *, SE2, NW
01/28/2020	10:00 to 16:00	SE1 *, SE2, NW
01/31/2020	10:00 to 15:30	SE1 *, SE2, NW

*EM27/SUN was deployed in the third location in January 2020.

3.2.2 EM27/SUN measurements

The EM27/SUN is a compact and transportable solar tracking FTS. Column-averaged dry-air mole fractions of gases *(X_{gas})* are retrieved with the instrument by using

solar absorption spectroscopy along the atmospheric path from the instrument to the sun. It takes 5.8s to complete one forward/backward scan and the instrument has a 1σ running precision of 0.06% for XCH_4 (Chen et al., 2016; Hedelius et al., 2016). The raw XCH_4 measurements from the EM27/SUN were retrieved from double-sided interferograms using the GGG and I2S software (Wunch et al., 2015) and EGI processing suite (Hedelius et al., 2016). All the EM27/SUN instruments were calibrated to remove systematic offsets at the NASA Armstrong TCCON site or the Californian Institute of Technology TCCON site. The TCCON instruments are part of a network of high-resolution solar Fourier transform spectrometers, which are tied to the World Meteorological Organization (WMO) trace gas scale using aircraft concentration profiles. We found that the coefficient of determination R^2 of the calibrations between our instruments and TCCON sites was higher than 0.96, indicating that our instruments correlated well with TCCON (Heerah et al., 2021).

Examples of the raw XCH_4 measurements collected in the four campaigns are shown in Figure 3.2. We see that the XCH_4 at the downwind site (SE1 or SE2) are generally larger than those measured at the upwind site (NW), indicating the contribution of CH_4 emissions from the dairy farms. The dispersion model used 30-minute averaged differential column wind measurements between SE and NW (NW and SE) measurements to infer the emissions.

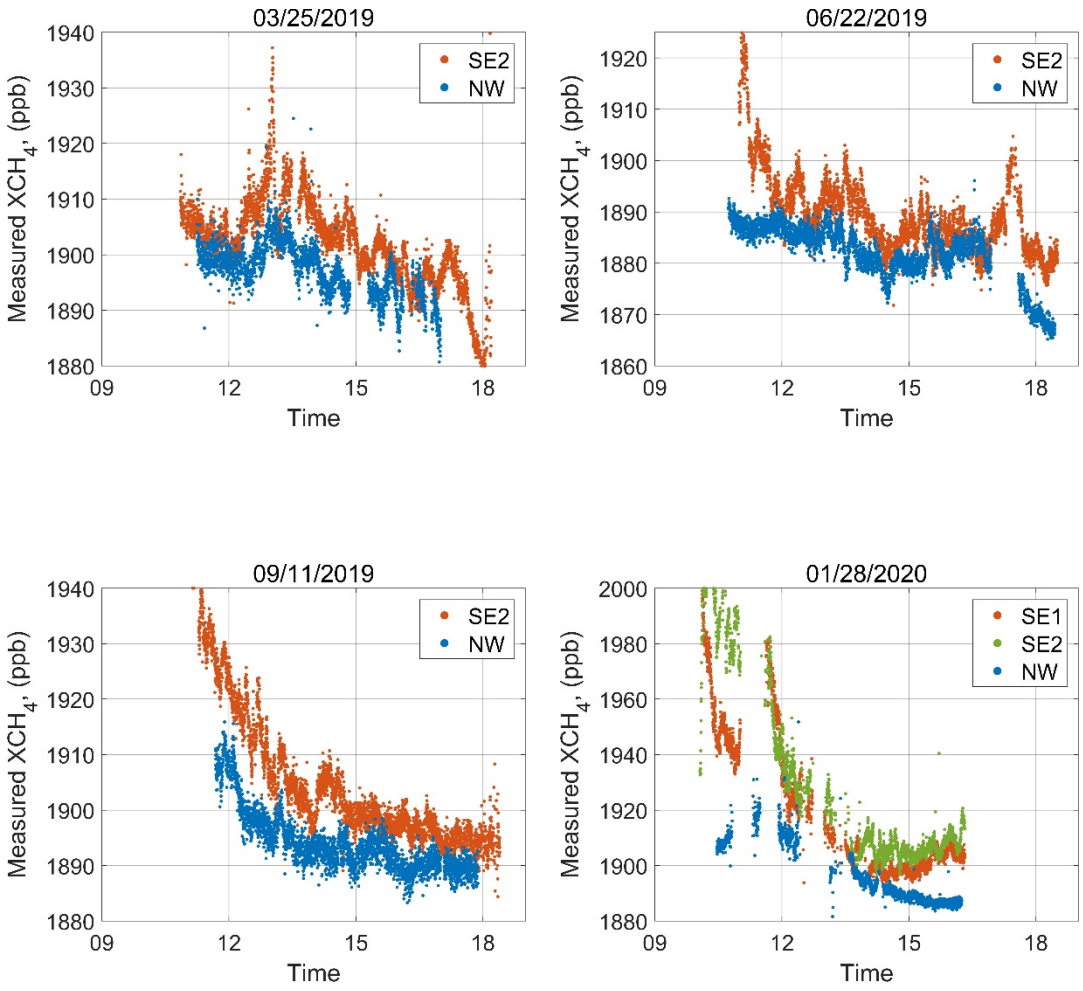

Figure 3.2. EM27/SUN raw measurements collected in March 2019, June 2019, September 2019, and January 2020. For each month, we show one day of measurements as an example.

3.2.3 Meteorological measurements

The micrometeorological data was measured with a CSAT3 3-D sonic anemometer mounted at 10 m. The instrument recorded 3d winds and temperature at 20Hz. The data from the sonic anemometer were processed to obtain the micrometeorological variables, the friction velocity (u_*), the kinematic heat flux (Q_o), and the Monin-Obukhov length (L) required by the dispersion model. The boundary layer height was estimated with AERMET, the meteorological processor of the American

Meteorological. Society and U.S. Environmental. Protection. Agency Regulatory Model (AERMOD) (Cimorelli et al., 2005). The averaged meteorological measurements collected over four different seasons are shown in Table 2.2. We also used the High-Resolution Rapid Refresh (HRRR) model as the source of meteorological data to model CH_4 emissions based on column-averaged observations by TROPOMI (Blaylock et al., 2017; Rolph et al., 2017b). The HRRR model provides 3-km resolved hourly meteorological data that includes 3-dimensional wind fields, surface temperature *(T),* surface friction velocity *(u_*),* surface heat flux (Q_o), and the boundary height (z_i).

Table 3.2. Meteorological data collected from 10 m sonic anemometer averaged during 9:00 to 18:00 (local time)

Measurement Period	**Wind Speed** (m/s)	**Wind Direction** (°)	u_* (m/s)	T ($°C$)	L (m)	Q_o ($K \cdot m/s$)	z_i (m)
March 25 - March 30, 2019	2.19	316	0.28	17.92	-43.93	0.06	611
June 18 – June 27, 2019	3.29	288	0.29	30.27	-23.48	0.11	900
September 11 - September 17, 2019	2.35	307	0.24	26.41	-29.35	0.07	718
January 21- February 02, 2020	1.79	308	0.18	12.61	-25.86	0.03	365

Our modeling framework assumes that mean winds in the study area are spatially homogeneous over a horizontal scale of 10 km. To evaluate the degree to which this

assumption was met, we used the 10 m wind data collected at Visalia Municipal Airport (~11 km from the sonic anemometer location), which is part of the Automated Surface Observing System (ASOS). We compared the ASOS measurements with sonic anemometer measurements and HRRR wind data at the sonic anemometer location (Figure 3.3). The 5-minute data from 10:00 to 18:00 local time during the complete measurement days was used for sonic anemometer comparisons (left panel) and hourly averaged data was used for HRRR comparisons (right panel) during the campaign periods. The R^2 with the ASOS data is 0.64 and 0.55 for the sonic anemometer and HRRR data, respectively. The scatter suggested by these correlation coefficients between different sources of wind fields has bearing on the uncertainty in the inferred emission rates.

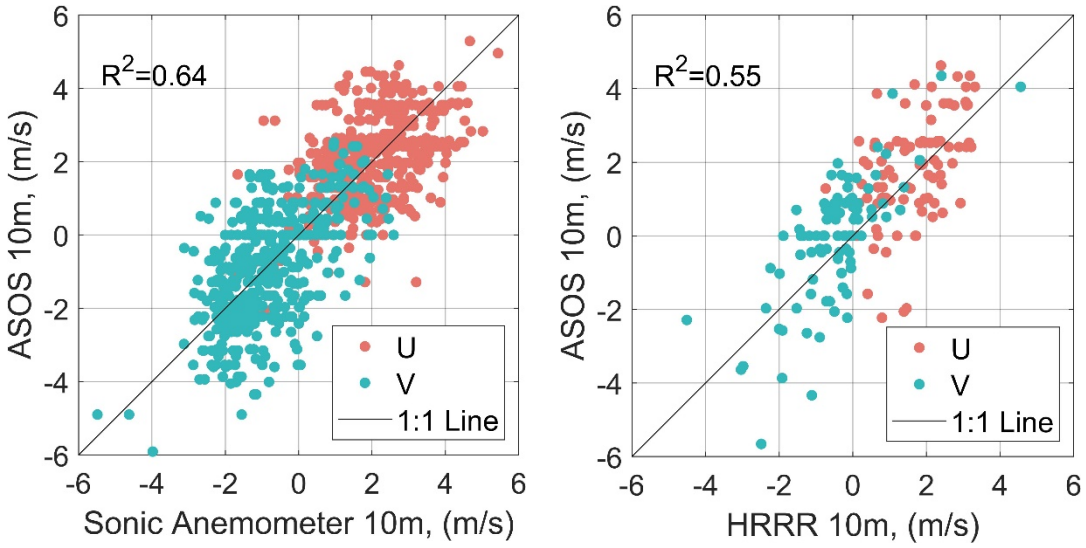

Figure 3.3. 10-m wind comparison: ASOS (Visalia Municipal Airport site) versus the sonic anemometer (left panel) and ASOS versus HRRR (right panel). Positive U and V components represent the east and north directions.

Different methods were used to examine the vertical distribution of the wind speeds (Figure 3.4). Measurements were made with radiosondes that were launched in the morning and evening near the sonic anemometer location during the March campaign. We also accessed hourly wind observations from a 915-MHz boundary-layer profiler provided by NOAA Physical Sciences Laboratory. Its vertical coverage ranges from 120 m to 4000 m with approximately 62 m vertical resolution and 0.99 m/s precision (Angevine et al., 1998).

Modeled wind profiles were obtained from the HRRR model, which predicts wind profiles at 25-minibar pressure intervals from the surface. A similarity wind profile was also generated using the 10 m sonic anemometer data following Businger (1973).

The wind speeds from the Visalia radar wind profiler, radiosonde, and HRRR show a similar increasing trend with height on March 29th morning, however the similarity wind profile underpredicts the wind speed compared to the other measurements. This indicates the need to combine the similarity wind profiles from surface measurements with wind profiles observed at higher altitudes in applying the dispersion model, described in the next section.

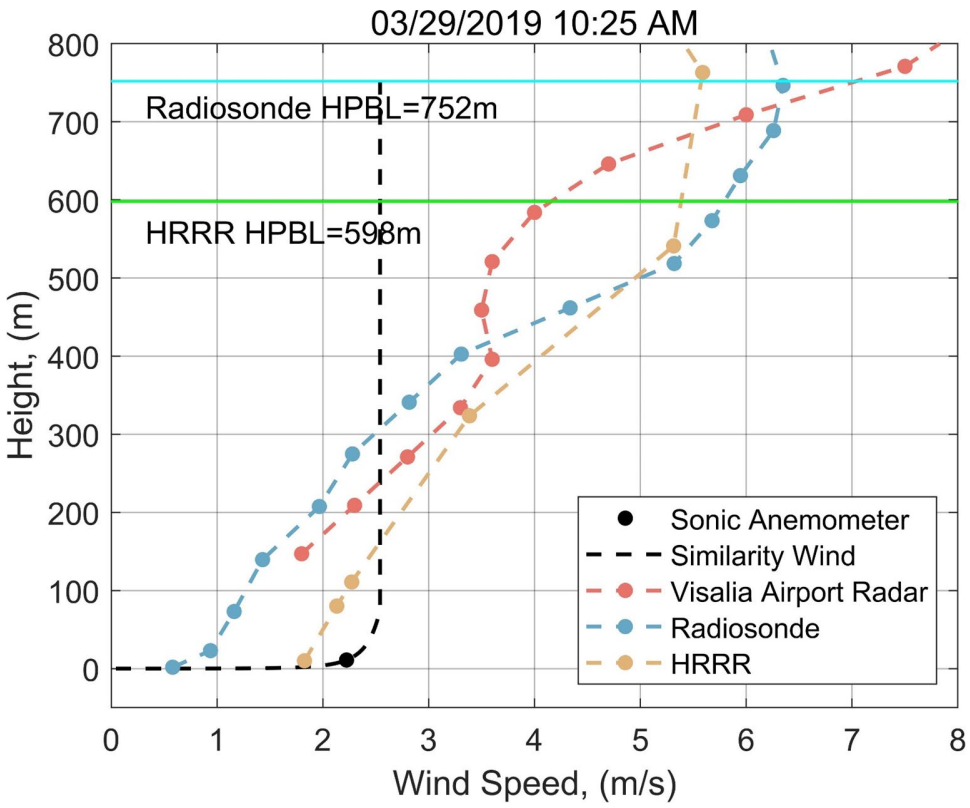

Figure 3.4. Comparison of vertical wind speed observations and predictions on one study day.

3.2.4 Interpretation of data using a dispersion model

The data collected in the field study was used to infer emissions from the manure lagoons by fitting results from a dispersion model to the measurements. Details of the dispersion model and the fitting procedure are described next.

The contribution of emissions from a surface-based area source, such as a manure lagoon, to the concentration at a receptor at (x_r, y_r, z_r) is computed by representing the area by a set of line sources.

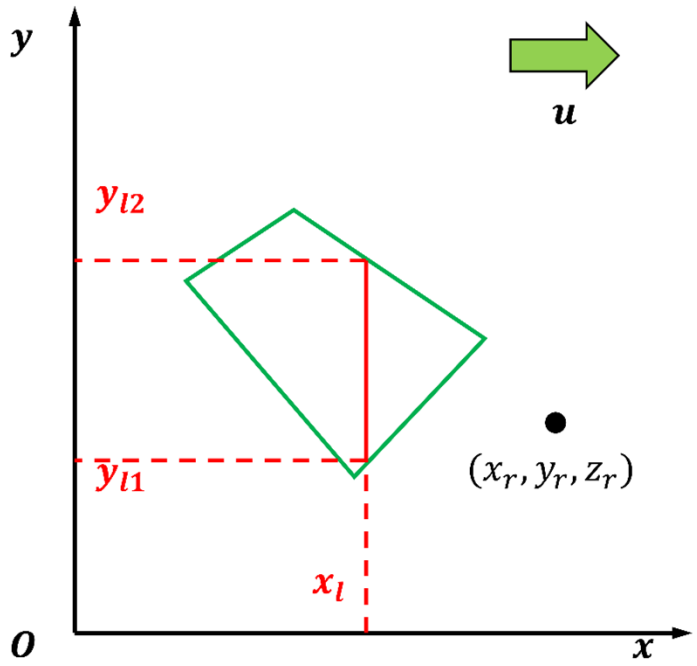

Figure 3.5. Area source representation

As shown in Figure 3.5, each line source spans the area source and is placed perpendicular to the near surface wind speed; the x-axis of the co-ordinate system is parallel to the direction of the surface wind speed. This allows us to compute the contribution of each line source to the concentration at the receptor using the expression (Venkatram and Horst, 2006)

$$C(x_r, y_r, z_r) = qF_z(x_r - x_l, z_r)\frac{erf(t_2) - erf(t_1)}{2} \tag{3.1}$$

where q is the emission rate per unit length of line source, x_r, y_r and z_r, are the co-ordinates of the receptor, x_l is the x-co-ordinate of the line source, and

$$t_i = \frac{y_{li} - y_r}{\sqrt{2}\sigma_y(x_r - x_l)} \tag{3.2}$$

The y-co-ordinates of the beginning and end of the line source are y_{l1} and y_{l2}, and $\sigma_y(x_r - x_l)$ is the horizontal spread of the plume over the distance $x_r - x_l$.

The vertical distribution of the concentration is given by $F_z(x,z)$, which is commonly described with a Gaussian distribution. Nieuwstadt and Van Ulden (1980) show that the tracer concentrations measured during the classic Prairie Grass experiment. Barad (1958) indicates that the vertical concentration distribution is more nearly exponential than Gaussian during unstable conditions; it is close to Gaussian only under very stable conditions. They also show that the solution of the two-dimensional mass conservation provides an excellent description of the vertical distribution of concentration when the wind speed and eddy diffusivity are formulated using Monin-Obukhov similarity. Current formulations of plume spread draw upon this early work (Venkatram et al., 2011).

We use the numerical solution of the two-dimensional mass conservation equation to derive $F_z(x,z)$ because it provides a realistic description of the vertical distribution of concentrations associated with surface releases. The equation is

$$U(z)\frac{\partial F_z}{\partial x} = \frac{\partial}{\partial z}\left(K_z(z)\frac{\partial F_z}{\partial z}\right) \tag{3.3}$$

where the wind speed, $U(z)$, and eddy diffusivity, $K_z(z)$, are functions of micrometeorological variables in addition to z. These variables are the surface friction velocity, u_*, the Monin-Obukhov (MO) length, L, the surface roughness length, z_0, and the boundary layer height, z_i. We use formulations suggested by Businger (1973), based on MO similarity theory, to represent the wind, $U(z)$, for $z < 0.1z_i$ and the radar wind

profiler measurements for heights between $0.1z_i$ and z_i The eddy diffusivity profile $K(z)$ follows MO similarity for $z < 0.1z_i$, and then taken to be the value at $z = 0.1z_i$ above this height.

One of the attractive features of applying Equation (3.3) is that we can specify the vertical distributions of wind speed and eddy diffusivity to obtain the best description of the measured concentrations; the Gaussian distribution does not provide this flexibility. Note that the eddy diffusivity representation of vertical mixing is not realistic for elevated releases in the atmospheric boundary layer.

The boundary conditions for Equation (3.3) are

$$\frac{\partial F_z}{\partial z} = 0 \; at \; z = z_0 \; and \; z = z_i \tag{3.4}$$

where z_i is the boundary layer height. Equation (3.4) says that there is no vertical transport beyond the boundaries of the domain, (z_0, z_i).

The horizontal plume spread, σ_y, used in Equation (3.2) for the contribution of a line source is based on the expression suggested by Eckman (1994) and applied by Venkatram et al. (2013) to describe horizontal spread of plumes released during the Prairie Grass field study

$$\frac{d\sigma_y}{dx} = \frac{\sigma_v}{U(\bar{z})}$$

and

$$\bar{z}(x) = \frac{\int_{z_0}^{z_i} F_z(x,z) z dz}{\int_{z_0}^{z_i} F_z(x,z) dz} \tag{3.5}$$

where $\bar{z}$ is the center of mass of the vertical distribution $F_z(x, z)$ obtained from the solution of Equation (3.3), and $U(\bar{z})$ is the wind speed at the mean plume height by interpolating the value from the combined wind profile.

The horizontal domain used in the solution of Equation (3.3) extends from the minimum of the x-co-ordinates of corners of the area polygon to the receptor, x_r. The source of emissions is represented by a non-zero value of concentration at a near surface vertical level at $x = 0$ in the co-ordinate system used in the numerical solution of Equation (3.3); the resulting concentrations are normalized by the integral of the vertical distribution to yield F_z for a unit emission rate. The concentrations are computed on a two-dimensional grid at a fine enough spatial resolution to allow us to linearly interpolate the vertical distribution at any horizontal distance between a line source and receptor.

The contribution of the area source to the concentration at a receptor is computed by summing over contributions from the line sources used to represent the area source; the emission per unit length of the line sources is obtained by dividing the unit strength by the total length of the lines. This integration is conducted in steps in which the number of line sources is doubled in subsequent steps, and successive results compared. The integration is terminated when the relative error between successive integrals, extrapolated to zero distance between the line sources, is less than 10^{-4}.

This procedure is extended to compute the integral of the concentration along a specified line in three-dimensional space. This integral is required in interpreting data from the EM27/SUN instrument, which measures the integral of the methane concentration along the line joining the measuring instrument to the sun. The equation

describing the line can be expressed in terms of the azimuth and elevation angles of the sun.

This integral consists of two integrals: the first integrating the contributions from the line sources from the area sources to the concentration at a receptor along the path, and the second integrates these concentrations along the path. If it is assumed that the methane above the boundary layer is at background levels, the line integral is terminated at the top of the boundary layer.

As shown in Figure 3.6, the EM27/SUN measures the line integral of the CH_4 molar concentration normalized by the total molar mass of air per unit cross-sectional area along the line joining the instrument to the sun; this is the average mixing ratio of methane along this line of sight.

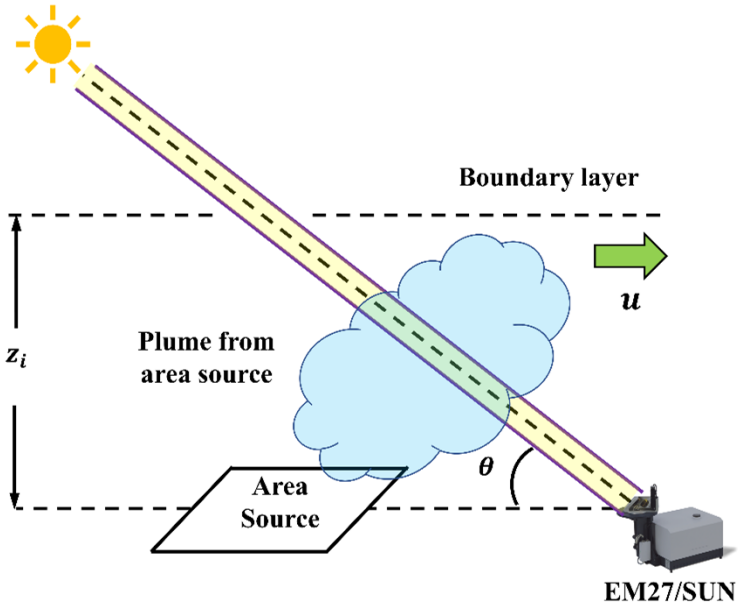

Figure 3.6. Atmospheric column geometry from the EM27/SUN measurement

The molar mass of air along the line of sight of the EM27/SUN is

The molar mass of air along the line of sight of the EM27/SUN is

$$Mass_{air} = \frac{p}{g \cdot sin(\theta) \cdot MW_{air}} \tag{3.6}$$

where p is the surface pressure, g is the acceleration due to gravity, θ is the sun's elevation angle, and MW_{air} is the molecular weight of air. Then the modeled value, X_{model}, that is compared to the measured value is

$$X_{model} = \int_0^{s_2} C_{model}\,(s\,(x,y,z))\,ds \frac{1}{MW_{CH_4} \cdot Mass_{air}} \tag{3.7}$$

where $s(x,y,z)$ describes the line joining the instrument to the sun, and s_2 is the upper limit of the integral where the line intersects the boundary layer height.

The unknown CH_4 emission rates from the dairy farms are estimated by fitting the differences in the values of EM27/SUN measurements made between the downwind and upwind locations to the corresponding modeled values, Δx, corresponding to unit emission rates

$$\Delta X_i = \sum_j \Delta x_{ij}\, Q_j + \varepsilon_i \tag{3.8}$$

where the subscript "*i*" denotes the measurement, "*j*" refers to the source area with the unknown emission rate, Q_j, and ε_i is the residual between the model estimate and the measured value. The emission rates Q_j are obtained by minimizing the sum of residual squared $\sum_i \varepsilon_i^2$ with the constraint that the Q_j values are greater than or equal to zero. To achieve this, we use the MATLAB function lsqnonneg described in Lawson and Hanson (1974).

The 95% confidence values of the emission rates are obtained using a version of bootstrapping in which the residuals are added randomly to the initial set of modeled

values to create a set of 'pseudo observations' (Ding et al., 2021). We created 1500 sets of pseudo measurements, which were then used to derive 1500 emission sets, Q_j, using Equation (3.5). The values of Q_j were then used to estimate the 95% confidence intervals.

3.3 Results and Discussion

3.3.1 Emissions from the EM27/SUN measurements

The performance of the model in fitting the observed XCH_4 enhancements between the upwind and downwind sites is measured with the R^2 between the modeled and observed values, the percentage of modeled values within a factor of 2 of the observed values (Fact2), geometric mean (m_g) and the geometric standard deviation (s_g) of the ratios of the modeled to the observed values (Venkatram et al., 2013b) m_g and are defined as

$$m_g = exp(\langle \varepsilon_m \rangle) \tag{3.9}$$

$$s_g = exp(\sigma(\varepsilon)) \tag{3.10}$$

where $\langle\rangle$ and σ represent average and standard deviation, respectively, and ε_m is the residual between the logarithms of model predictions and observations, given by

$$\varepsilon_m = ln(C_p) - ln(C_o) \tag{3.11}$$

m_g is a measure of the model bias; m_g greater (less) than unity indicates overestimation (underestimation) by the model. s_g is a measure of the uncertainty of modeled values and s_g^2 is an approximate measure of the 95% confidence interval of the ratio of modeled to measured values.

In order to capture the effective plume signals from the cluster dairy farms, the EM27/SUN dataset was filtered using wind direction and mole fraction differences. Only wind direction ranges from 270 to 360 degree with a positive mole fraction difference (SE-NW) or wind direction ranges from 0 to 90 degree with a positive mole fraction difference (NW-SE) were used to estimate emission rates.

The R^2 values between modeled and measured values of methane enhancement were 0.78, 0.45, 0.82, and 0.43 for March 2019, June 2019, September 2019, and January 2020, respectively (Figure 3.7). m_g ranges from 1.04 to 1.12 (relative to unity) and s_g from 1.66 to 2.49. Figure 3.8 compares the estimates from the dispersion model with the corresponding to EM27/SUN measured differential methane mole fractions. As seen in the figure, the dispersion model captures the variation of the measured ΔXCH_4 during the campaign periods.

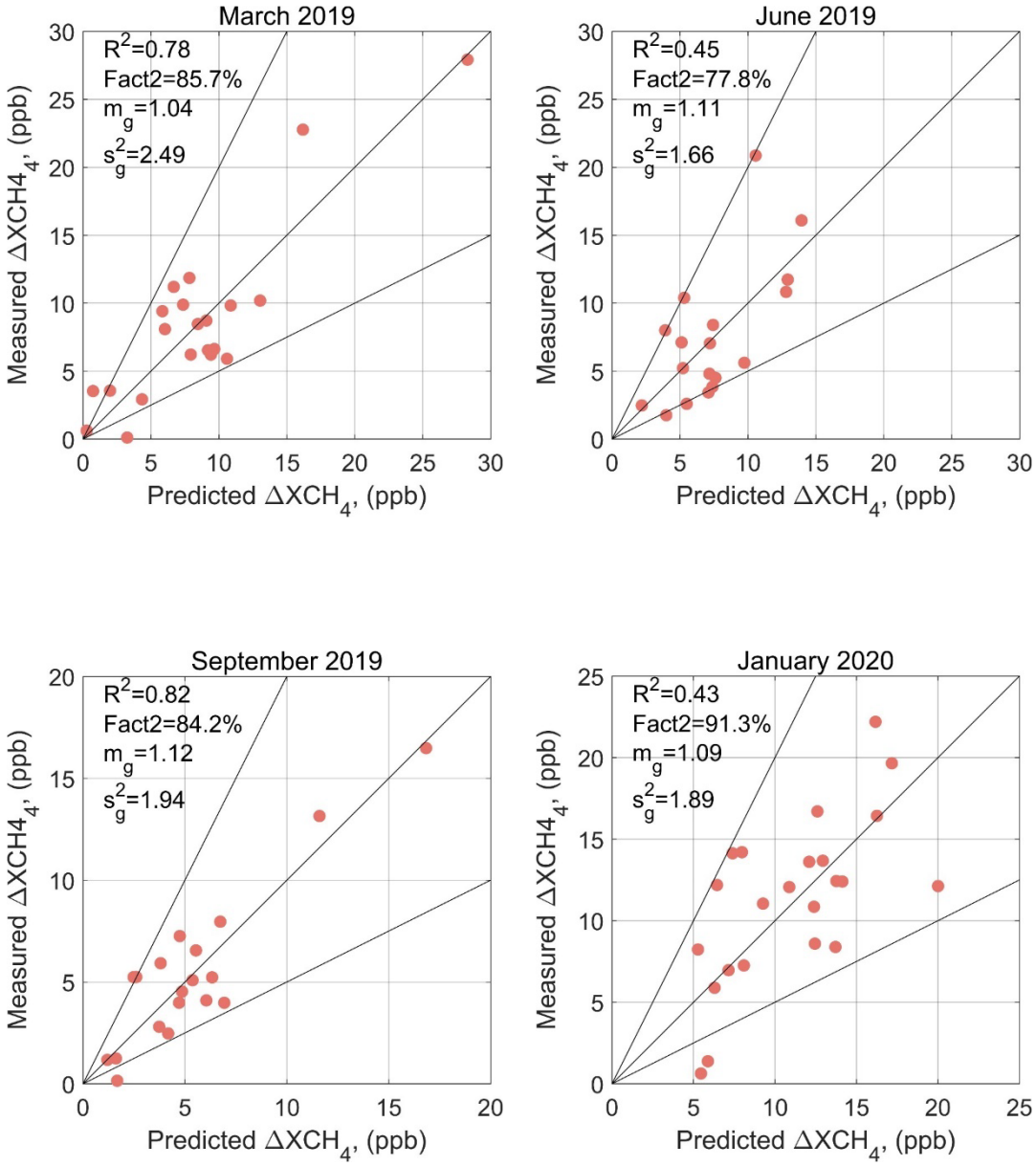

Figure 3.7. Scatter plots of EM27/SUN measurements and predictions from the dispersion model for all the campaigns

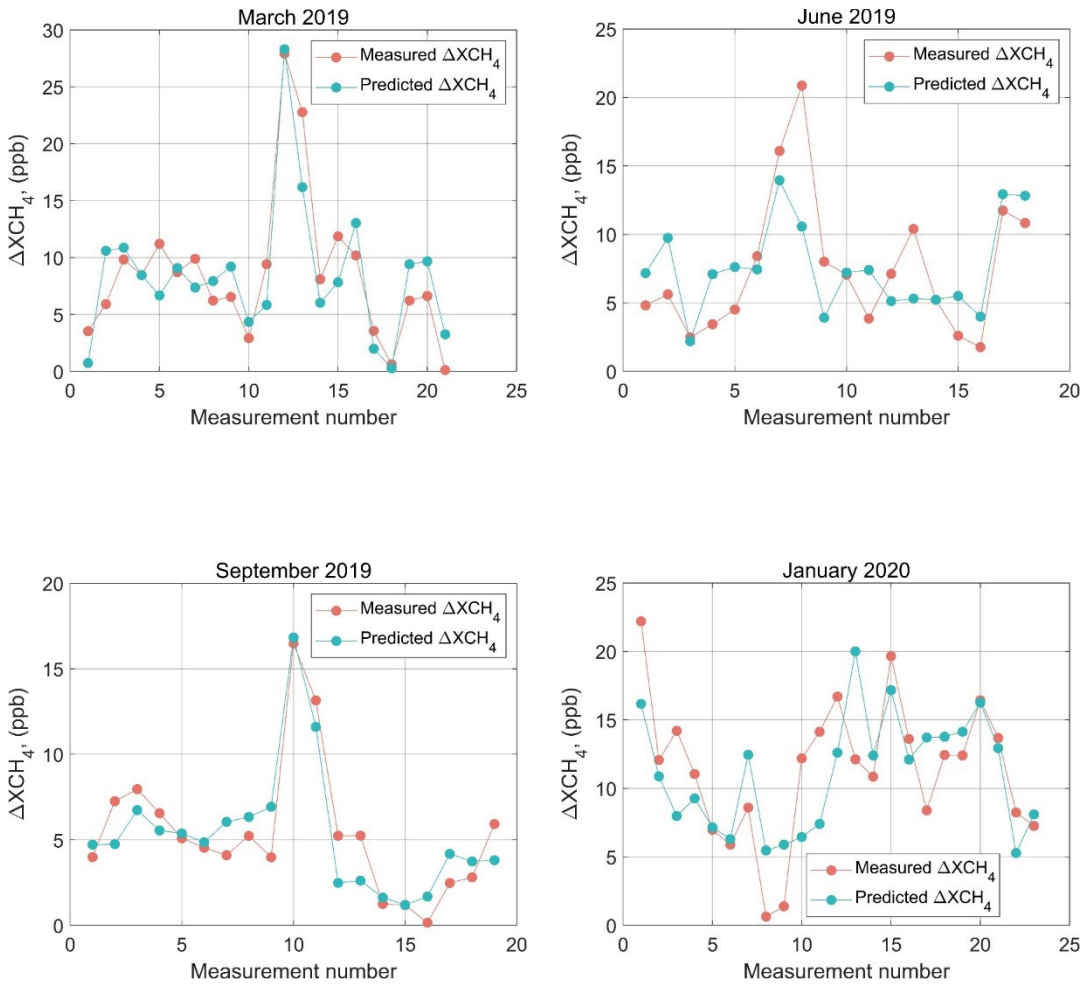

Figure 3.8. Comparisons of EM27 measurements and model estimates at the 30-minute averaged sampling points during the campaigns.

The model inferred CH_4 emissions driven by the EM27/SUN and 10 m sonic anemometer measurements as well as the 95% confidence intervals are shown in Table 3.3. We compare these values with the 'bottom-up' annual averaged emissions 25.3 Gg/yr estimated by Marklein et al. (2021) using populations and habits of the cows in the dairy farms being examined. These emissions include enteric fermentation emissions

based on dry matter intake by total cattle (Appuhamy and Kebreab, 2018) and manure emissions (Hristov et al., 2017).

The highest model inferred emission rate is 105.0 Gg/yr in the summer campaign, and the 95% confidence interval is 80.4 -119.1 Gg/yr. The best fit value is 4.2 times the prior bottom-up emission rate. The emission rates from the other three campaigns range from 43.7 to 49.8 Gg/yr, which are lower than that of June 2019. We notice that all of these emissions are at least 1.7 times higher than the bottom-up emission estimates.

Table 3.3. Inferred CH_4 emissions and uncertainties from all field campaigns

Time	Best Fit Emission (Gg/yr)	95% Confidence Intervals	Factor to Prior
March 2019	44.7	[41.3, 48.8]	1.8
June 2019	105.0	[80.4, 119.1]	4.2
September 2019	43.7	[39.4, 53.1]	1.7
January 2020	49.8	[46.7, 55.6]	2.0

3.3.2 Impact of modeled meteorology

Since meteorological data is not always available from the 3-D sonic, we examined the potential use of the HRRR meteorological data as an alternative. The EM27/SUN measurements during January 2020 were used in the evaluation, and the micrometeorological data from the sonic anemometer and HRRR model served as inputs to the dispersion model respectively.

The meteorological datasets were obtained from the HRRR model, which was then interpolated at the location corresponding to the sonic anemometer using a linear 2-D scattered scheme. We used the hourly HRRR data including the surface temperature at

2 m (T), the surface friction velocity (u_*), the kinematic heat flux (Q_o), and the mixed layer height, z_i. The vertical velocity profiles were constructed from wind vectors (u, v) at 10 m, 80 m, 1000 mbar height (~111 m) and levels at 25 mbar intervals (~220 m) up to a height of 775 mbar (~1950 m).

The crosswind turbulence velocity required by the dispersion model is estimated from the relationship (Venkatram and Princevac, 2008)

$$\sigma_v = (\sigma_{vc}^3 + \sigma_{vm}^3)^{\frac{1}{3}} \tag{3.12}$$

where $\sigma_{vm} = 1.9u_*$ for the mechanical component as in Hicks (1984), and the convective component σ_{vc} is given by (Isakov et al., 2007)

$$\sigma_{vc} = 0.6\left(\frac{g \cdot z_i \cdot Q_o}{T}\right)^{\frac{1}{3}}, when\ Q_o > 0$$

and (3.13)

$$\sigma_{vc} = 0, when\ Q_o \leq 0$$

Figure 3.9 compares the σ_v values computed from Equation (3.12) and (3.13) at the locations of the 3D sonic anemometer to measurements from the sonic anemometer. The impact of such differences in modeled and measured micrometeorology was assessed through differences in the corresponding inferred methane emission rates, shown in the violin plots of Figure 3.10.

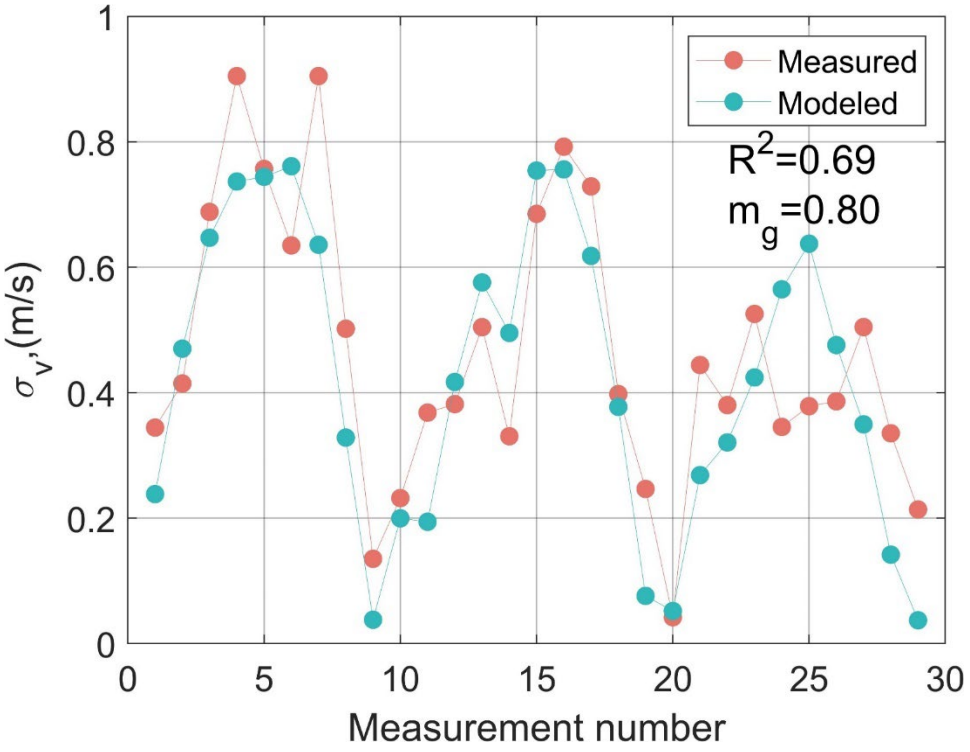

Figure 3.9. Comparison of horizontal velocity fluctuations (σ_v) measured with 3D sonic anemometer with values inferred from HRRR model results using Equation (9)

We see from the violin plot that the HRRR meteorology yields slight overestimates of CH_4 emissions relative to those based on sonic anemometer measurements; however, the uncertainty of the emission estimates based on the HRRR data are larger than those based on the sonic measurements.

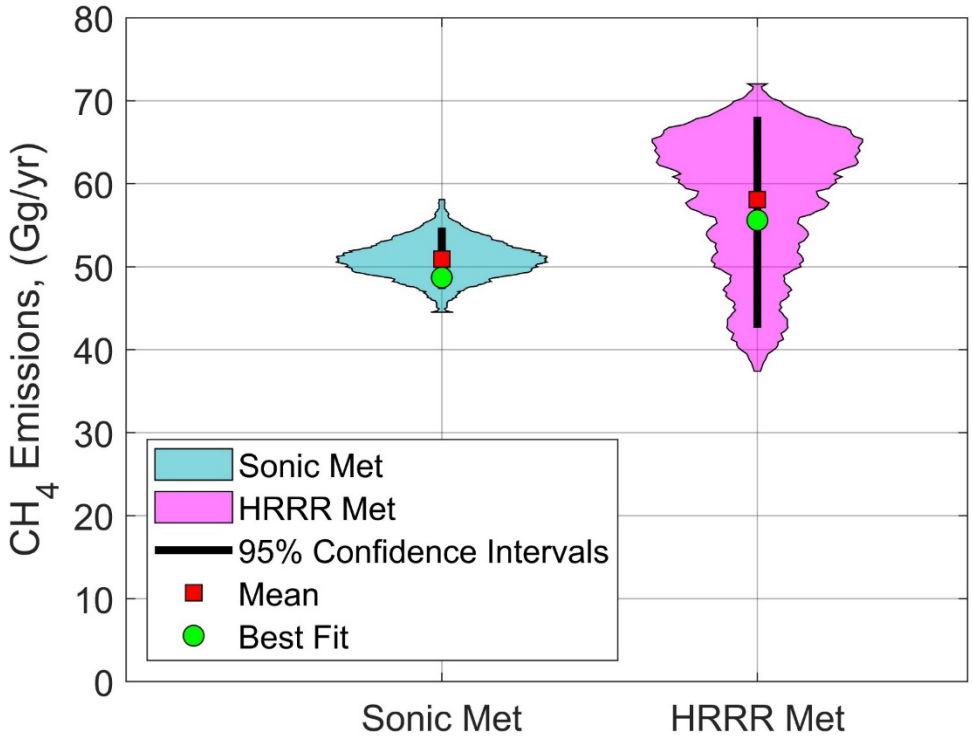

Figure 3.10. Violin plot of CH_4 emissions estimates using different meteorological (Met) data in January 2020. The width of the color region represents the frequency of the fitted emissions, while the best fit emissions are determined using non-negative least squares regression.

3.3.3 TROPOMI based emissions

CH_4 emission rates were also estimated by the dispersion model using instantaneous column measurements from the TROPOMI instrument mounted on a satellite that passes over the study area once a day at 13:30 local solar time. The TROPOspheric Monitoring Instrument (TROPOMI) is one of the current instruments on board the Sentinel 5 satellite, which can measure a wide range of atmospheric pollutants including nitrogen dioxide (NO_2), ozone (O_3), sulfur dioxide (SO_2), and methane (CH_4). TROPOMI measures the column-averaged gas concentration using backscattered sunlight in the shortwave-inferred (SWIR) spectral range (Butz et al., 2012).

TROPOMI, launched in October 2017, provides daily global measurements at approximately 13:30 local solar time with the resolution of 7×7 km^2, which was upgraded to 5.5×7 km^2 in August 2019. Lorente et al. (2021) and Hasekamp et al. (2019) estimate the global mean bias and station-to-station variability between TROPOMI and the ground based Total Carbon Column Observing Network (TCCON) to be -3.4 ± 5.6 ppb and -4.3 ± 7.4 ppb for CH_4 specifically. Several studies have used TROPOMI measurements to estimate CH_4 emissions estimates (Qu et al., 2021; Varon et al., 2019) even though only 3% of the data over land has been useful because of hazy atmosphere or low surface reflectance (Jacob et al., 2022).

The spatial resolution provided by TRPOMI was 7×7 km^2 during the first part of the study and was then to upgraded to 5.5×7 km^2 after August 2019 (Siddans and Smith, 2018). We realize that this spatial resolution might reduce the magnitudes of the gradients of CH_4 mole fractions created by emissions from the dairy cluster.

We studied the time period between January 1st 2019 and August 31st 2020. Only 108 out of 608 (18%) of the study days in this period had non-zero quality values that could be analyzed with the dispersion model. The satellite metadata files provide the viewing azimuth and the solar zenith angles, which are used by the dispersion model to compute the CH_4 concentrations along the line of sight from the observation point to the sun. An example of the instantaneous TROPOMI observations without interpolation over the study area is plotted in Figure 3.11. The upwind and downwind XCH_4 from TROPOMI correspond to locations nearest to those of the EM27/SUN instruments. The XCH_4 gradient associated with methane emissions from diary cluster between SE2 and

NW is clearly seen in the image. During the period that TROPOMI passes over this area, the HRRR wind direction in this region was 301 degrees which is consistent with the presence of this XCH_4 gradient.

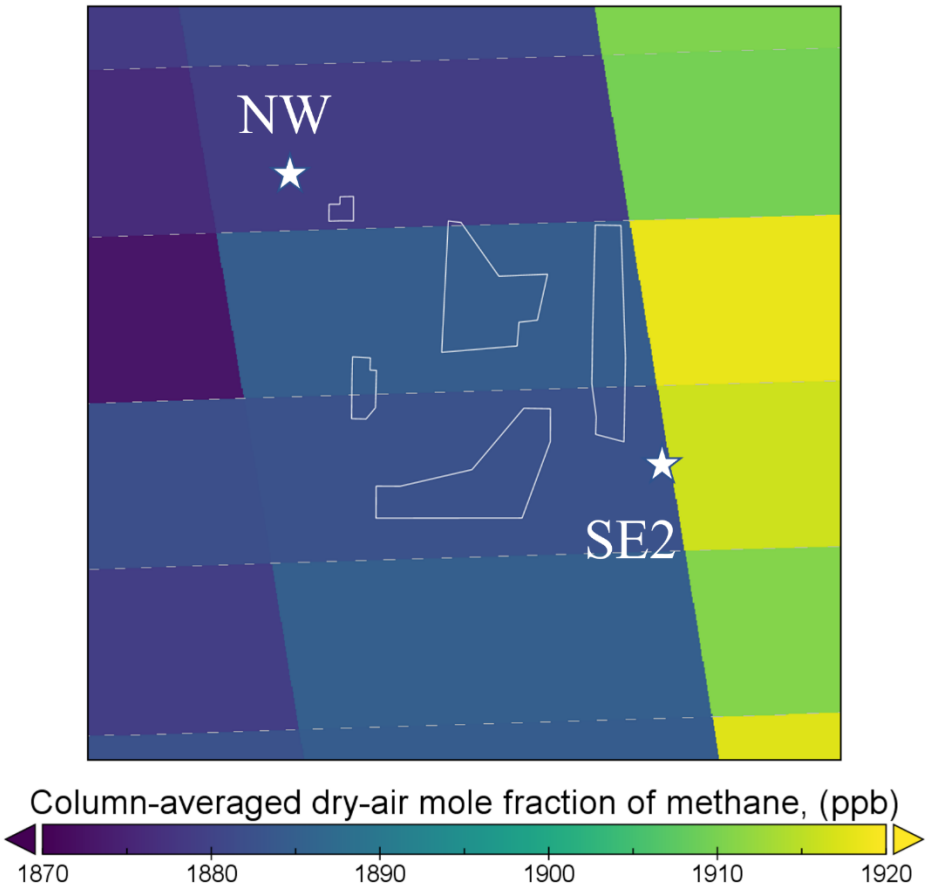

Figure 3.11. TROPOMI observations of column-averaged dry-air mole fractions XCH_4 in the study area. The white polygons denote the clusters of dairy facilities, and the stars represent TROPOMI model observation locations.

Table 3.4 presents the emissions from the two sources, normalized by the head of milk cows. We see that emissions based on the EM27/SUN and TROPOMI data are close to each other. Both of them are more than twice as high as the "bottom up" estimates (Maasakkers et al., 2016) and those from the CARB GHG inventory (CARB, 2015). The

timeseries of CH_4 emissions estimated from TROPOMI measurements and EM27/SUN are shown in Figure 3.12. Monthly averaged emissions in June, July, and August 2020 are 47, 71, and 91Gg/yr respectively.

The uncertainty in the TROPOMI derived emissions is obtained from satellite observation standard errors, and the 95% confidence intervals of EM27/SUN determined by the bootstrapping method described earlier. During overlapping time periods, the differences in the fitted emission estimates derived from the EM27/SUN and the TROPOMI values are much smaller than the uncertainties in the emission estimates. The EM27/SUN based seasonal methane emissions, shown in Table 3.4, are likely to be higher during the summer than in the other seasons, which is consistent with seasonal variation of emissions of a California-specific a priori model estimated by Jeong et al. (2012). One possible reason for higher emissions in summer could be the higher ambient temperatures (Table 3.2) during summer accompanied by higher pond temperatures, which in turn result in increased CH_4 production (Mangino et al., 2002; McMillan et al., 2007). Our stringer summer seasonal source results differ with those reported by Heerah et al. (2021) using EM27/SUN deployed in the same region at large scales and were attributed to greater soil moisture in winter. This is possibly due to our sampling of lagoon CH4 emissions at the smaller scales that are not water limited. These results suggest that more studies are needed to investigate the mechanism of CH_4 production in dairy ponds and the effect of temperature on emissions.

Table 3.4. CH_4 emissions per head and uncertainties comparisons in March 2019

	CH4 Emissions Per Head (kg/yr)	95% Confidence Interval
EM27/SUN	475	[447, 575]
TROPOMI	507	[436, 583]
Prior	271	[141, 401]
CARB	187	-

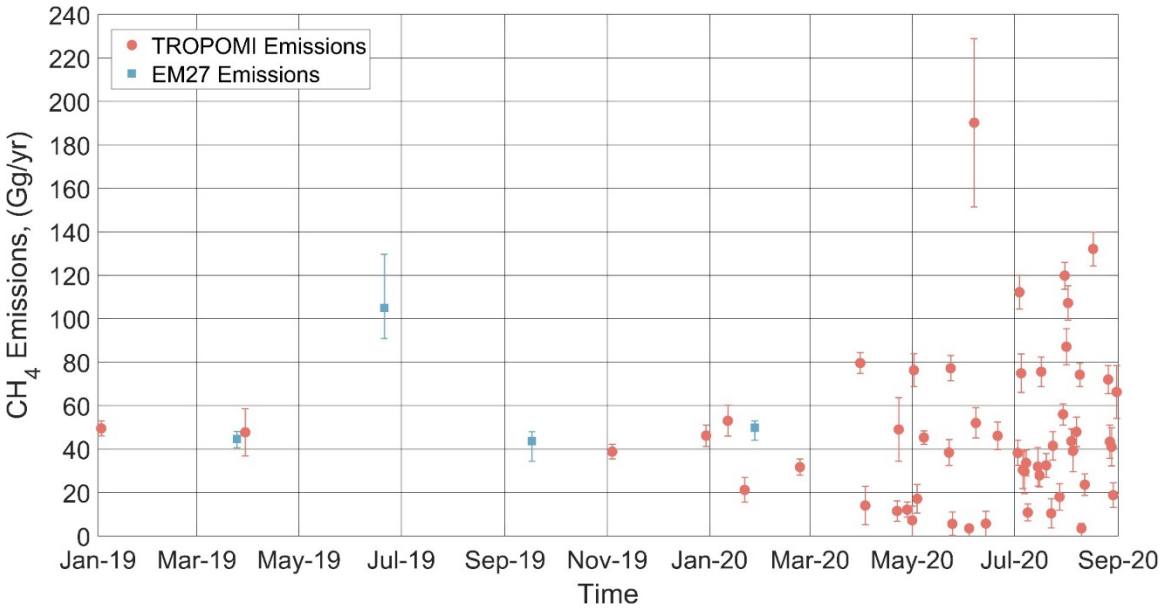

Figure 3.12. The time series of inferred emissions from TROPOMI remote sensed observations and EM27/SUN.

3.4 Conclusions

This chapter demonstrates the application of a numerical dispersion model to infer methane emissions from a dairy cluster using column-averaged methane measurements upwind and downwind of the cluster. The model accounts for the geometry of the sources and the mean and turbulent structure of the atmospheric boundary layer in estimating concentrations associated with area sources of methane. The model also pays attention to the details of the geometry of the remote measurement method. The numerical model

allows a straightforward incorporation of the vertical structure of the boundary layer into the model inputs to describe the three-dimensional concentration field resulting from an area source of emissions. This concentration field is then used to compute the average concentration along the line joining the instrument and the sun. The application is restricted to a horizontal spatial scale of the order of 10 kilometers over which the vertical structure of the boundary layer is assumed to be invariant.

Because onsite meteorological inputs are not routinely available, we examined the use of these inputs derived from the HRRR model. The emissions derived from these inputs were compared with those based on-site measurements. Although the emissions estimated using these two methods were similar, the HRRR modeled inputs introduced larger uncertainty in the emission estimates.

The model was also applied to two sets of methane measurements, one from a ground-based EM27/SUN and the second from a satellite-based system, and the results compared well. We show that measurements made by the TROPOMI combined with the HRRR modeled meteorology can be used to infer CH_4 emissions from a cluster of dairy farms. The emission estimates from this approach compare well with those derived from on-site EM27/SUN column measurements and meteorology. This suggests that this satellite-based approach can be used to monitor the time variation of CH_4 emissions over selected dairy farms. This type of continuous monitoring is not practical with on-site field measurements.

4. Field Study to Estimate Exposure to Vehicle Exhaust During Idling and Starting

4.1 Introduction

Vehicle pollutants contain carbon monoxide (CO), particulate matter (PM), nitrogen oxides (NO_x), black carbon (BC), and volatile organic compounds (VOCs) (Schulte et al., 2014; Ulfvarson et al., 1987). Several studies have indicated that exposure to these pollutants can trigger several adverse health effects such as cardiovascular morbidity, asthma, respiratory illnesses, lung function and chronic obstructive pulmonary disease (HEI, 2010; Laumbach et al., 2012). To address this issue, several field and wind tunnel studies have been conducted to estimate the impact of vehicle emissions on air quality next to roads (Finn et al., 2010; Heist et al., 2009; Thiruvenkatachari et al, 2021).

Results from these studies have been used to develop dispersion models that can provide estimates of pollutant concentration next to roads given inputs such as emission rates, traffic flows, and governing meteorological variables. Examples of such models are RLINE and CALINE (Kenty et al., 2007; Snyder et al., 2013; Yura et al., 2007), which have been used to estimate the impact of new roadway construction (e.g., highway expansion) on surrounding air quality. These models are not designed to estimate concentrations of pollutants at distances of meters from a vehicle exhaust. These distances are relevant to pollutant exposure for people located close to a vehicle when it is idling or is accelerating from a stationary position.

A limited of studies have examined dispersion of vehicle emissions at meters from a stationary vehicle. Ning et al. (2005) report results from a study that measured concentrations and size distributions of fine particles, VOCs, and NOx at distances within 5 m from an idling vehicle. The experiments were conducted under light wind conditions at the end of the day so that atmospheric turbulence played a minor role in dispersion. Turbulence induced by momentum and buoyancy of the exhaust was believed to have caused dilution of the exhaust plume. The experiments indicated that the velocity and the exit angle of the exhaust gases had a strong impact on their subsequent vertical and horizontal dispersion. The concentrations dropped off rapidly with distance from the source, reaching background levels within 3 m from the sources. These observations on the behavior of the exhaust plume were described adequately with a CFD model. McNabola et al. (2009) conducted a related study in which the dilution of exhaust concentrations was inferred by measuring concentrations of several pollutants in two identical vehicles located at 1 and 2 m from the cars in front of them. These two vehicles were driven in congested stop and go traffic. By recording the fractions of time spent in idling and moving traffic, they could estimate the fall off exhaust concentrations between 1 and 2 m during idling. They then used a CFD model to extend the measured concentrations to distances between 0 and 4 m. McNabola et al. (2009) concluded that their results were consistent with those of Ning et al. (2005), which showed a rapid decrease in exhaust concentrations to background levels within 3 m from the exhaust source. Deng et al., (2020) measured the gaseous and solid particles within exhaust plume of a typical passenger car under simulated traffic light driving pattern. They highlighted

that vehicle-induced turbulence was more and more important on pollutant dispersion with ambient wind speed increasing and pedestrians would expose 2.6-3 times higher particle number (with diameters of 28-33 nm) than atmosphere value with a 3 m distance from the vehicle.

Our study differs from previous studies in that it focuses on the near-field concentration field associated with a stationary idling vehicle located in surroundings with varying mean winds and atmospheric stabilities. The data are analyzed with a dispersion model to infer the impact of the buoyancy of the exhaust on the vertical and horizontal variation within 3 m from the source. The objective of the research described in this chapter is to collect tailpipe CO_2 concentrations relevant to such situations and use it to modify existing dispersion models for estimating exposure to vehicle related pollutants. Our experiment is designed to quantify concentrations relevant to those exposure scenarios such as 1) young children waiting on the curb to be picked up after school, 2) people waiting at curbside to cross the road at a signalized intersection, where vehicles stop and go in response to traffic lights, and 3) people waiting for pick-up services by transportation network companies, such as Lyft and Uber. We next describe the field study, and then evaluate the performance of a currently used dispersion model in describing the data from the study.

4.2 Field Study

In the field study, we collected meteorological data, and measured CO_2 concentrations at different levels and distances near the vehicle tailpipe. The CO_2 concentrations are well above background values at meters from the tailpipe. We

measured CO_2 concentrations for both idling and power cases under daytime and nighttime conditions which usually have different wind and stability conditions.

4.2.1 Site

The study was conducted in the parking lot of the College of Engineering, Center for Environmental Research and Technology (CE-CERT) of University of California, Riverside. The location was far enough from roads to avoid contamination of the CO_2 measurements by emissions from vehicles from these roads. A 2012 Toyota Corolla LE model with a 1.8-litre internal combustion engine served as the source of emissions, and the exhaust tailpipe was 26 cm above the ground.

Figure 4.1 shows the experimental set-up of the study. A polar coordinate system for measurements was used in this study. The concentrations were collected at radii of 1, 2, 3, 4 m centered around the tailpipe at angles 30, 60, 90, 120, 150°, and heights 0.3, 0.6, 1.2 m above the ground.

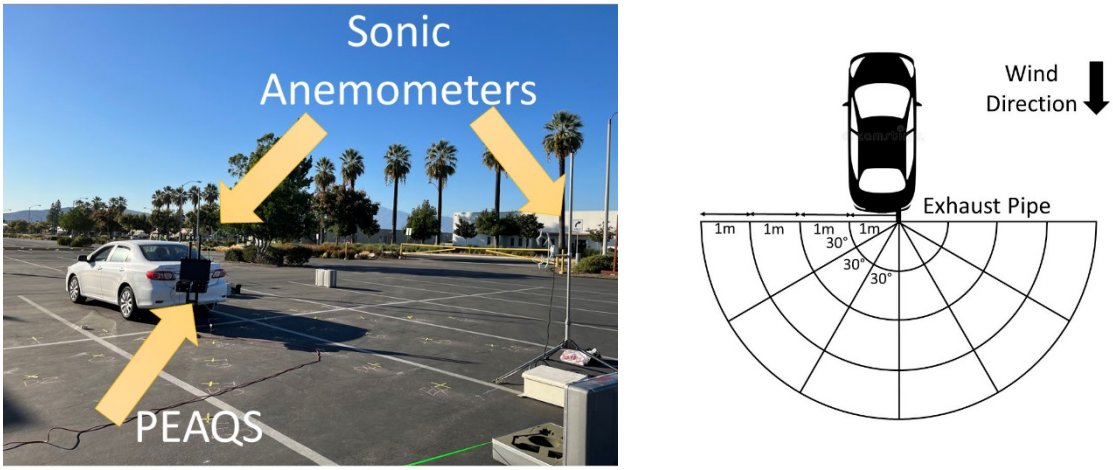

Figure 4.1. Experimental layout showing instruments used in the study. The vehicle was heading to west direction.

4.2.2 Meteorological measurements

The meteorological data were collected using two CSAT3 3-D sonic anemometers mounted at a height of 1.5 m with a frequency of 20 Hz. One sonic anemometer (Figure 4.1) was placed west (upwind) of the vehicle, and the other one was placed towards the east (downwind) of the vehicle to measure turbulence effects caused by the vehicle. The 5-minute averaged meteorological data is shown in Figure 4.2. During daytime, there was a stable west wind which blew form the front to the back of the vehicle and during nighttime, the wind direction shifted more frequently. In addition, as indicated by the red dots in the figure, the surface friction velocities u_* during nighttime were around half of the values measured during daytime.

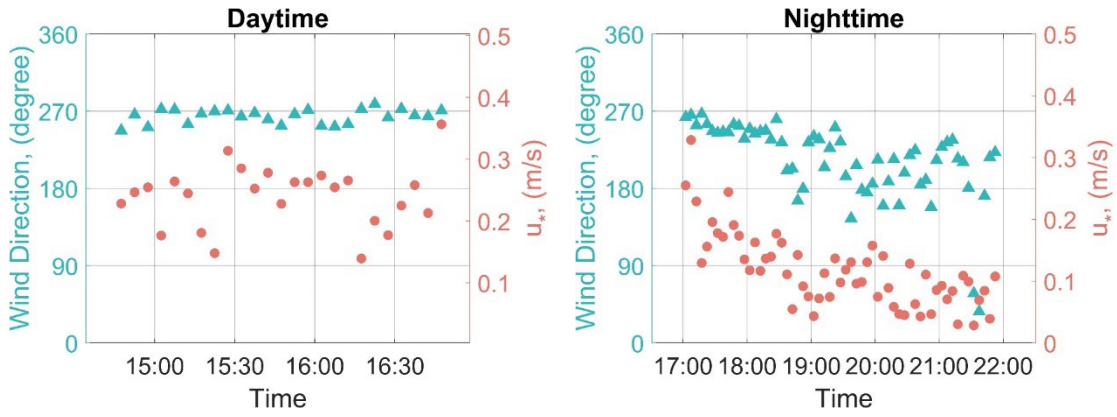

Figure 4.2. Wind direction and surface friction velocities u_* from downwind sonic anemometer averaging every 5 minutes.

4.2.3 Tailpipe temperature

The tailpipe temperature was sampled instantaneously using an infrared thermometer. Figure 4.3 shows the variation of temperature of the exhaust gases during the same two power cycles used in the field study. Based on the measurements, the

tailpipe temperature during idling was about 60 $°C$ and that during the power cycle exceeds 175 $°C$ while the ambient temperature was approximately 20 $°C$.

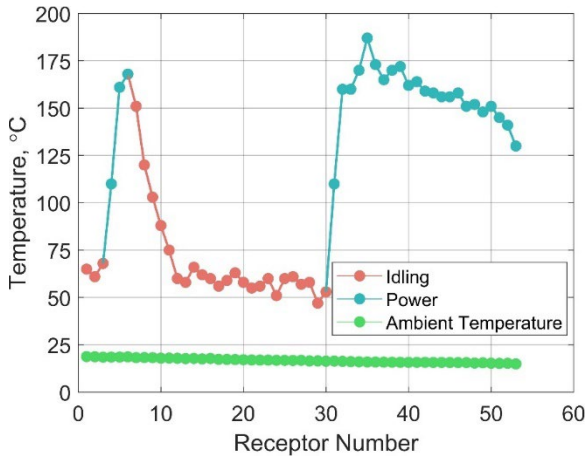

Figure 4.3. Variation of tailpipe temperature and ambient temperature under different vehicle conditions. Each receptor number represents the averaged data during one sampling period ranging from 2 to 5 minutes measurements.

4.2.4 Tracer measurements

CO_2 concentrations were measured at several distances and heights from the source using a Portable Emissions Acquisition System (PEAQS), provided by California Air Resources Board (CARB). The PEAQS. which can make real-time measurements, includes a LI-840 CO_2 gas analyzer controlled with a low-cost single-board computer Raspberry Pi. At each location, sampling was conducted over 2 to 5 minutes to capture an averaged stable plume signal. The emission rates were computed from the recorded fuel consumption rate assuming complete combustion of the fuel (US EPA, 2018). The gas pedal was positioned to produce two CO_2 emissions rates, one during idling and the other during starting.

4.3 Dispersion Modeling

The data collected in this chapter was interpreted using a point source numerical model (Venkatram and Schulte, 2018). The primary objective of this modeling exercise is to identify the processes that govern the concentrations rather than to develop a new dispersion model. The dispersion model expresses the concentration as

$$C(x,y,z) = \frac{Q}{\sqrt{2\pi}\sigma_y(x)} exp\left(-\frac{y^2}{2\sigma_y(x)^2}\right) F_z(x,z) \tag{4.1}$$

where x, y, and z are the downwind distance, crosswind distance from the source, and the height of the receptor respectively, Q is the source emission rate (mass/time), and σ_y is the horizontal plume spread. The vertical distribution function, F_z is the solution of the two-dimensional mass conservation equation. Nieuwstadt & van Ulden (1978) show that this solution provides an excellent description of the tracer measurements made during the Prairie Grass experiment (Barad, 1958). The governing equation is

$$U(z)\frac{\partial F_z}{\partial x} = \frac{\partial}{\partial z}\left(K(z)\frac{\partial F_z}{\partial z}\right) \tag{4.2}$$

where F_z denotes the crosswind-integrated vertical concentration profile, $U(z)$ is the horizontal similarity wind profile given by Businger (1973) and $K(z)$ is the eddy diffusivity. The vertical eddy diffusivity is consistent with Monin-Obukhov similarity (Businger, et al., 1971).In the numerical model, the tailpipe is represented by a point source with a vertical Gaussian distribution centered at $z_s = 0.267\ m$, with a nominal vertical spread of $\sigma_{zo} = 0.05\ m$.

The mass flux at $z = 0$ is equal to the deposition rate and is zero at large values of z. The boundary conditions are

$$K(z)\frac{\partial F_z}{\partial z} = v_d F_z \; at \; z = z_o$$

and

$$\frac{\partial F_z}{\partial z} = 0 \; at \; z = H \tag{4.3}$$

where v_d is the deposition velocity, taken to be zero for CO_2, z_o is the roughness length obtained by fitting the measured u_* with the similarity u_* iteratively (Qian et al., 2010), which is taken to be $0.023\,m$ in this study. and H is the top of the modeling domain, taken to be $20\,m$ in this study. The horizontal domain of the numerical solution is the distance between the source and the receptor at which the concentration is desired; Equation (4.2) with (4.3) are solved numerically at each receptor.

Plume rise is included in the model by the adding the average plume rise between the source and receptor to the source height. The plume rise averaged over the distance between source and receptor is given by Venkatram and Schulte (2018)

$$h_p = \frac{0.96 F_b^{\frac{1}{3}} X^{\frac{2}{3}}}{U} \tag{4.4}$$

where U is the wind speed at this average plume height, obtained from a similarity wind profile, X is the distance from source to receptor, and F_b, is the buoyancy flux given by

$$F_b = \frac{g}{T_a} v_s r_s^2 (T_s - T_a) \tag{4.5}$$

where v_s is the velocity of the exhaust gases, r_s is the inner radius of tailpipe, T_s is the exhaust gas temperature, and T_a is the ambient temperature. Equation (4.5) has to be evaluated iteratively because the wind speed at plume height is not known a priori. We do

not account for the effects of the horizontal momentum of the exhaust plume in this preliminary attempt to explain the performance of model.

4.4 Results and discussion

4.4.1 Data Interpretation

Figure 4.4 compares the model estimates normalized by the emission rates (C/Q), to corresponding observations at the receptors at different heights and distances over the meteorological conditions of the experiment. Note that the modeled C/Q, which depends only on meteorological variables, does not incorporate deposition and chemical transformation of pollutants as they are transported between source and receptor. These processes are likely to have little impact on concentrations of most vehicle-related pollutants at distances of a few meters from the tailpipe.

The scatter between the measured 2-minute and modeled concentrations is large, but the right panel shows that the model provides a good description of the distribution of measured concentrations; the concentrations are sorted from high to low before plotting. The inclusion of plume rise, whose magnitudes are shown in Figure 4.5, does not make much difference to the modeled distributions shown in Figure 4.4.

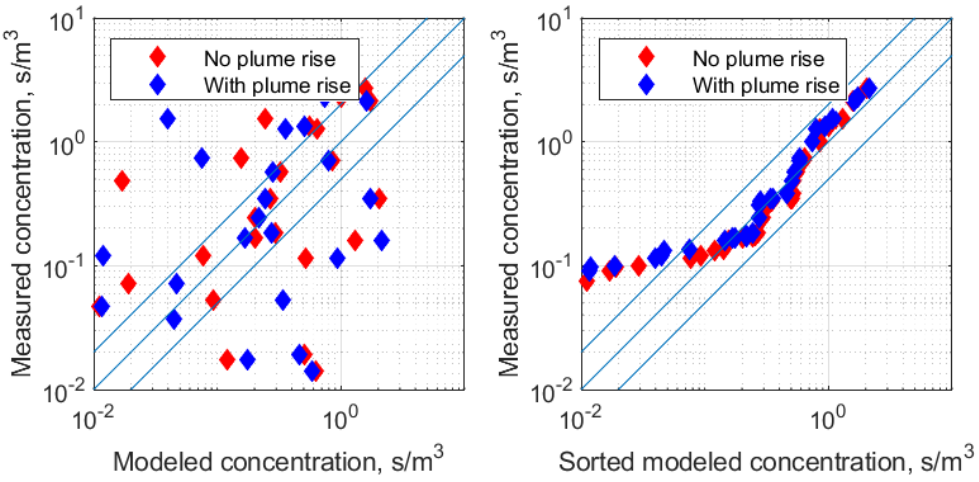

Figure 4.4. Comparison between model estimates and corresponding measured concentrations normalized by emission rates. Left panel shows concentrations paired in space and time, while the right panel compares distributions of the two sets of concentrations.

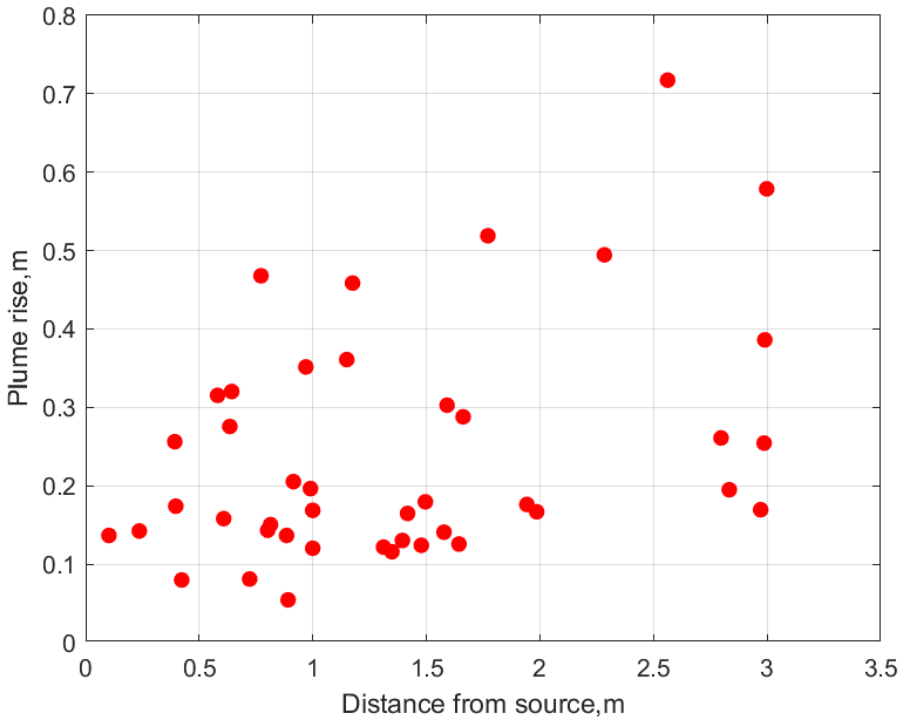

Figure 4.5. Plume rise versus distance from source.

We postulate that the arc-averaged concentration is an approximation to a time average that is longer than the averaging time used to compute the concentrations shown in Figure 4.4. Figure 4.6 compares the arc averaged concentrations measurements to the corresponding modeled values. Here, we see that most of the model estimates with plume rise are within a factor of two of the measurement arc-averaged values. The inclusion of plume rise appears to reduce the scatter at the low values of C/Q.

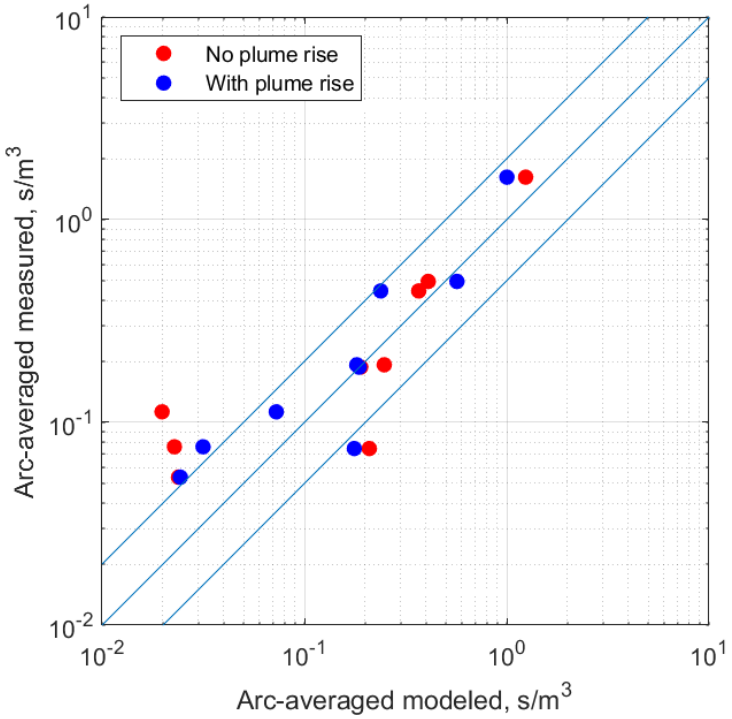

Figure 4.6. Arc-averaged measurements compared with model estimates with and without plume rise. The parallel lines around the one-to-one lines correspond to factor-of-two limits.

Figure 4.7 shows that the performance of the model in describing the downwind variation of concentrations. Both versions of the model are within a factor of two of the measurements at heights of 0.3m and 0.6m. However, at a height of 1.2m, plume rise improves the performance of the model relative to the version without plume rise. The

estimates with plume rise follow the decreasing trend with distance seen in the measurements, while the model estimates without plume rise do not.

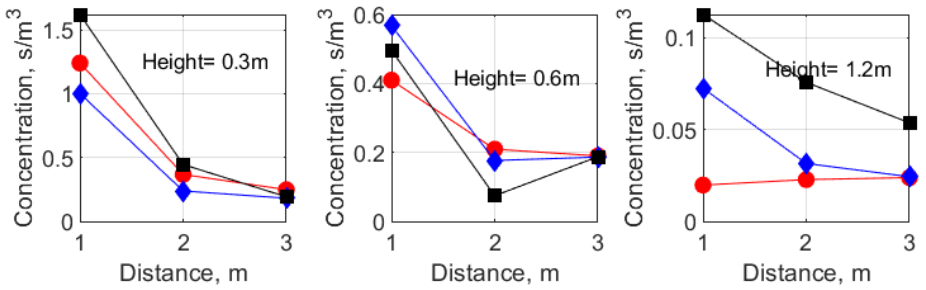

Figure 4.7. Comparison of modeled downwind variation with arc-averaged measurements. Black squares: Measurements. Blue diamonds: Model with plume rise. Red circles: Model without plume rise.

Figure 4.8 compares the measured vertical variation of concentrations with the model values with and without plume rise. Here again we see the improvement in model performance by including plume rise. This is most evident at the distance of 3m where the measurements show mixing below the height of 0.6m; the model with plume rise describes this feature well while the model without plume rise shows a concentration that decreases rapidly with height.

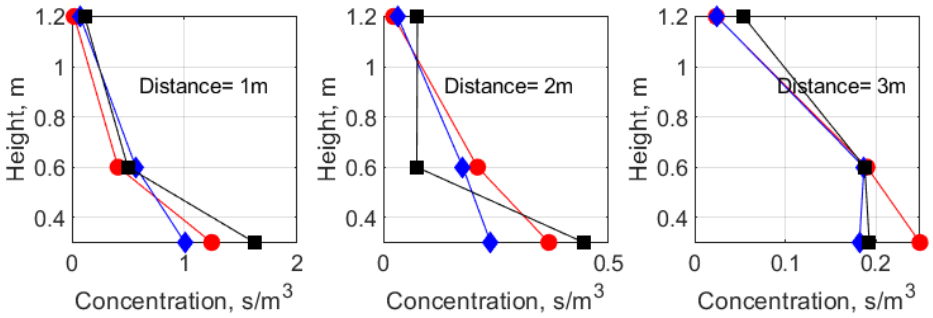

Figure 4.8. Comparison of modeled vertical variation of concentrations with arc-averaged measurements. Black squares: Measurements. Blue diamonds: Model with plume rise. Red circles: Model without plume rise.

4.4.2 Near Source Exposure to Emissions

The measured emission normalized concentrations C/Q can be used to estimate exposure to various of pollutants such as nitrogen oxides (NO_x) and particulate matter with aerodynamic diameter: less than 2.5 micrometer ($PM_{2.5}$) close to the vehicle. The measured values of C/Q are multiplied by the vehicle NO_x and $PM_{2.5}$ fuel-based emission factors (grams of pollutant per kg fuel burned) given by Park et al. (2011) and on-board diagnostics (OBD) measured fuel rates whose values are shown in Table 4.1. The NO_x and $PM_{2.5}$ emission factors are slightly higher during idling than during the power cycle presumably because of incomplete combustion not operating at peak temperature (Shancita et al., 2014). The estimated NO_x and $PM_{2.5}$ averaged concentrations using the CO_2 dispersion pattern at several distances and heights are shown in Table 4.2.

Depending on how rapidly NO_x is converted to NO_2, we see that most NO_2 concentrations within the distance of 3 meters are likely to exceed the EPA NO_2 1-hour standard of 100 ppb for both idling and power cycles. $PM_{2.5}$ concentrations are below the EPA 24-hour standard of 35 $\mu g/m^3$. These results suggest that exposure to high NO_2 concentrations could be one of the primary health concerns for people waiting a few meters from an idling vehicle over periods of minutes.

Table 4.1. Averaged emission factors for light duty gasoline vehicles under idling and power conditions

	Fuel Rate (gal/hr)	NO_x Emission Factor (g/kg)	$PM_{2.5}$ Emission Factor (g/kg)	NO_x Emission Rate (g/s)	$PM_{2.5}$ Emission Rate (g/s)
Idling	0.154	7.90	0.20	9.795×10^{-4}	2.480×10^{-5}
Power	0.596	6.50	0.15	3.017×10^{-3}	6.963×10^{-5}

Table 4.2. Estimated NO_x and $PM_{2.5}$ arc averaged concentrations

Height (m) / Distance (m)		NO_x Concentration (ppb)			$PM_{2.5}$ Concentration ($\mu g/m^3$)		
		0.3	0.6	1.2	0.3	0.6	1.2
Idling	1	872	91	38	41.6	4.3	1.8
	2	354	73	33	16.9	3.5	1.6
	3	182	141	37	8.7	6.8	1.8
Power	1	2406	1265	236	104.7	55.1	10.3
	2	110	128	134	4.8	5.6	5.8
	3	41	320	88	1.8	13.9	3.8

4.5 Conclusions

This chapter describes a field study designed to collect concentrations of tailpipe CO_2 at distances of meters from idling vehicles exposed to varying wind speeds and stabilities. As the first step in interpreting the data, we examined the performance of a currently available point source dispersion model in describing the measured concentrations; this model is not designed for the spatial scales of the situation under study and does not account for the effects of the momentum of the exhaust plume.

The comparison of measurements with model estimates suggests that currently available dispersion models provide an adequate description of the measurements if plume rise, associated with the exhaust plume, is accounted for. Wake turbulence might not be important when the vehicle is stationary; Chang et al., (2012) show that turbulence in the wake of a moving vehicle has a major impact on the dilution of the exhaust plume.

To illustrate the application of a dispersion model designed for near-tailpipe exposure, we have used the results of the field study to estimate the risks of exposure to potential pollutants such as NO_2 and $PM_{2.5}$ during the situations described earlier. The

results show that people waiting next to idling or slowly moving cars are likely to be exposed to high levels of NO_2.

It is worth repeating that the field study described in this chapter is relevant to estimating exposure to vehicle emissions when customers are waiting for pick-up services by transportation network companies. Other similar situations to this near-road exposure case are: 1) young children waiting on the curb to be picked up after school; and 2) people waiting at curbside to cross the road at a signalized intersection, where vehicles stop and go in response to traffic lights.

5. An Assessment of Paved Road Dust Emissions Modeling

5.1 Introduction

Particulate matter with diameters less than 10 μm (PM_{10}) is one of the six criteria air pollutants established by U.S. EPA. It consists of solid particles and liquid droplets suspended in the air (US EPA, 2023b). Numerous studies have demonstrated that exposure to particulate matter (PM) has adverse effects on respiratory and cardiovascular systems of humans (Jose and Srimuruganandam, 2020; Khan and Strand, 2018; US EPA, 2023c). The mobile sources sector, including road traffic, is recognized as one of the primary contributors to PM emissions (Casotti Rienda and Alves, 2021; Dallmann and Harley, 2010). The 2020 National Emissions Inventory (NEI) developed by the U.S. EPA indicates that the transportation sector is responsible for about 10% of PM emissions in the United States (US EPA, 2023d).

PM emissions from roadways can be classified into two primary categories: exhaust emissions and non-exhaust emissions (NEE). Many studies have been conducted to quantify and analyze vehicle exhaust emissions, and this research is crucial for understanding the environmental and health effects exposure to engine exhaust (Bisig et al., 2018; Ding et al., 2022; Ljungman et al., 2019; Steiner et al., 2016; Weitekamp et al., 2020; Wu et al., 2022). Non-exhaust emissions, often referred to as resuspended dust or road dust (RD), encompass a range of sources such as the mechanical wear of tires, brakes, vehicle components, road materials, and the re-suspension of particles into the atmosphere due to the turbulence processes (Casotti Rienda and Alves, 2021). Recent

studies have shown that road dust plays a significant role in contributing to at least 50% of the total PM concentrations currently (Amato et al., 2014; Denier van der Gon et al., 2018), and it is projected to increase to 67% in 2035 (S. Reid et al., 2016) or even reach 90% in 2030 (OECD, 2020). The upward trend in road dust's dominance in PM concentrations emphasizes the importance of accurately quantifying road dust as well as uncertainties.

PM_{10}, consisting of all particles with an aerodynamic diameter smaller than 10 μm, is categorized as inhalable particulate matter. $PM_{10\text{-}2.5}$, composed of particles with an aerodynamic diameter between 2.5 and 10 μm, is termed coarse particulate matter. $PM_{2.5}$, which comprises particles with an aerodynamic diameter less than 2.5 μm, is classified as fine particulate matter. Several studies tried to distinguish road dust contribution to $PM_{2.5}$ and $PM_{10\text{-}2.5}$ respectively. Matthaios et al. (2022) deployed a mobile platform investigation along with the positive matrix factorization (PMF) method to identify non-exhaust sources responsible for 65.6% of coarse particulate matter (PM) and 29.1% of fine PM respectively. Harrison et al. (2012) integrated size distribution and tracer elements to differentiate brake dust, tire dust, and resuspension, within the 0.9−11.5 μm aerodynamic diameter range. These sources collectively constituted 104.1% of coarse particle mass in traffic. Based on these evidences, our study assumes that road dust predominantly contributes to the $PM_{10\text{-}2.5}$ size fraction in our data analysis and modeling.

The currently used regulatory model to estimate the road dust is described in the "Compilation of Air Pollutant Emissions Factors" (AP-42). U.S. Environmental Protection Agency (EPA) initially published in 1968. The model is routinely updated the

new versions (US EPA, 2011a). The current version of the AP-42 model is a semi-empirical equation based on two inputs: road surface silt loading *sL*, which refers to the fraction of surface dust with aerodynamic diameter below 75 μm (US EPA, 1995), and averaged weight of vehicle (US EPA, 2011b). In recent years, numerous studies have employed the AP-42 model to assess silt loading and emission factors (Bogacki et al., 2018; Bukowiecki et al., 2010; Chen et al., 2019; Fitz et al., 2020; Kumar and Elumalai, 2018; Thorpe et al., 2007). For instance, Alves et al. (2018) applied the AP-42 method in Road tunnel, Braga, Portugal and reported the silt loading 0.059 [$g\ m^{-2}$] and PM_{10} emission factor 33 [$mg\ km^{-1}\ veh^{-1}$]. Amato et al. (2017) presented the AP-42 silt loading estimates ranging from 0.006 - 0.066 and [$g\ m^{-2}$] and PM_{10} emission factor 13–32 [$mg\ km^{-1}\ veh^{-1}$] in Milan, Italy. Although the AP-42 model is utilized worldwide, Venkatram et al. (1999) criticized the AP-42 model for yielding unreliable emission results due to its lack of a mechanistic foundation. Furthermore, the official procedures recommended by AP-42 for directly sampling silt loading on paved roads require manual and stationary collection of road surface materials using a vacuum cleaner (US EPA, 1993). Han et al. (2011) highlighted limitations in replicating real-world road dust resuspension through local sampling using vacuum sweeping and resuspension chambers. Zhang et al. (2017) and Fitz et al. (2020) expressed concerns about the impracticality and safety issues associated with applying these procedures on some active roads.

This study is motivated by the need to address the limitations of the formulation of the model as well as difficulty in specifying model inputs. The main objectives of this study are to 1) design a mobile dust collection system that adheres to AP-42

requirements, facilitating portable and reliable mobile sampling of silt loading on various roadways 2) develop and assess a new model that incorporates a physical structure for estimating emission factors of paved road dust ($PM_{10-2.5}$) on California freeways with varying traffic volumes.

5.2 Method and Methodology

5.2.1 Field Studies

This chapter provides a comprehensive overview of the methodologies employed and the measurement results from the field campaign conducted on two freeways and two city roads in Riverside, California. The on-road field studies were conducted during the period from June to July 2023, and the studied roads were chosen at a portion of I-91 freeway, Chicago Avenue, Iowa Avenue, and I-215 freeway in Riverside California as shown in Figure 5.1. The studied roads are approximately 0.7-1.3 km long with 230° (I-91 freeway) and 180° (other roads) orientation under geographic wind coordinate (North is 0° , and East is 90°). The total widths of the studied roads are approximate 20-32 m listed in Table 2.

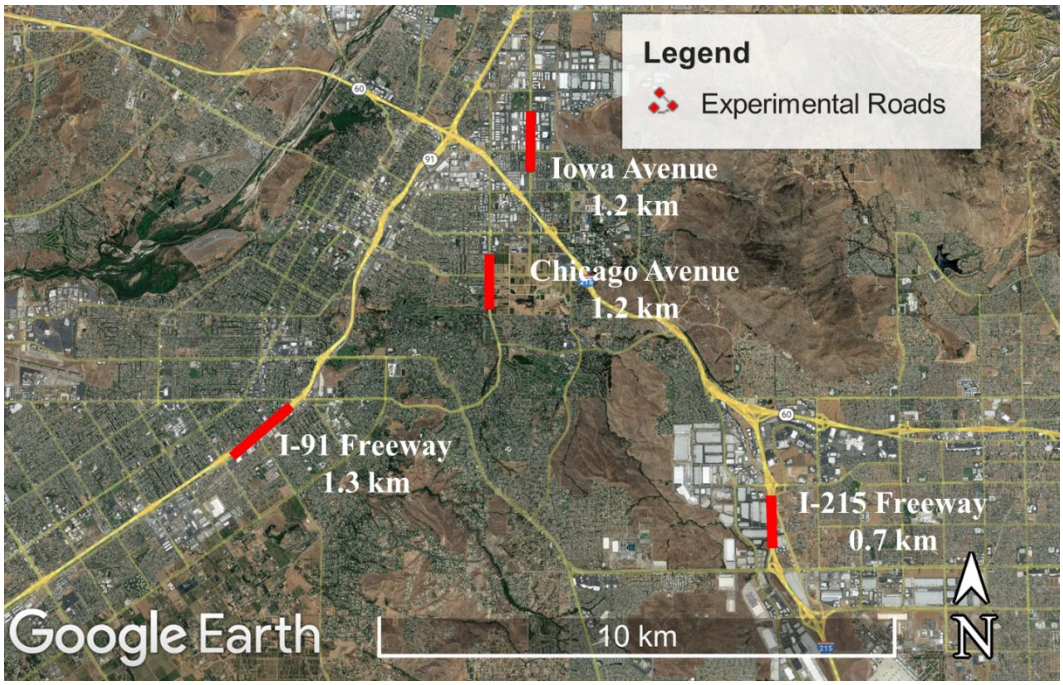

Figure 5.1. Top view of sampled roads in Riverside

In this study, our mobile laboratory was equipped with two PurpleAir PM monitors and one Picarro G2401 CO/CO2 gas concentration analyzer, all of which were meticulously calibrated using standard cylinder CO/CO2 gas. The inlets for both the gas and PurpleAir PM monitors were mounted on the side door of the vehicle at an elevation of approximately 1.2 meters. During our mobile data collection measurements, we conducted multiple loops along both freeway and city roads. This enabled us to obtain real-time data on CO_2 gas concentrations, PM concentrations, and collect surface road dust samples.

To quantify re-suspended dust emissions, we employed the downwind-upwind difference method, with the experimental scenarios depicted in Figure 5.2. Scenario 1 involved measurements taken while the vehicle was in motion on the downwind side of the road. In Scenario 2, we conducted measurements while the vehicle was parked

stationary on the downwind side of the road. This stationary setup allowed us to gather crucial turbulence parameters, including the standard deviation of the vertical velocity σ_w and surface heat flux Q_o, which will be discussed in detail in section 5.2.4. Scenario 3 includes stationary measurements taken upwind, aiding in the determination of background concentrations and relevant meteorological variables such as wind direction and speed. The road contribution to the air species of interest in this study is expressed as follows

$$C_{road} = C_1 - C_3 \tag{5.1}$$

where C_1 is the downwind on-road concentration averaged while the vehicle is on the road, and C_3 is the upwind stationary concentration which is assumed to be the background concentration. The background sampling time was 5 minutes for all the studied roads. The evaluation of how the quality of air monitoring is influenced by factors such as the vehicle's body and movement-induced turbulence is discussed in an independent study conducted on the I-215 freeway. Further insights into this assessment can be found in section 5.4.

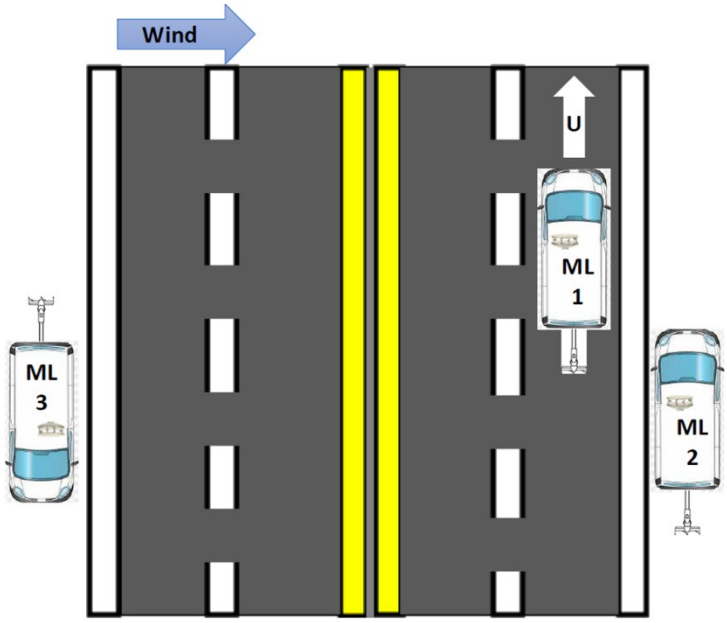

Figure 5.2. Experimental scenarios for on-road measurements by the mobile lab attached air quality monitors and the portable dust collection system

5.2.2 PM Instruments Calibration

The PurpleAir monitor comprises a pair of laser scattering particle sensors (Plantower PMS5003 sensors), along with a Bosch BME280 sensor for measuring pressure, temperature, and humidity. It also features a WiFi-enabled processor, enabling real-time data uploading to the cloud for immediate utilization. The PurpleAir SD card recording offers a minimum time resolution of approximately 2 minutes. However, the PurpleAir terminal provides the capability to retrieve raw data at a finer granularity of 1 second, as demonstrated in Table 5.1.

For the internal calibration, the current model called PurpleAir-II monitors were set for running side-by-side in the UCR Agricultural Operations (Ag-Ops). One PurpleAir monitor was set as a reference monitor, and the other monitors are corrected

based on its raw measurements. In this study, we applied a multiple regression method for PurpleAir correction using the equation discussed by Barkjohn et al. (2021)

$$PA_{cor} = s_1 \times PA_{raw} + s_2 \times T + s_3 \times RH + i \tag{5.2}$$

where PA_{cor} is defined as the corrected PurpleAir measurements, PA_{raw} represents the raw PurpleAir measurements, T is the PurpleAir recorded air temperature in degrees Fahrenheit [°F], RH is the PurpleAir measured relative humidity [%], s_1, s_2, and s_3 are determined using the non-negative least-square method, which minimizes the square of residual i between the reference measurements and raw measurements.

For the external calibration, the historical routine measurements taken from the side-by-side BAM 1020 and PurpleAir monitors, which are maintained by the South Coast Air Quality Management District (SCAQMD) at the Rubidoux, Riverside location as shown in Figure 5.3, were utilized for the external calibration analysis. Table 5.1 compares the PM monitors used for the external calibration.

Figure 5.3. South Coast AQMD PM monitors setup at Rubidoux site

Table 5.1. Summary of the BAM 1020 and PuepleAir monitors

Instrument Model	Pollutants	Minimum Time Resolution	Air Monitoring Methods	Power [W]	Weight [kg]	Cost (USD)
PurpleAir II SD	$PM_{2.5}$; PM_{10}	~2 min (1 sec available via PurpleAir Utility terminal)	Optical and Algorithm	1	0.4	289
Met One BAM 1020	$PM_{2.5}$; PM_{10}	1 hour	FEM ($PM_{2.5}$; PM_{10})	400	38	37200

5.2.3 Meteorological Inputs

A Campbell Scientific CSAT3 3D 20 Hz sonic anemometer was used to calibrate a 2D micrometeorological model before the formal field studies (Thiruvenkatachari et al., 2023). The raw sonic anemometer data contains three mutually perpendicular wind vectors (u, v, w) and temperature (T). The sonic anemometer needs to be leveled to ensure that vertical wind vector w is perpendicular to the ground and the sonic arm faced true north using a compass and adjusted by the real-location magnetic declination. The sonic anemometer was mounted at 3 m and 5 m on a tower. The idling mobile lab was

parked next to the 3D sonic anemometer for 8 hours each day to estimate the performance of the mobile platform observed meteorology as shown in Figure 5.4. The raw data from the sonic anemometer was then retrieved and processed to obtain 5-minute averaged micrometeorological parameters.

Figure 5.4. Experimental set up of side-by-side comparisons between 3-D sonic anemometer and mobile platform meteorological monitors

5.2.4 Dust Collection System

In this study, a mobile dust collection system was designed for a cargo van, as illustrated in Figure 5.5. A 3.5 kW generator powered a VacuMaid GV30 central vacuum cleaner, which boasts 740 max air watts. The vacuum cleaner employs a High Efficiency Particulate Air (HEPA) filter bag for dust collection.

Throughout the on-road measurement phase, a phone GPS tracked the vehicle's location, information that was used to compute the distance traveled by the van. . The van was driven at speeds ranging from ranging from 25-30 mph in the rightmost lane,

ensuring the brush was fully in contact with the ground for stable dust collection. A trailing vehicle observed the brush and provided additional safety. Dust samples were obtained from both freeway and local street, with the HEPA bags subsequently sent to the lab for weighing. The log time that records the dust sampling period is shown in Table 5.2.

The first step of the in-lab standard procedure is to transfer the bag's contents to a plastic zip lock bag. The collected dust was then sieved through 0.315 mm, 0.15 mm, 0.075 mm, and 0.0385 mm meshes in sequence. Since some dust inevitably remains in the original HEPA bag and ziplock bag, the leftover dust mass is proportionally allocated to the sieved dust with diameters below 0.15 mm for correction. Finally, the dust per unit area with an aerodynamic diameter below 0.075 mm was considered as the measured silt loading (sL) in this study.

Figure 5.5. Mobile dust sampling system

Table 5.2. Summary of dust sampled on different roads

Road Location	Sampling Duration [minute]	Road Width [m]	Mean Silt Loading [g/m^2]	Mean Speed [mph]	Mean Vehicle Weight [tons]	Mean Traffic Flow [veh/hr]
I-91 Freeway	~ 4	30	0.009 ± 0.008	59 ± 4	2.31	8833
Chicago Avenue	~ 5	20	0.012 ± 0.005	35	4.53	1850
Iowa Avenue	~ 5	20	0.017 ± 0.006	35	5.18	2008
I-215 Freeway	~ 4	32	0.006 ± 0.003	47 ± 7	2.53	5733

The traffic data including the traffic flow and vehicle speed for the freeways was available through the Caltrans Performance Measurement System (PeMS). This information is collected in real-time from Loop Detector Stations (LDS) embedded within the road surface, providing the traffic info for all lanes, updated every 5 minutes at

minimum (Caltrans, 2020). Meanwhile, the traffic data for the city roads was obtained through a GoPro camera, mounted roadside, recorded the traffic. The recorded video was then manually analyzed to count the number of vehicles and classify them based on different vehicle types during the time window when the mobile lab took on-road measurements. The averaged vehicle speed on city roads was assumed to be 35 [mph] which the upper limit for these roads.

5.3 Road Dust Modeling

5.3.1 AP-42 Model

The document "Compilation of Air Pollutant Emissions Factors" (AP-42) was published by U.S. Environmental Protection Agency (EPA) since 1968. It isroutinely updated by EPA (US EPA, 2011a), and current version of the emission factor reads

$$EF = k \times (sL)^{0.91} \times (W)^{1.02} \tag{5.3}$$

where EF is the particulate matter emission factor in unit of $[g/(veh \cdot km)]$, sL is the road surface silt loading in $[m/g^2]$, k is the particle size multiplier taken to be 0.15 and 0.62 for $PM_{2.5}$ and PM_{10} respectively, W is average weight of vehicles traveling on the road expressed in tons. In this study, the average weight of light-duty vehicles (LDV) which include sedans, SUVs, pickup trucks and vans is taken to be 1.95 tons suggested by US EPA (2022). The average weight heavy-duty vehicles (HDV) is taken to be 16.5 tons, which is the threshold value of the medium heavy-duty (MHD) vehicles and heavy heavy-duty (HHD) vehicles provided by US EPA (2016). Table 2 presents the weighted average weights determined from the traffic flow of LDV as well as HDV and their corresponding hypothesized weights. In addition, California statewide default value of

the average weight of vehicles, which is 2.4 tons, is treated in the results as a reference value (CARB, 2016b). Table 5.3 presents the default silt loading values, which will serve as a reference in cases where on-site measurements are unavailable. These values are evaluated and discussed in the chapter 5.4.

Table 5.3. AP-42 default silt loading values

Silt Loading Categories	ADT Category [veh/day]			
	<500	500 - 5000	5000 - 10000	>10000
Default baseline [g/m^2]	0.6	0.2	0.06	0.015 for freeways; 0.03 for other roads
Winter baseline during months with frozen precipitation [g/m^2]	2.4	0.6	0.12	0.015 for freeways; 0.03 for other roads

5.3.2 Line Source Model

Highways and city roads are represented as a set of line sources, and the impact of each line source to the concentration at the receptor location is given by the expression (Venkatram and Horst, 2006)

$$C_p(x_r, y_r, z_r) = \frac{Q}{cos(\theta)}[erf(t_e) - erf(t_b)]F_z(x_d, z_r) \tag{5.4}$$

$$t_e = \frac{y_e - y_r}{\sqrt{2}\,\sigma_y(x_r - x_e)} \tag{5.5}$$

$$t_b = \frac{y_b - y_r}{\sqrt{2}\,\sigma_y(x_r - x_b)}$$

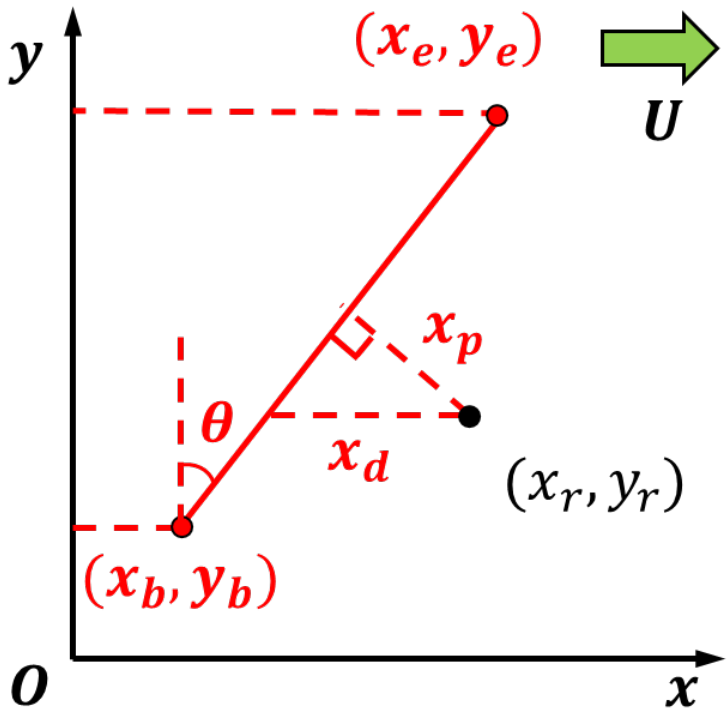

Figure 5.6. Line source co-ordinate system used to determine the concentration at the receptor location

where C_p is the plume state concentration in unit of $[g/m^3]$, Q is the emission rate in units of $[g/(m \cdot s)]$, the parameters related to coordinates are established within a rotated coordinate system as shown in Figure 5.6, where the x-axis aligns with the direction of the wind, (x_r, y_r), (x_b, y_b), and (x_e, y_e) are the co-ordinates of the receptor, the beginning, and ending points of the source line, θ is the angle between the source line and the y-axis, x_d is the downwind distance between the receptor and the source line, $\sigma_y(x_r - x_e)$ and $\sigma_y(x_r - x_b)$ are the horizontal plume spread in [m] at the distances of $(x_r - x_e)$ and $(x_r - x_b)$ provided by Venkatram et al. (2013), and F_z is the vertical concentration profile which can be given by

$$F_z(x_d, z_r) = \frac{1}{\sqrt{2\pi} U_e \sigma_z} \left[exp\left(-\frac{(z_r - z_s)^2}{2\sigma_z^2} \right) + exp\left(-\frac{(z_r + z_s)^2}{2\sigma_z^2} \right) \right] \quad (5.6)$$

where z_r and z_s are the receptor height and source height taken to be 1.2 m and 0.3 m respectively in this study, U_e is the effective wind speed in unit of $[m/s]$ given by $U_e = (2\sigma_v^2 + U^2)^{0.5}$ where σ_v is the standard deviation of crosswind velocity, and σ_z is the vertical plume spread in [m] obtained from an semi-empirical formulation given by Venkatram et al. (2013)

$$\sigma_z = f(x, u_*, L, U(\bar{z})) \tag{5.7}$$

where u_* is the surface friction velocity , L is the Monin–Obukhov length, $U(\bar{z})$ is the Monin–Obukhov similarity theory predicted wind speed at the mean plume height $\bar{z}$ by solving the Equation (5.7) and (5.8) iteratively (Businger et al., 1971; Venkatram et al., 2013a)

$$\bar{z} = \sigma_z \sqrt{\frac{2}{\pi}} exp\left[-\frac{1}{2}\left(\frac{z_s}{\sigma_z}\right)^2\right] + z_s erf\left(\frac{z_s}{\sqrt{2}\,\sigma_z}\right) \tag{5.8}$$

Under low wind speed conditions, the meandering wind is assumed to spread radially in all horizontal directions and the meandering components of the concentration can be written as

$$C_m(x_r, y_r) = \sqrt{\frac{2}{\pi}} \frac{Q}{U_e \sigma_z(x_p)} \frac{\theta_s}{2\pi} \tag{5.9}$$

where $\sigma_z(x_p)$ is the vertical plume spread at the perpendicular distance of the receptor from the line source, and θ_s represents the angle between the lines joining (x_b, y_b), (x_r, y_r), and (x_e, y_e)

The aggregate concentration, following the incorporation of the meandering algorithm, is computed as a weighted mean of both the plume component from Equation (5.4) and the meandering component given by Equation (5.9)

$$C = C_p(1 - f_r) + C_m f_r$$

$$f_r = \frac{2\sigma_v^2}{U_e^2} \tag{5.10}$$

where f_r is the weight for the random meandering component ensuring that the weight for meandering component to be unity when effective wind speed approaches zero.

5.3.3 Simple Road Dispersion Model

The dispersion model expression for an infinitely long road is used for estimating the emission factors (Thiruvenkatachari et al., 2022)

$$C = \sqrt{\frac{2}{\pi}} \frac{Q}{W\sigma_w} ln\left(1 + \frac{W\sigma_w}{h_o U cos\theta}\right) \tag{5.11}$$

where C is the particulate matter concentration in unit of $[g/m^3]$, Q is the emission rate in unit of $[g/(m \cdot s)]$, W is the road width in $[m]$, σ_w is the standard deviation of vertical wind speed in unit of $[m/s]$ predicted from the mobile platform model, U is the background wind speed in unit of $[m/s]$ observed from the mobile platform, and h_o is the initial mixing height which is given as 2 m in this study.

The emission rate Q can be further converted to the emission factor with the observed traffic flow rate

$$EF = \frac{Q}{Tr} \tag{5.12}$$

where EF is the emission factor representing the particulate matter mass per vehicle per unit length traveled, Tr is the traffic flow rate in [veh/hr].

5.3.4 Carbon Mass Balance Method

The emission rates can also be determined based on the following equation (Jalali Farahani et al., 2022)

$$Q = \frac{[PM]_{dw} - [PM]_{bg}}{[CO_2]_{dw} - [CO_2]_{bg}} \times w \times 10^6 \times \rho \times U \tag{5.13}$$

where $[PM]$ and $[CO_2]$ are the particulate matter and carbon dioxide concentrations, $[]_{dw}$ and $[]_{bg}$ are air species measured at the downwind road and upwind background locations respectively, w is the carbon weight fraction of the fuel, which was considered 0.85 and 0.87 for diesel fuels and gasoline fuels respectively, ρ is the density of the fuel, reported 0.74 kg/L and 0.84 kg/L for gasoline and diesel respectively, U is the average fuel consumption of the vehicles which are considered for diesel and gasoline were 0.107 L/km and 0.424 L/km respectively, and they are weighted averaged based on truck flow and passenger flow. The calculated emission rates can apply Equation (5.13) to obtain the emission factors as well.

5.4 Results and Discussion

5.4.1 PM Monitors Calibration

To evaluate the influence of vehicle body and turbulence caused by movement, we conducted a comparative analysis using data collected simultaneously from both vehicular and stationary PurpleAir monitors. Figure 5.7 illustrates scatter plots depicting

the emission factors obtained from these distinct monitor types. Notably, both the R^2 values for PM_{10} and $PM_{2.5}$ emission factors measured by vehicular and stationary PurpleAir units stand at 0.93 and 0.87 respectively.

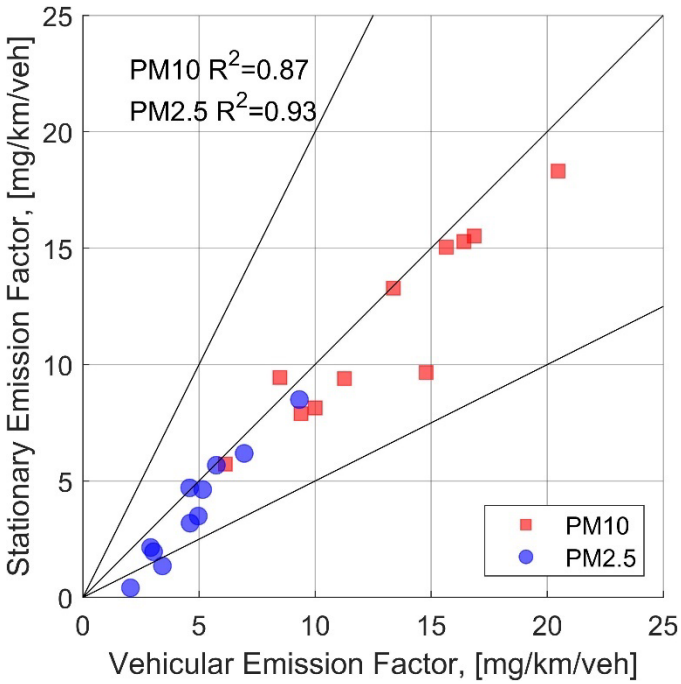

Figure 5.7. Comparisons of the emission factors estimated from vehicular calibrated PurpleAir monitors and stationary mounted PurpleAir monitors near the I-215 freeway.

To validate the low-cost PurpleAir monitors, we compare the hourly PM_{10} and $PM_{2.5}$ co-located FEM BAM 1020 monitor concentration measurements from SCAQMD routinely observing site in Rubidoux which is closed to 60 freeway for one month period starting from April 12th to April 30th, 2022. The raw correlation and statistical results are shown in Figure 5.8 and Table 5.3. m_g is a measure of the bias; m_g greater (less) than unity indicates over measurement (under measurement). The percentage of x-axis values within a factor of 2 of the y-axis values is denoted as Fact2. We can see that for raw $PM_{2.5}$ measurements comparison, the R^2 can reach as high as 0.73 and 87% of datapoints

lie within the factor of 2. However for raw PM_{10} measurements, the R^2 is 0.55 and Fact2 is only 23%.

The results in Table 5.3 show that after applying the correction method, both m_g and Fact2 improve for PM_{10} comparison and the previous under measurements disappear.

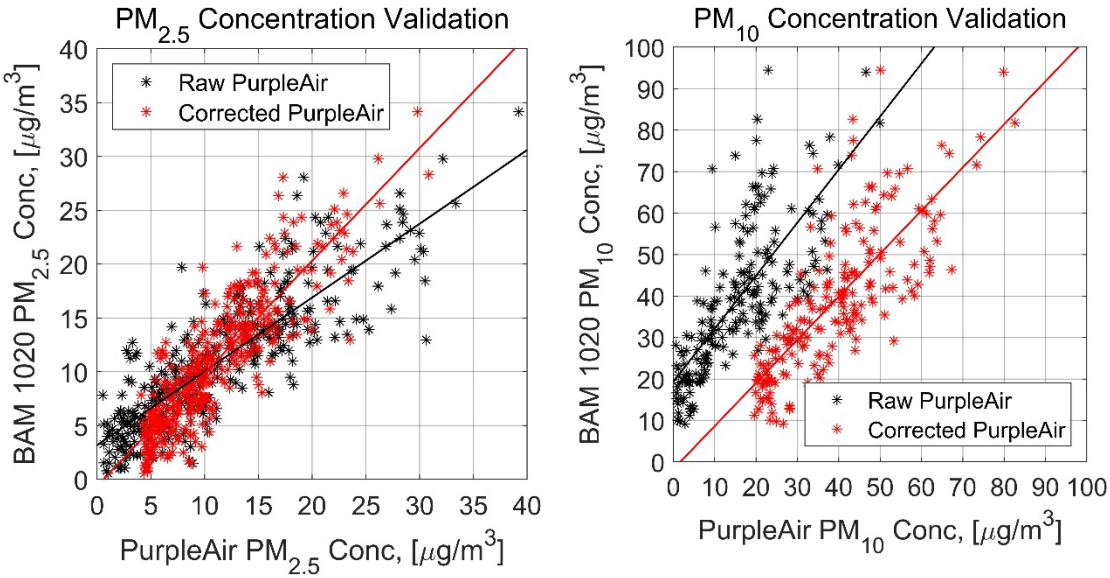

(a) (b)

Figure 5.8. Comparisons of PM_{10} and $PM_{2.5}$ measurements between PurpleAir and FEM BAM 1020 instrument

Table. 3 Statistical results for raw and corrected PurpleAir – BAM 1020 comparisons

		Slope	Intercept	s_1	s_2	R^2	m_g	Fact2
$PM_{2.5}$	Raw	0.7	3.2	1	0	0.73	0.95	87%
	Corrected	1.1	-0.6	0.67	0.05	0.76	1.1	92%
PM_{10}	Raw	1.3	19.4	1	0	0.55	0.32	23%
	Corrected	1.0	-1.7	1.32	0.25	0.6	1.06	96%

5.4.2 Mobile Platform Meteorology Performance

Because the 3D sonic anemometer needs careful leveling, it cannot be deployed on the mobile platform used to sample silt loading on roads. So we developed a method to measure micrometeorological parameters that was robust enough to be mounted on a mobile platform. The method, based on 2D wind information and high frequency

temperature data is described in Thiruvenkatachari et al.(2023). Figure 5.9 the top left and top right panels compare of the meteorological measurements from the 3D sonic anemometer with those derived from measurements made on the mobile platform. The bottom left and bottom right show the performance of the mobile platform model in estimating the standard deviation of vertical speed σ_w and kinematic heat flux Q_o. The comparisons indicate that the meteorological parameters derived from the mobile platform are more than adequate as inputs to the dispersion model used to derive emission factors.

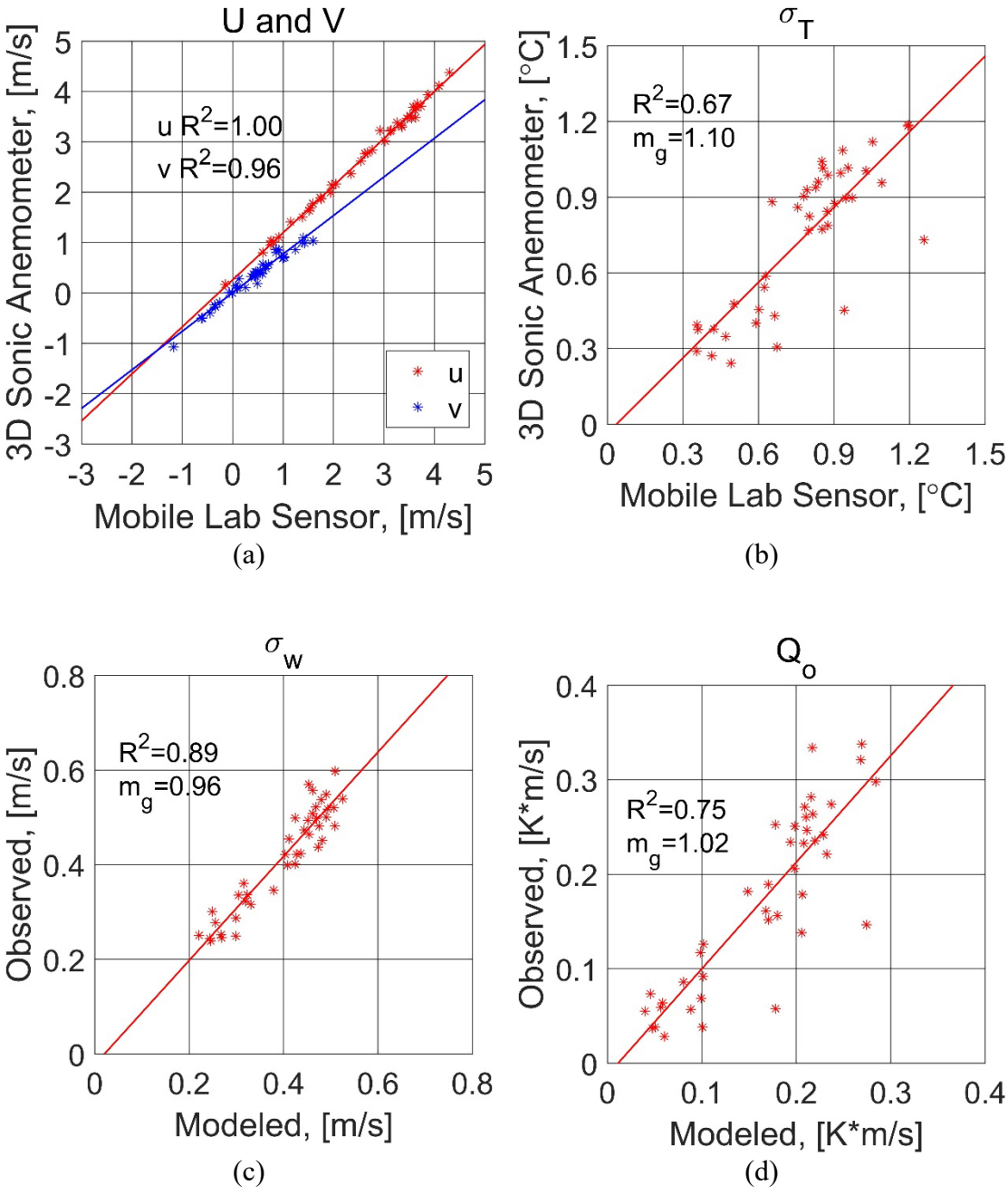

Figure 5.9. Measurement comparisons and model performance of mobile platform meteorology

5.4.3 Estimated Emission Factors

For the silt loading results, the standard deviation 1 σ uncertainties were determined by sampling the surface road dust 3 times continuously with a relatively

constant traffic flow and the same mobile platform setup before the formal study. It turned out that our mobile system sampled silt loading results had an averaged standard deviation 6.5% of the measurements. Figure 5.10 shows the relationship between emission factors inferred from the using PurpleAir measurements (N=66) versus different parameters: silt loading, vehicle weight, vehicle speed, and traffic flow per lane. The measured emission factors, inferred from the line source model, increase with silt loading and vehicle weight, although there is scatter in the relationships. The emission factors show a decreasing trend with traffic flow rate per lane.

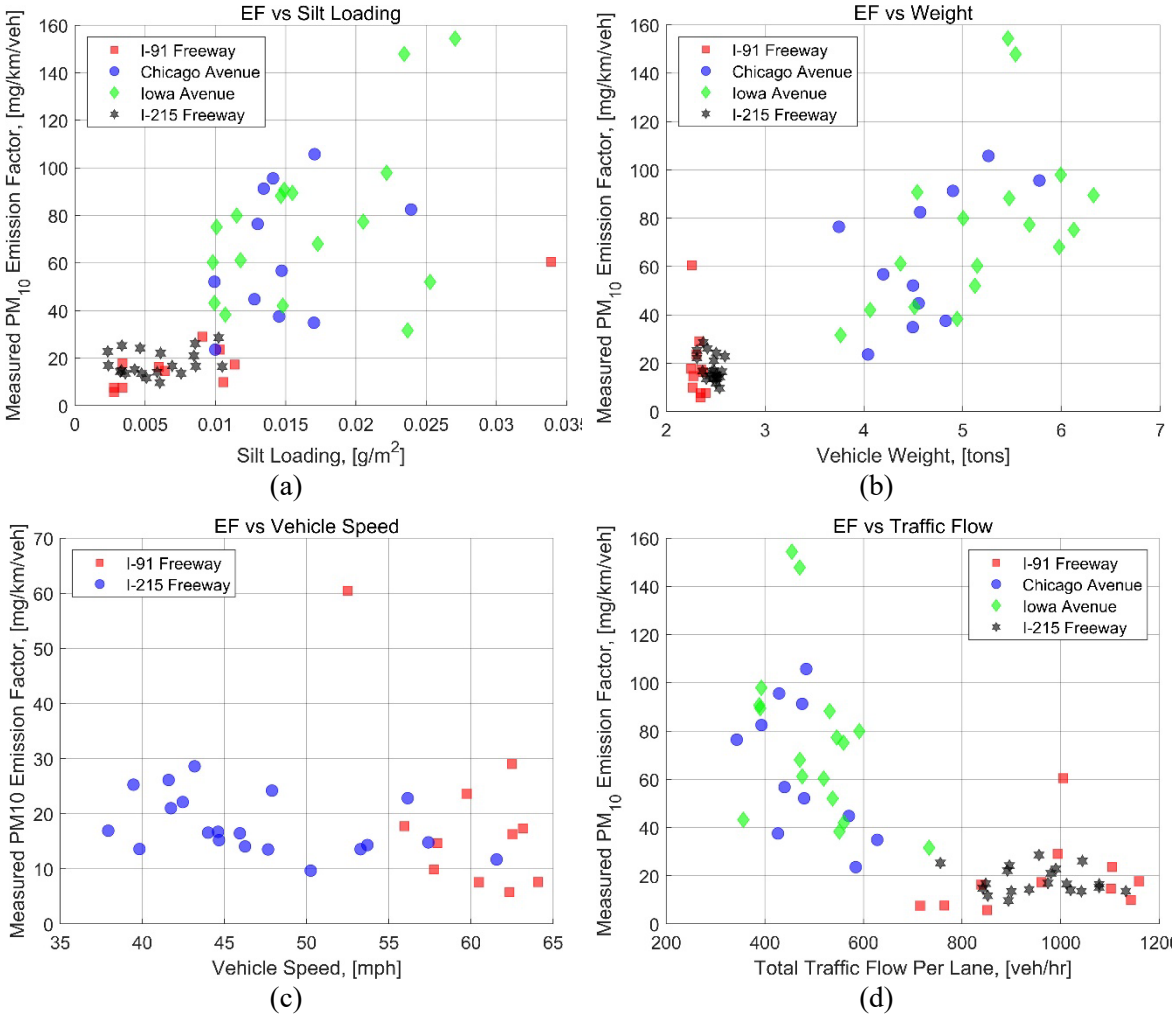

Figure 5.10. Relationship between dispersion model determined emission factors versus silt loading, vehicle weight, vehicle speed, and traffic flow per lane.

The simple model was used for estimates of emission factors and compared with results inferred from the line source model as described in the section 5.3.2 and 5.3.3. Figure 5.11 shows that the R^2 values are over 0.9 for both PM_{10} and $PM_{2.5}$, indicating a high concordance between the results of the simple model and the line source model.

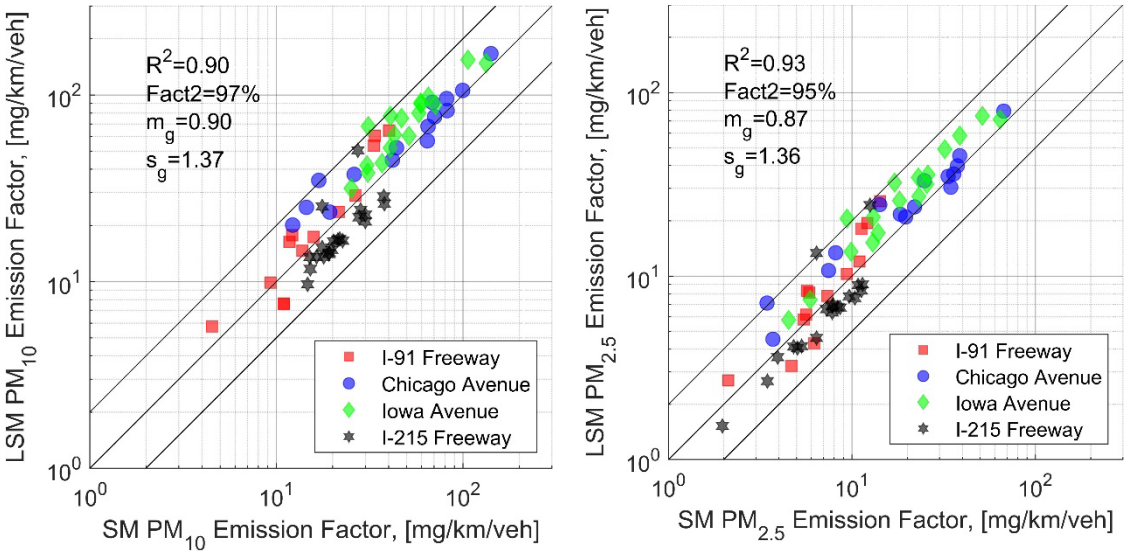

(a) (b)

Figure 5.11 The comparisons of PM_{10} and $PM_{2.5}$ emission factors inferred from simple model and line source model.

We expect road dust emission rates to depend on traffic volume, vehicle weight, vehicle speed, and meteorological conditions (such as wind speed, atmospheric stability, and precipitation) in the short term. Governing factors on a longer time scale include atmospheric reactions, deposition, and production (Reid et al., 2016). Notice that AP-42 is a semi-empirical model that lacks a mechanistic basis and relies on an input that is difficult to measure. The proposed system for measuring emission factors using a mobile platform overcomes the difficulty with measuring silt loading. To place the model on a mechanistic foundation we have derived a new equation that estimates the emission factors using silt loadings and vehicle The AP-42 equations and the new model for road dust emission rates and emission factors are listed in Table 5.4. The coefficient *k* in this study is determined by using a non-negative least-square method to best fit the on-road measurements. Tr and Vspd listed in the Table 5.4 are the traffic flow expressed as

veh/hr and the vehicle speed in mph obtained by the PeMS sensors or from the recorded video described before.

The comparisons (N=66) of emission rates derived from the AP-42 and our best-fit model are shown in Figure 5.12. We can see that for all the types of particulate matter pollutants, the R^2, Fact2, and m_g improve over those corresponding to the AP-42 model.

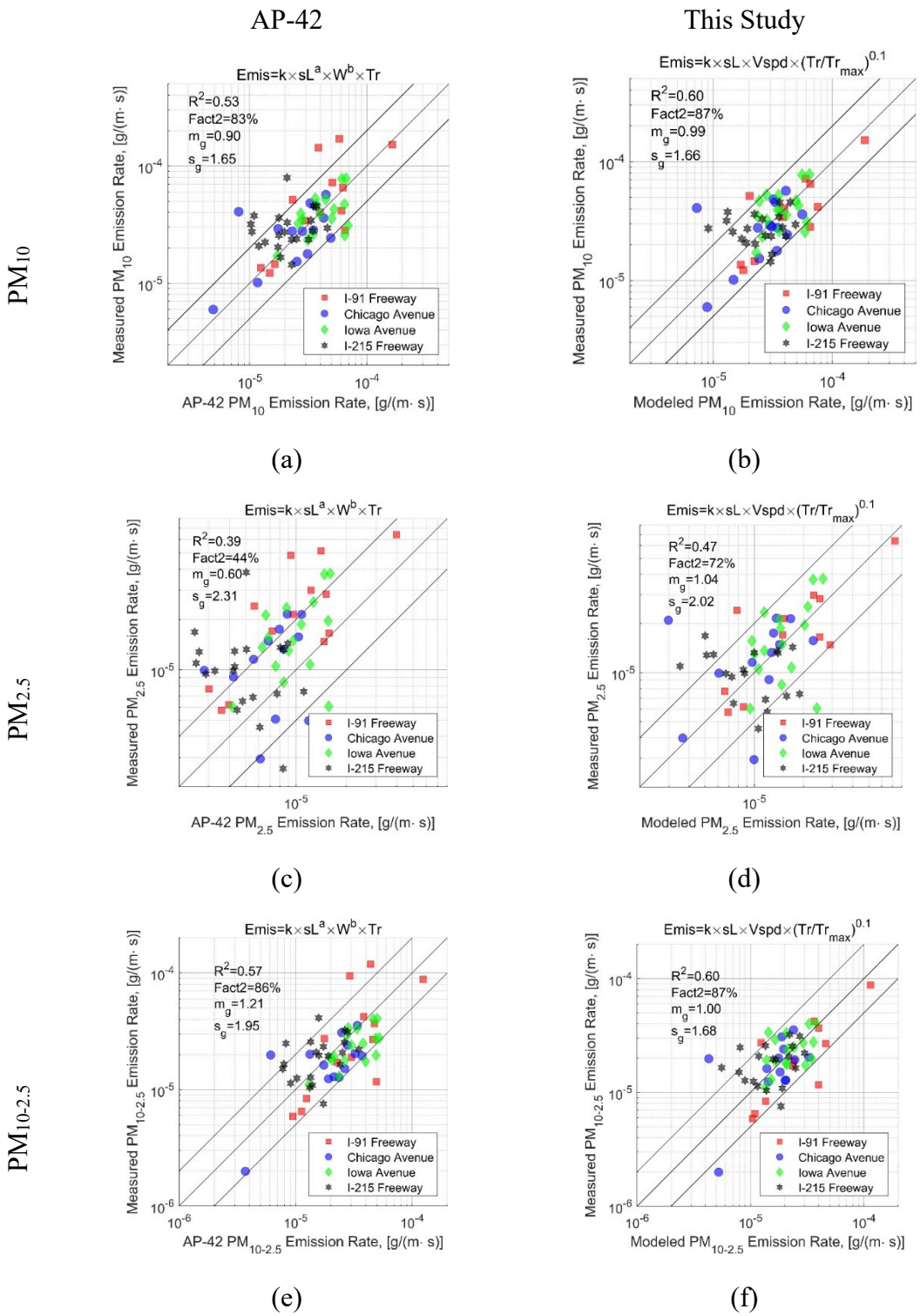

Figure 5.12. The scatter plots of AP-42 model and our best-fit model for PM_{10}, $PM_{2.5}$, and $PM_{10\text{-}2.5}$

Table 5.4. The comparisons of AP-42 equations and best-fit equations for road dust emission rate and emission factor

Emissions	Methods	Equation	Pollutants	k	a	b
Emission Rate	US EPA	$Emis = k \times (sL)^a \times (W)^b \times Tr$	PM_{10}	620	0.91	1.02
			$PM_{2.5}$	150	0.91	1.02
	This Study	$Emis = k \times sL \times Vspd \times \left(\frac{Tr}{Tr_{max}}\right)^{0.1}$	PM_{10}	2.0e-4	-	-
			$PM_{2.5}$	7.9e-5	-	-
Emission Factor	US EPA	$\mathrm{EF} = k \times (sL)^a \times (W)^b$	PM_{10}	620	0.91	1.02
			$PM_{2.5}$	150	0.91	1.02
	This Study	$\mathrm{EF} = k \times sL \times Vspd \times \frac{1}{Tr^{0.9} Tr_{max}^{0.1}}$	PM_{10}	2.8e6	-	-
			$PM_{2.5}$	1.2e6	-	-

In the context of comparing emission factors, we normalized the emission rate equations by the corresponding traffic flow values for both the AP-42 method and our model. Figure 5.13 illustrates scatter plots depicting the emission factors for PM_{10}, $PM_{2.5}$, and $PM_{10\text{-}2.5}$ for the AP-42 method and the proposed model. It is evident that the proposed model for $PM_{2.5}$ is a factor of 1.93 times larger than that obtained using the AP-42 method. The emission factors for PM_{10} and $PM_{10\text{-}2.5}$, form the two models show good agreement.

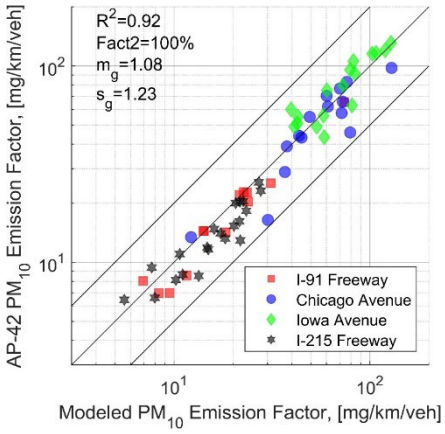

(a)

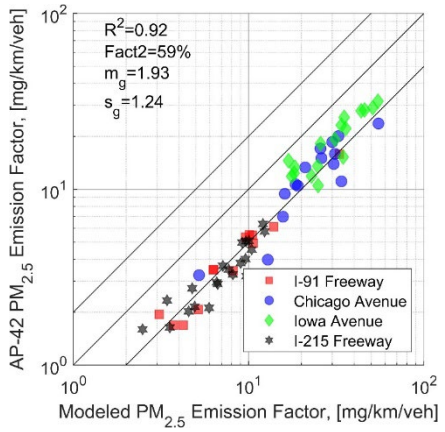

(b)

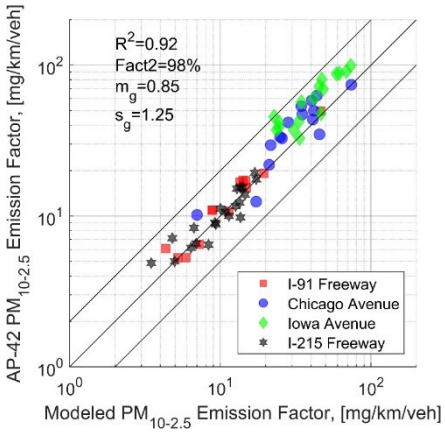

(c)

Figure 5.13. The scatter plot comparisons of PM_{10}, $PM_{2.5}$, and $PM_{10\text{-}2.5}$ emission factors determined by the AP-42 model and this study

5.4.4 Estimated Emission Factors compared with Default Values

We compare estimated emission factors from this study with reference values. CARB (2016) provided an independent road dust inventory that covers freeway and major roadways in Riverside. In Figure 5.14 we have depicted the estimation of PM_{10} and $PM_{2.5}$ emission factors using various methodologies, which include the line source model (LSM), the carbon mass balance (CMB) method, the AP-42 model with our vacuum sampling and suggested default inputs. Notably, regardless of the approach employed, we observe that the emission factors for city roads are significantly higher than those for freeways. Furthermore, when comparing these methods, it becomes evident that the emission factors calculated using the AP-42 method with default silt loadings and default weight are consistently higher than those obtained from the other four methodologies, which yield similar results. It shows that the default silt loadings in AP-42 were generally higher than those in southern California. This discrepancy may be attributed to the limited availability of crustal material for emissions in this region, leading to silt loadings stabilizing at lower levels due to the effective cleaning action of vehicle tires, as discussed by Fitz et al. (2020).

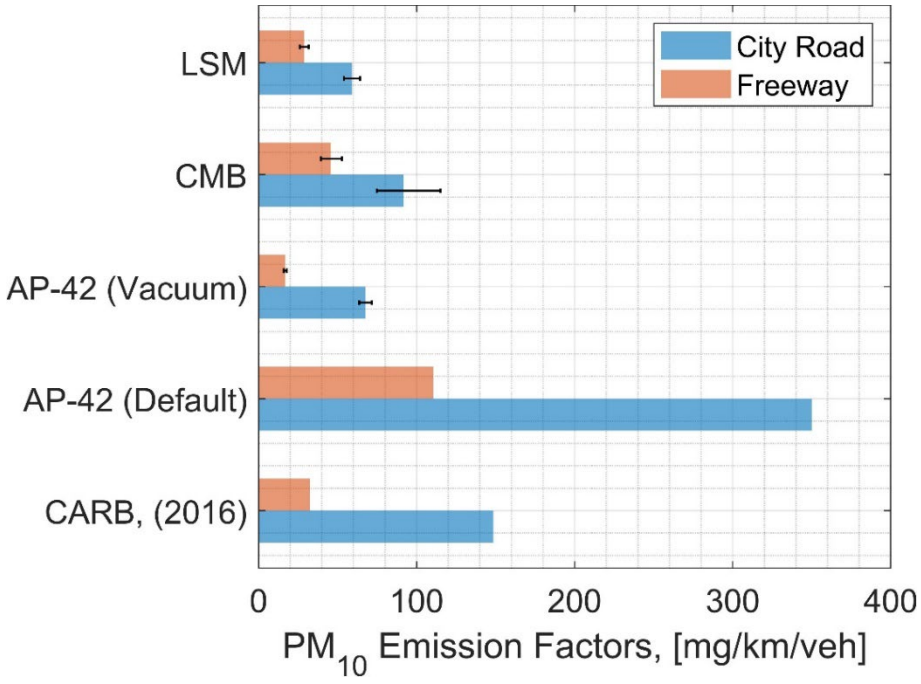

(a)

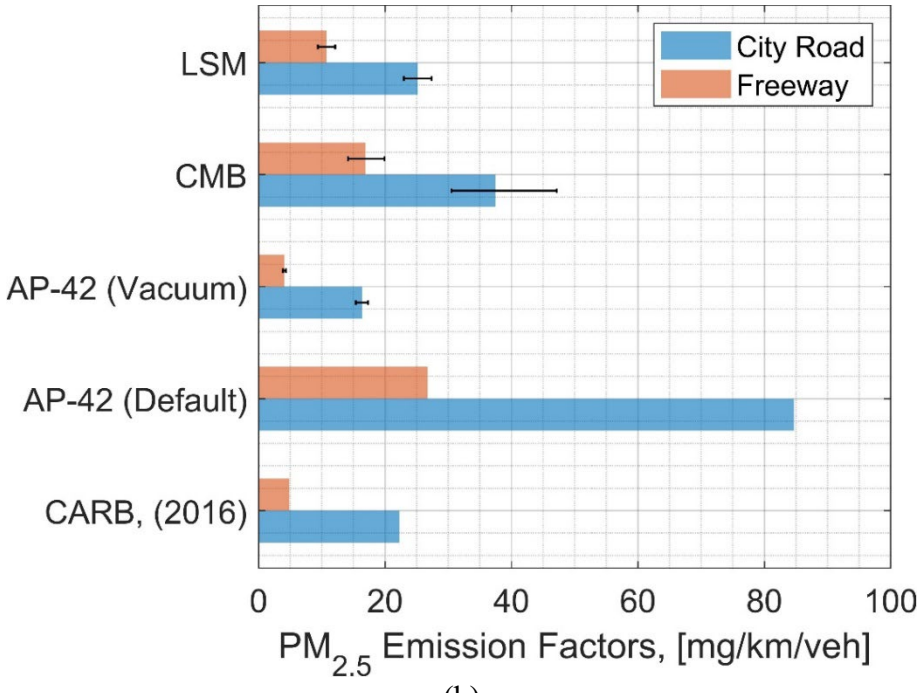

(b)

Figure 5.14. PM emission factors determined in this study compared to AP-42 default baselines and CARB inventory (CARB, 2016b). LSM stands for the line source model, CMB represents the carbon mass balance method, and AP-42 (Vacuum) incorporates silt loadings measured from a mobile vacuum dust system as input sources.

5.5 Conclusions

This study was motivated by the need for estimating emission factors for PM_{10} and $PM_{2.5}$ from roads. a practical approach to sample silt loadings on highways and busy roads, particularly in situations where the existing AP-42 procedures encounter deployment challenges. the portable vacuum dust collection system presented in this study provides a potential solution for silt loading sampling on a wide range of roads with decent uncertainty. Furthermore, we conducted experiments using the widely tested low-cost PM monitors (PurpleAir) on the mobile platform as a portable method for measuring PM concentrations. Another contribution in this study was to develop a physical structure model enhancing the accuracy of models used to estimate emission factors for paved roads dust, and this provides a theoretical explanation for road dust modeling work.

To achieve this, we implemented a portable vacuum dust collection system mounted on a mobile platform, which underwent the field studies on two freeways and two city roads. The mobile dust sampling system demonstrated 1σ uncertainty of 6.5% of the raw measurements through the continuous controlled test samplings. Simultaneously, we measured PM and CO2 concentrations using the vehicle-attached PurpleAir and PICARRO, respectively. We employed the downwind-upwind difference method to assess road contributions, and the 3-D micrometeorological inputs were derived from a vehicular attached 2-D sonic anemometer and a high-frequency bead thermistor (Thiruvenkatachari et al., 2023).

Our research incorporated dispersion models and the carbon mass balance method for comparison with the regulatory AP-42 approach, using both measured and default

baseline inputs. Additionally, we included an independent inventory of PM emission factors measured at the same location in 2008 (CARB, 2016b). Our findings (N=66) on-road tests indicate that all freeways exhibit lower PM_{10} and $PM_{2.5}$ emission factors compared to city roads. Notably, the AP-42 model with default inputs tends to overestimate dust emission factors while the other methods demonstrate good agreement. Based on our measurements, PM_{10} emission factors ranged from 17 to 46 [$\mathrm{mg\ km^{-1}\ veh^{-1}}$] for freeways and 59 to 149 [$\mathrm{mg\ km^{-1}\ veh^{-1}}$] for city roads. Similarly, PM2.5 emission factors ranged from 4 to 17 [$\mathrm{mg\ km^{-1}\ veh^{-1}}$] for freeways and 16 to 38 [$\mathrm{mg\ km^{-1}\ veh^{-1}}$] for city roads.

The physical structure model for road dust estimates includes the parameters of silt loadings, vehicle speed, and traffic flow. This model provides an explanation for the mechanism of the production the road dust. The new model shows an improved performance when compared to the AP-42 model.

6. Conclusions

6.1 Improving Spatial Resolution of $PM_{2.5}$ Measurements during Wildfires

The significant threat posed by large wildfires to air quality and public health arises from the release of harmful substances, particularly fine particulate matter ($PM_{2.5}$), in wildfire smoke. Conventional regulatory methods, mandated by the U.S. Clean Air Act, have limited spatial coverage in assessing $PM_{2.5}$ concentrations during wildfire events. Existing satellites provide daily aerosol optical depth (AOD) data, offering a global perspective in cloud-free regions but with limited temporal resolution. There is a critical need for technology that can comprehensively evaluate health risks at the community level with enhanced spatial and temporal resolution. This research seeks to bridge this gap by integrating ground monitor measurements with satellite observations using dispersion models.

An approach to construct highly resolved surface $PM_{2.5}$ maps by combining observations made at surface monitors and satellite data collected during wildfires was presented. Surface observations were firstly described using two dispersion models: a Lagrangian model based on backward trajectories generated with HRRR data from source to receptor and a segmented plume model that transports emissions from the source within a large-scale plume, whose horizontal dimensions are governed by trajectories originating from the sources. Estimates from these two models were fitted to surface observations to obtain emissions rates from sources. The satellite measurements of AOD, which measures column integrated $PM_{2.5}$, were also fitted to surface

observations using an empirical power law model. Because the results from the Lagrangian model were similar to those from the Plume model, the computationally efficient Plume model was used in most of the analysis.

The development of an empirical power equation allowed the estimation of $PM_{2.5}$ concentrations from AOD data obtained through the Moderate Resolution Imaging Spectroradiometer (MODIS) by NASA. The AOD model made a contribution to the correlation, R^2 ,between model estimates and surface observations; the contribution was relatively small on most days but can be significant on some days.

This model was used to construct 1 km resolved maps of surface $PM_{2.5}$ concentration during the October 2017 fires and the 2018 Camp Fire in Northern California. These maps interpolated between observations by combining model estimates with Kriged residuals between model estimates and observations. The residual Kriging maps showed greater spatial variation than that from simple Kriging, which just interpolates the measured concentrations.

This integrated technology facilitates the assessment of $PM_{2.5}$ concentrations at 1 km spatial resolution with 1-hour temporal resolution. Such precision not only enhances the evaluation of health risks but also holds the potential to predict wildfire impacts. In principle, the plume dispersion model is simple enough to allow updating of the parameters, horizontal plume spread and effective emission rate, in real time, which suggests that it can complement or be incorporated into a system (Marsha & Larkin, 2019 for example) to forecast ground-level $PM_{2.5}$ during wildfires.

6.2 Quantifying and Monitoring Methane Emissions from Dairy Farms in California Using TROPOMI and EM27/SUN Measurements

The application of a numerical dispersion model to infer methane emissions from a dairy cluster using column-averaged methane measurements upwind and downwind of the cluster is demonstrated. The model accounts for the geometry of the sources and the mean and turbulent structure of the atmospheric boundary layer in estimating concentrations associated with area sources of methane. The model also pays attention to the details of the geometry of the remote measurement method. The numerical model allows a straightforward incorporation of the vertical structure of the boundary layer into the model inputs to describe the three-dimensional concentration field resulting from an area source of emissions. This concentration field is then used to compute the average concentration along the line joining the instrument and the sun. The application is restricted to a horizontal spatial scale of the order of 10 kilometers over which the vertical structure of the boundary layer is assumed to be invariant.

Because onsite meteorological inputs are not routinely available, we examined the use of these inputs derived from the HRRR model. The emissions derived from these inputs were compared with those based on-site measurements. Although the emissions estimated using these two methods were similar, the HRRR modeled inputs introduced larger uncertainty in the emission estimates.

The model was also applied to two sets of methane measurements, one from a ground-based EM27/SUN and the second from a satellite-based system, and the results compared well. We show that measurements made by the TROPOMI combined with the

HRRR modeled meteorology can be used to infer CH_4 emissions from a cluster of dairy farms. The emission estimates from this approach compare well with those derived from on-site EM27/SUN column measurements and meteorology. This suggests that this satellite-based approach can be used to monitor the time variation of CH_4 emissions over selected dairy farms. This type of continuous monitoring is not practical with on-site field measurements.

6.3 Field Study to Estimate Exposure to Vehicle Exhaust During Idling and Starting

The adverse health effects associated with vehicle pollutants necessitate a thorough assessment of their impact on air quality near roads. A field study was designed to collect concentrations of tailpipe CO_2 at distances of meters from idling vehicles with varying wind speeds and stabilities. As the first step in interpreting the data, we examined the performance of a currently available point source dispersion model in describing the measured concentrations; this model is not designed for the spatial scales of the situation under study and does not account for the effects of the momentum of the exhaust plume.

The findings revealed that CO_2 concentrations were significantly higher than background values at meters from the tailpipe. A comparative analysis between measurements and modeled results indicated that existing dispersion models provide an accurate depiction when accounting for plume rise associated with the exhaust plume. Wake turbulence might not be important when the vehicle is stationary; Chang et al., (2012) show that turbulence in the wake of a moving vehicle has a major impact on the dilution of the exhaust plume.

To illustrate the application of a dispersion model designed for near-tailpipe exposure, we have used the results of the field study to estimate the risks of exposure to potential pollutants such as NO_2 and $PM_{2.5}$ during the situations described earlier. The results show that people waiting next to idling or slowly moving cars are likely to be exposed to high levels of NO_2.

The results from the field study described in this chapter are relevant to estimating exposure to vehicle emissions when customers are waiting for pick-up services by transportation network companies. Other similar situations to this near-road exposure case are: 1) young children waiting on the curb to be picked up after school; and 2) people waiting at curbside to cross the road at a signalized intersection, where vehicles stop and go in response to traffic lights.

6.4 An Assessment of Paved Road Dust Emissions Modeling

This study was motivated by the need for a practical approach to estimate PM emissions from roads, which are highly correlated with silt loading on roads. Current methods to measure silt loading require stopping traffic on a section of road, which is difficult to implement on most roads and almost impossible on freeways with varying traffic volumes. So current emission factor methods rely on default values of silt loading, which can lead to uncertainty in emission estimates. The major contribution of this study is to develop and deploy a system that allows measurements on a moving platform to 1) estimate silt loading on freeways using the mobile dust sampling system, 2) infer dust emission rates from roads, and 3) estimate micrometeorological inputs for the dispersion model uses. The PM concentrations used to infer to emission rates are made with widely

tested low-cost PM monitors (PurpleAir) mounted on the mobile platform. The micrometeorological variables are modeled with data from a 2D sonic anemometer and a bead thermistor (Thiruvenkatachari et al., 2023), which are portable to be mounted on a mobile platform. This technique addresses the challenges associated with setting up a 3D sonic anemometer, which typically requires time and careful leveling to ensure reliable measurements.

The new mobile system was used to collect data from several roads and highways, which was then used to a formulate emission factor model that has a better mechanistic foundation that the currently used AP-42 model. Emission factors of PM_{10} from the proposed model compared well with those from the AP-42 model, but $PM_{2.5}$ emission factors were almost a factor of two higher than those from the AP-42 model. The line source model and the simple model show a good agreement on the estimated PM emission factors. All freeways sampled in this chapter had lower PM_{10} and $PM_{2.5}$ emission factors compared to city roads, and the AP-42 model with default inputs tends to overestimate dust emission factors while the other methods demonstrate good agreement.

References

Ahangar, F.E., Freedman, F.R., Venkatram, A., 2019. Using low-cost air quality sensor networks to improve the spatial and temporal resolution of concentration maps. Int. J. Environ. Res. Public Health 16. https://doi.org/10.3390/ijerph16071252

Ahern, A.T., Robinson, E.S., Tkacik, D.S., Saleh, R., Hatch, L.E., Barsanti, K.C., Stockwell, C.E., Yokelson, R.J., Presto, A.A., Robinson, A.L., Sullivan, R.C., Donahue, N.M., 2019. Production of Secondary Organic Aerosol During Aging of Biomass Burning Smoke From Fresh Fuels and Its Relationship to VOC Precursors. J. Geophys. Res. Atmos. 124, 3583–3606. https://doi.org/10.1029/2018JD029068

Allen, D.T., 2014. Methane emissions from natural gas production and use: Reconciling bottom-up and top-down measurements. Curr. Opin. Chem. Eng. 5, 78–83. https://doi.org/10.1016/j.coche.2014.05.004

Alves, C.A., Evtyugina, M., Vicente, A.M.P., Vicente, E.D., Nunes, T. V., Silva, P.M.A., Duarte, M.A.C., Pio, C.A., Amato, F., Querol, X., 2018. Chemical profiling of PM10 from urban road dust. Sci. Total Environ. 634, 41–51. https://doi.org/10.1016/j.scitotenv.2018.03.338

Amato, F., Bedogni, M., Padoan, E., Querol, X., Ealo, M., Rivas, I., 2017. Characterization of road dust emissions in milan: Impact of vehicle fleet speed. Aerosol Air Qual. Res. 17, 2438–2449. https://doi.org/10.4209/aaqr.2017.01.0017

Amato, F., Cassee, F.R., Denier van der Gon, H.A.C., Gehrig, R., Gustafsson, M., Hafner, W., Harrison, R.M., Jozwicka, M., Kelly, F.J., Moreno, T., Prevot, A.S.H., Schaap, M., Sunyer, J., Querol, X., 2014. Urban air quality: The challenge of traffic non-exhaust emissions. J. Hazard. Mater. 275, 31–36. https://doi.org/10.1016/j.jhazmat.2014.04.053

Amini, S., Kuwayama, T., Gong, L., Falk, M., Chen, Y., Mitloehner, Q., Weller, S., Mitloehner, F.M., Patteson, D., Conley, S.A., Scheehle, E., FitzGibbon, M., 2022. Evaluating California dairy methane emission factors using short-term ground-level and airborne measurements. Atmos. Environ. X 14, 100171. https://doi.org/10.1016/j.aeaoa.2022.100171

Amiridis, V., Giannakaki, E., Balis, D.S., Gerasopoulos, E., Pytharoulis, I., Zanis, P., Kazadzis, S., Melas, D., Zerefos, C., 2010. Smoke injection heights from agricultural burning in Eastern Europe as seen by CALIPSO. Atmos. Chem. Phys. Discuss. 10, 19247–19276. https://doi.org/10.5194/acpd-10-19247-2010

Angevine, W.M., Bakwin, P.S., Davis, K.J., 1998. Wind profiler and RASS measurements compared with measurements from a 450-m-tall tower. J. Atmos. Ocean. Technol. 15, 818–825. https://doi.org/10.1175/1520-0426(1998)015<0818:WPARMC>2.0.CO;2

Appuhamy, R., Kebreab, E., 2018. Characterizing California-Specific Cattle Feed Rations and Improve Modeling of Enteric Fermentation for California'S Greenhouse Gas Inventory 2018 Final Report Contract 16Rd001 Prepared for: State of California Air Resources Board Research Division Po Box 90210.

B.B.Hicks, 1984. Behavior of Turbulence Statistics in the Convective Boundary Layer. Atmos. Turbul. Diffus. Div.

Barad, M.L., 1958. Project Prairie Grass: a field program in diffusion vol II. Geophys. Res. Pap. https://doi.org/10.1016/0022-460X(71)90105-2

Barkjohn, K.K., Gantt, B., Clements, A.L., 2021. Development and application of a United States-wide correction for PM2.5 data collected with the PurpleAir sensor. Atmos. Meas. Tech. 14, 4617–4637. https://doi.org/10.5194/amt-14-4617-2021

Bisig, C., Comte, P., Güdel, M., Czerwinski, J., Mayer, A., Müller, L., Petri-Fink, A., Rothen-Rutishauser, B., 2018. Assessment of lung cell toxicity of various gasoline engine exhausts using a versatile in vitro exposure system. Environ. Pollut. 235, 263–271. https://doi.org/10.1016/j.envpol.2017.12.061

Blaylock, B.K., Horel, J.D., Liston, S.T., 2017. Cloud archiving and data mining of High-Resolution Rapid Refresh forecast model output. Comput. Geosci. 109, 43–50. https://doi.org/10.1016/j.cageo.2017.08.005

Bogacki, M., Mazur, M., Oleniacz, R., Rzeszutek, M., Szulecka, A., 2018. Re-entrained road dust PM10 emission from selected streets of Krakow and its impact on air quality. E3S Web Conf. 28, 1–10. https://doi.org/10.1051/e3sconf/20182801003

Bovensmann, H., Buchwitz, M., Burrows, J.P., Reuter, M., Krings, T., Gerilowski, K., Schneising, O., Heymann, J., Tretner, A., Erzinger, J., 2010. A remote sensing technique for global monitoring of power plant CO 2 emissions from space and related applications. Atmos. Meas. Tech. 3, 781–811. https://doi.org/10.5194/amt-3-781-2010

Bukowiecki, N., Lienemann, P., Hill, M., Furger, M., Richard, A., Amato, F., Prévôt, A.S.H., Baltensperger, U., Buchmann, B., Gehrig, R., 2010. PM10 emission factors for non-exhaust particles generated by road traffic in an urban street canyon and along a freeway in Switzerland. Atmos. Environ. 44, 2330–2340. https://doi.org/10.1016/j.atmosenv.2010.03.039

Businger, J. a., Wyngaard, J.C., Izumi, Y., Bradley, E.F., 1971. Flux-Profile Relationships in the Atmospheric Surface Layer. J. Atmos. Sci. https://doi.org/10.1175/1520-0469(1971)028<0181:FPRITA>2.0.CO;2

Businger, J.A., 1973. Turbulence transfer in the atmospheric surface layer. Work. Micrometeorology 67–100.

Butz, A., Galli, A., Hasekamp, O., Landgraf, J., Tol, P., Aben, I., 2012. TROPOMI aboard Sentinel-5 Precursor: Prospective performance of CH 4 retrievals for aerosol and cirrus loaded atmospheres. Remote Sens. Environ. 120, 267–276. https://doi.org/10.1016/j.rse.2011.05.030

CALFIRE, 2018. Camp Fire Watershed Emergency Response Team (WERT) Report.

CALFIRE, 2017. CAL FIRE Fire Investigation Reports.

Caltrans, 2020. Pems User Guide Table of Contents.

CARB, 2020. California Greenhouse Gas Emissions for 2000 to 2017.

CARB, 2016a. State of California (2016).Senate Bill No.1383 [WWW Document]. URL https://leginfo.legislature.ca.gov/faces/billNavClient.xhtml?bill_id=201520160SB1383

CARB, 2016b. Miscellaneous Process Methodology 7.9 — Entrained Road Travel, Paved Road Dust.

CARB, 2015. California Air Resources Board: California Greenhouse Gas Emission Inventory [WWW Document]. URL https://ww2.arb.ca.gov/ghg-inventory-data

Cascio, W.E., 2018. Wildland fire smoke and human health. Sci. Total Environ. 624, 586–595. https://doi.org/10.1016/j.scitotenv.2017.12.086

Casotti Rienda, I., Alves, C.A., 2021. Road dust resuspension: A review. Atmos. Res. 261. https://doi.org/10.1016/j.atmosres.2021.105740

Chang, V.W., Hildemann, L.M., Chang, C., Chang, V.W., Hildemann, L.M., Chang, C., Chang, V.W., Hildemann, L.M., 2012. Dilution Rates for Tailpipe Emissions : Effects of Vehicle Shape , Tailpipe Position , and Exhaust Velocity Dilution Rates for Tailpipe Emissions : Effects of Vehicle Shape , Tailpipe Position , and Exhaust Velocity 2247. https://doi.org/10.3155/1047-3289.59.6.715

Chen, J., Viatte, C., Hedelius, J.K., Jones, T., Franklin, J.E., Parker, H., Gottlieb, E.W.,

Wennberg, P.O., Dubey, M.K., Wofsy, S.C., 2016. Differential column measurements using compact solar-tracking spectrometers. Atmos. Chem. Phys. 16, 8479–8498. https://doi.org/10.5194/acp-16-8479-2016

Chen, S., Zhang, X., Lin, J., Huang, J., Zhao, D., Yuan, T., Huang, K., Luo, Y., Jia, Z., Zang, Z., Qiu, Y., Xie, L., 2019. Fugitive road dust PM2.5 emissions and their potential health impacts. Environ. Sci. Technol. 53, 8455–8465. https://doi.org/10.1021/acs.est.9b00666

Cimorelli, A.J., Perry, S.G., Venkatram, A., Weil, J.C., Paine, R.J., Wilson, R.B., Lee, R.F., Peters, W.D., Brode, R.W., 2005. AERMOD: A Dispersion Model for Industrial Source Applications. Part I: General Model Formulation and Boundary Layer Characterization. J. Appl. Meteorol. 44, 682–693. https://doi.org/10.1175/JAM2227.1

Cui, Y.Y., Brioude, J., Angevine, W.M., Peischl, J., McKeen, S.A., Kim, S.W., Andrew Neuman, J., Henze, D.K., Bousserez, N., Fischer, M.L., Jeong, S., Michelsen, H.A., Bambha, R.P., Liu, Z., Santoni, G.W., Daube, B.C., Kort, E.A., Frost, G.J., Ryerson, T.B., Wofsy, S.C., Trainer, M., 2017. Top-down estimate of methane emissions in California using a mesoscale inverse modeling technique: The San Joaquin Valley. J. Geophys. Res. 122, 3686–3699. https://doi.org/10.1002/2016JD026398

Cui, Y.Y., Vijayan, A., Falk, M., Hsu, Y.K., Yin, D., Chen, X.M., Zhao, Z., Avise, J., Chen, Y., Verhulst, K., Duren, R., Yadav, V., Miller, C., Weiss, R., Keeling, R., Kim, J., Iraci, L.T., Tanaka, T., Johnson, M.S., Kort, E.A., Bianco, L., Fischer, M.L., Stroud, K., Herner, J., Croes, B., 2019. A Multiplatform Inversion Estimation of Statewide and Regional Methane Emissions in California during 2014-2016. Environ. Sci. Technol. 53, 9636–9645. https://doi.org/10.1021/acs.est.9b01769

Dallmann, T.R., Harley, R.A., 2010. Evaluation of mobile source emission trends in the United States. J. Geophys. Res. Atmos. 115, 1–12. https://doi.org/10.1029/2010JD013862

Deng, B., Chen, Y., Duan, X., Li, D., Li, Q., Tao, D., Ran, J., Hou, K., 2020. Dispersion behaviors of exhaust gases and nanoparticle of a passenger vehicle under simulated traffic light driving pattern. Sci. Total Environ. 740. https://doi.org/10.1016/j.scitotenv.2020.140090

Denier van der Gon, H., Hulskotte, J., Jozwicka, M., Kranenburg, R., Kuenen, J., Visschedijk, A., 2018. European Emission Inventories and Projections for Road Transport Non-Exhaust Emissions, Non-Exhaust Emissions: An Urban Air Quality Problem for Public Health; Impact and Mitigation Measures. Elsevier Inc. https://doi.org/10.1016/B978-0-12-811770-5.00005-4

Ding, Y., Cruz, I., Freedman, F., Venkatram, A., 2021. Improving spatial resolution of PM2.5 measurements during wildfires. Atmos. Pollut. Res. 12, 101047. https://doi.org/10.1016/j.apr.2021.03.010

Ding, Y., Zhao, X., Luo, J., Wu, G., Venkatram, A., 2022. Field Study to Estimate Exposure to Vehicle Exhaust During Idling and Starting. SSRN Electron. J. 14, 101632. https://doi.org/10.2139/ssrn.4063435

Eckman, R.M., 1994. Re-examination of empirically derived formulas for horizontal diffusion from surface sources. Atmos. Environ. 28, 265–272. https://doi.org/10.1016/1352-2310(94)90101-5

EPA, 2020. Inventory of U.S. greenhouse gas emissions and sinks: 1990-2018, Federal Register.

Fann, N., Alman, B., Broome, R.A., Morgan, G.G., Johnston, F.H., Pouliot, G., Rappold, A.G., 2018. The health impacts and economic value of wildland fire episodes in the U.S.: 2008–2012. Sci. Total Environ. 610–611, 802–809. https://doi.org/10.1016/j.scitotenv.2017.08.024

Finn, D., Clawson, K.L., Carter, R.G., Rich, J.D., Eckman, R.M., Perry, S.G., Isakov, V., Heist, D.K., 2010a. Tracer studies to characterize the effects of roadside noise barriers on near-road pollutant dispersion under varying atmospheric stability conditions q. Atmos. Environ. 44, 204–214. https://doi.org/10.1016/j.atmosenv.2009.10.012

Finn, D., Clawson, K.L., Carter, R.G., Rich, J.D., Eckman, R.M., Perry, S.G., Isakov, V., Heist, D.K., 2010b. Tracer studies to characterize the effects of roadside noise barriers on near-road pollutant dispersion under varying atmospheric stability conditions. Atmos. Environ. 44, 204–214. https://doi.org/10.1016/j.atmosenv.2009.10.012

Fitz, D.R., Bumiller, K., Bufalino, C., James, D.E., 2020. Real-time PM10 emission rates from paved roads by measurement of concentrations in the vehicle's wake using on-board sensors part 1. SCAMPER method characterization. Atmos. Environ. 230, 117483. https://doi.org/10.1016/j.atmosenv.2020.117483

Frankenberg, C., Thorpe, A.K., Thompson, D.R., Hulley, G., Kort, E.A., Vance, N., Borchardt, J., Krings, T., Gerilowski, K., Sweeney, C., Conley, S., Bue, B.D., Aubrey, A.D., Hook, S., Green, R.O., 2016. Airborne methane remote measurements reveal heavytail flux distribution in Four Corners region. Proc. Natl. Acad. Sci. U. S. A. 113, 9734–9739. https://doi.org/10.1073/pnas.1605617113

Geng, G., Murray, N.L., Tong, D., Fu, J.S., Hu, X., Lee, P., Meng, X., Chang, H.H., Liu,

Y., 2018. Satellite-Based Daily PM2.5 Estimates During Fire Seasons in Colorado. J. Geophys. Res. Atmos. 123, 8159–8171. https://doi.org/10.1029/2018JD028573

Gisi, M., Hase, F., Dohe, S., Blumenstock, T., Simon, A., Keens, A., 2012. XCO 2 - measurements with a tabletop FTS using solar absorption spectroscopy . Atmos. Meas. Tech. Discuss. 5, 5691–5724. https://doi.org/10.5194/amtd-5-5691-2012

Gupta, P., Christopher, S.A., Wang, J., Gehrig, R., Lee, Y., Kumar, N., 2006. Satellite remote sensing of particulate matter and air quality assessment over global cities. Atmos. Environ. 40, 5880–5892. https://doi.org/10.1016/j.atmosenv.2006.03.016

Gupta, P., Doraiswamy, P., Levy, R., Pikelnaya, O., Maibach, J., Feenstra, B., Polidori, A., Kiros, F., Mills, K.C., 2018. Impact of California Fires on Local and Regional Air Quality: The Role of a Low-Cost Sensor Network and Satellite Observations. GeoHealth 2, 172–181. https://doi.org/10.1029/2018gh000136

Gyawali, M., Arnott, W.P., Lewis, K., Street, N.V., 2009. In situ aerosol optics in Reno, NV, USA during and after the summer 2008 California wildfires and the influence of absorbing and non-absorbing organic coatings on spectral light absorption. Atmos. Chem. Phys. 2, 8007–8015.

Haan, P. De, Rotach, M.W., 1995. A puff-particle dispersion model. Int. J. Environ. Pollut. 5, 350–359.

Han, S., Youn, J.S., Jung, Y.W., 2011. Characterization of PM10 and PM2.5 source profiles for resuspended road dust collected using mobile sampling methodology. Atmos. Environ. 45, 3343–3351. https://doi.org/10.1016/j.atmosenv.2011.04.015

Harrison, R.M., Jones, A.M., Gietl, J., Yin, J., Green, D.C., 2012. Estimation of the contributions of brake dust, tire wear, and resuspension to nonexhaust traffic particles derived from atmospheric measurements. Environ. Sci. Technol. 46, 6523–6529. https://doi.org/10.1021/es300894r

Hasekamp, O., Lorente, A., Hu, H., Butz, A., aan de Brugh, J., Jochen Landgraf, 2019. Algorithm Theoretical Baseline Document for Sentinel-5 Precursor Methane Retrieval, Atbd.

Hedelius, J.K., Viatte, C., Wunch, D., Roehl, C.M., Toon, G.C., Chen, J., Jones, T., Wofsy, S.C., Franklin, J.E., Parker, H., Dubey, M.K., Wennberg, P.O., 2016. Assessment of errors and biases in retrievals of XCO2, XCH4, XCO, and XN2O from a 0.5 cm-1 resolution solar-viewing spectrometer. Atmos. Meas. Tech. 9, 3527–3546. https://doi.org/10.5194/amt-9-3527-2016

Heerah, S., Frausto-Vicencio, I., Jeong, S., Marklein, A.R., Ding, Y., Meyer, A.G.,

Parker, H.A., Fischer, M.L., Franklin, J.E., Hopkins, F.M., Dubey, M., 2021. Dairy Methane Emissions in California's San Joaquin Valley Inferred Using Ground-based Remote Sensing Field Observations in the Summer and Winter. J. Geophys. Res. Atmos. 1–36. https://doi.org/10.1029/2021jd034785

HEI, 2010. Traffic-Related Air Pollution: A Critical Review of the Literature on Emissions , Exposure , and Health Effects. Heal. Eff. Inst.

Heist, D.K., Perry, S.G., Brixey, L.A., 2009. A wind tunnel study of the effect of roadway configurations on the dispersion of traffic-related pollution. Atmos. Environ. 43, 5101–5111. https://doi.org/10.1016/j.atmosenv.2009.06.034

Hidy, G.M., Brook, J.R., Chow, J.C., Green, M., Husar, R.B., Lee, C., Scheffe, R.D., Swanson, A., Watson, J.G., 2009. Remote sensing of particulate pollution from space: Have we reached the promised land? J. Air Waste Manag. Assoc. 59, 1130–1139. https://doi.org/10.3155/1047-3289.59.10.1130

Hoff, R.M., Christopher, S.A., 2009. Remote sensing of particulate pollution from space: Have we reached the promised land? J. Air Waste Manag. Assoc. 59, 645–675. https://doi.org/10.3155/1047-3289.59.6.645

Hristov, A.N., Harper, M., Meinen, R., Day, R., Lopes, J., Ott, T., Venkatesh, A., Randles, C.A., 2017. Discrepancies and Uncertainties in Bottom-up Gridded Inventories of Livestock Methane Emissions for the Contiguous United States. Environ. Sci. Technol. 51, 13668–13677. https://doi.org/10.1021/acs.est.7b03332

Hurteau, M.D., Westerling, A.L., Wiedinmyer, C., Bryant, B.P., 2014. Projected Effects of Climate and Development on California Wildfire Emissions through 2100. Environ. Sci. Technol. 48, 2298–2304. https://doi.org/10.1021/es4050133

IPCC, 2013. Climate change 2013 the physical science basis: Working Group I contribution to the fifth assessment report of the intergovernmental panel on climate change, Cambridge University Press, Cambridge, United Kingdom and New York, NY, USA. https://doi.org/10.1017/CBO9781107415324

Isakov, V., Venkatram, A., Touma, J.S., Koračin, D., Otte, T.L., 2007. Evaluating the use of outputs from comprehensive meteorological models in air quality modeling applications. Atmos. Environ. 41, 1689–1705. https://doi.org/10.1016/j.atmosenv.2006.10.043

Jacob, D.J., Turner, A.J., Maasakkers, J.D., Sheng, J., Sun, K., Liu, X., Chance, K., Aben, I., McKeever, J., Frankenberg, C., 2016. Satellite observations of atmospheric methane and their value for quantifying methane emissions. Atmos. Chem. Phys. 16, 14371–14396. https://doi.org/10.5194/acp-16-14371-2016

Jacob, D.J., Varon, D.J., Cusworth, D.H., Dennison, P.E., Frankenberg, C., Gautam, R., Guanter, L., Kelley, J., McKeever, J., Ott, L.E., Poulter, B., Qu, Z., Thorpe, A.K., Worden, J.R., Duren, R.M., 2022. Quantifying methane emissions from the global scale down to point sources using satellite observations of atmospheric methane. Atmos. Chem. Phys. 22, 9617–9646. https://doi.org/10.5194/acp-22-9617-2022

Jacobs, N., Simpson, W.R., Wunch, D., O'Dell, C.W., Osterman, G.B., Hase, F., Blumenstock, T., Tu, Q., Frey, M., Dubey, M.K., Parker, H.A., Kivi, R., Heikkinen, P., 2020. Quality controls, bias, and seasonality of CO2columns in the boreal forest with Orbiting Carbon Observatory-2, Total Carbon Column Observing Network, and EM27/SUN measurements. Atmos. Meas. Tech. 13, 5033–5063. https://doi.org/10.5194/amt-13-5033-2020

Jalali Farahani, V., Altuwayjiri, A., Taghvaee, S., Sioutas, C., 2022. Tailpipe and Nontailpipe Emission Factors and Source Contributions of PM10on Major Freeways in the Los Angeles Basin. Environ. Sci. Technol. 56, 7029–7039. https://doi.org/10.1021/acs.est.1c06954

Jeong, S., Newman, S., Zhang, J., Andrews, A.E., Bianco, L., Bagley, J., Cui, X., Graven, H., Kim, J., Salameh, P., LaFranchi, B.W., Priest, C., Campos-Pineda, M., Novakovskaia, E., Sloop, C.D., Michelsen, H.A., Bambha, R.P., Weiss, R.F., Keeling, R., Fischer, M.L., 2016. Estimating methane emissions in california's urban and rural regions using multitower observations. J. Geophys. Res. 121, 13,031-13,049. https://doi.org/10.1002/2016JD025404

Jeong, S., Zhao, C., Andrews, A.E., Bianco, L., Wilczak, J.M., Fischer, M.L., 2012. Seasonal variation of CH4 emissions from central California. J. Geophys. Res. Atmos. 117, 1–15. https://doi.org/10.1029/2011JD016896

Jongaramrungruang, S., Frankenberg, C., Matheou, G., Thorpe, A.K., 2019. Towards accurate methane point-source quantification from high-resolution 2-D plume imagery 6667–6681.

Jose, J., Srimuruganandam, B., 2020. Investigation of road dust characteristics and its associated health risks from an urban environment. Environ. Geochem. Health 42, 2819–2840. https://doi.org/10.1007/s10653-020-00521-6

Karakurt, I., Aydin, G., Aydiner, K., 2012. Sources and mitigation of methane emissions by sectors: A critical review. Renew. Energy 39, 40–48. https://doi.org/10.1016/j.renene.2011.09.006

Kasler, D., 2017. Wine country wildfire costs now top $9 billion, costliest in California history. Sacramento Bee.

Kelly, K.E., Whitaker, J., Petty, A., Widmer, C., Dybwad, A., Sleeth, D., Martin, R., Butterfield, A., 2017. Ambient and laboratory evaluation of a low-cost particulate matter sensor. Environ. Pollut. 221, 491–500. https://doi.org/10.1016/j.envpol.2016.12.039

Kenty, K.L., Poor, N.D., Kronmiller, K.G., McClenny, W., King, C., Atkeson, T., Campbell, S.W., 2007. Application of CALINE4 to roadside NO/NO2 transformations. Atmos. Environ. 41, 4270–4280. https://doi.org/10.1016/j.atmosenv.2006.06.066

Khan, R.K., Strand, M.A., 2018. Road dust and its effect on human health: A literature review. Epidemiol. Health 1–11. https://doi.org/10.4178/EPIH.E2018013

Kirschke, S., Bousquet, P., Ciais, P., Saunois, M., Canadell, J.G., Dlugokencky, E.J., Bergamaschi, P., Bergmann, D., Blake, D.R., Bruhwiler, L., Cameron-Smith, P., Castaldi, S., Chevallier, F., Feng, L., Fraser, A., Heimann, M., Hodson, E.L., Houweling, S., Josse, B., Fraser, P.J., Krummel, P.B., Lamarque, J.F., Langenfelds, R.L., Le Quéré, C., Naik, V., O'doherty, S., Palmer, P.I., Pison, I., Plummer, D., Poulter, B., Prinn, R.G., Rigby, M., Ringeval, B., Santini, M., Schmidt, M., Shindell, D.T., Simpson, I.J., Spahni, R., Steele, L.P., Strode, S.A., Sudo, K., Szopa, S., Van Der Werf, G.R., Voulgarakis, A., Van Weele, M., Weiss, R.F., Williams, J.E., Zeng, G., 2013. Three decades of global methane sources and sinks. Nat. Geosci. 6, 813–823. https://doi.org/10.1038/ngeo1955

Kumar, A., Elumalai, S.P., 2018. Influence of Road Paving on Particulate Matter Emission and Fingerprinting of Elements of Road Dust. Arch. Environ. Contam. Toxicol. 75, 424–435. https://doi.org/10.1007/s00244-018-0546-6

Kumar, P., Morawska, L., Martani, C., Biskos, G., Neophytou, M., Di Sabatino, S., Bell, M., Norford, L., Britter, R., 2015. The rise of low-cost sensing for managing air pollution in cities. Environ. Int. 75, 199–205. https://doi.org/10.1016/j.envint.2014.11.019

Kuula, J., Mäkelä, T., Hillamo, R., Timonen, H., 2017. Response characterization of an inexpensive aerosol sensor. Sensors (Switzerland) 17. https://doi.org/10.3390/s17122915

Larkin, N.K., O'Neill, S.M., Solomon, R., Raffuse, S., Strand, T., Sullivan, D.C., Krull, C., Rorig, M., Peterson, J., Ferguson, S.A., 2009. The BlueSky smoke modeling framework. Int. J. Wildl. Fire 18, 906–920. https://doi.org/10.1071/WF07086

Laumbach, R.J., Kipen, H.M., 2012. Respiratory health effects of air pollution: Update on biomass smoke and traffic pollution. J. Allergy Clin. Immunol. 129, 3–11.

https://doi.org/10.1016/j.jaci.2011.11.021

Lauvaux, T., Davis, K.J., 2014. Planetary boundary layer errors in mesoscale inversions of column-integrated CO2 measurements. J. Geophys. Res. 119, 490–508. https://doi.org/10.1002/2013JD020175

Lawson, C.L., Hanson, R.J., 1974. Solving Least Square Problems. Prentice-Hall.

Le, T.C., Shukla, K.K., Chen, Y.T., Chang, S.C., Lin, T.Y., Li, Z., Pui, D.Y.H., Tsai, C.J., 2020. On the concentration differences between PM2.5 FEM monitors and FRM samplers. Atmos. Environ. 222, 117138. https://doi.org/10.1016/j.atmosenv.2019.117138

Levy Zamora, M., Xiong, F., Gentner, D., Kerkez, B., Kohrman-Glaser, J., Koehler, K., 2019. Field and Laboratory Evaluations of the Low-Cost Plantower Particulate Matter Sensor. Environ. Sci. Technol. 53, 838–849. https://doi.org/10.1021/acs.est.8b05174

Li, L., Girguis, M., Lurmann, F., Pavlovic, N., McClure, C., Franklin, M., Wu, J., Oman, L.D., Breton, C., Gilliland, F., Habre, R., 2020. Ensemble-based deep learning for estimating PM2.5 over California with multisource big data including wildfire smoke. Environ. Int. 145, 106143. https://doi.org/10.1016/j.envint.2020.106143

Lipsett, M.; Materna, B.; Lyon Stone, S.; Therriault, S.; Blaisdell, R.; Cook, J., 2008. Wildfire Smoke—A Guide for Public Health Officials.

Liu, Y., Sarnat, J.A., Kilaru, V., Jacob, D.J., Koutrakis, P., 2005. Estimating ground-level PM2.5 in the eastern United States using satellite remote sensing. Environ. Sci. Technol. 39, 3269–3278. https://doi.org/10.1021/es049352m

Ljungman, P.L.S., Andersson, N., Stockfelt, L., Andersson, E.M., Sommar, J.N., Eneroth, K., Gidhagen, L., Johansson, C., Lager, A., Leander, K., Molnar, P., Pedersen, N.L., Rizzuto, D., Rosengren, A., Segersson, D., Wennberg, P., Barregard, L., Forsberg, B., Sallsten, G., Bellander, T., Pershagen, G., 2019. Long-term exposure to particulate air pollution, black carbon, and their source components in relation to ischemic heart disease and stroke. Environ. Health Perspect. 127, 1–11. https://doi.org/10.1289/EHP4757

Lorente, A., Borsdorff, T., Butz, A., Hasekamp, O., Aan De Brugh, J., Schneider, A., Wu, L., Hase, F., Kivi, R., Wunch, D., Pollard, D.F., Shiomi, K., Deutscher, N.M., Velazco, V.A., Roehl, C.M., Wennberg, P.O., Warneke, T., Landgraf, J., 2021. Methane retrieved from TROPOMI: Improvement of the data product and validation of the first 2 years of measurements. Atmos. Meas. Tech. 14, 665–684. https://doi.org/10.5194/amt-14-665-2021

Luther, A., Kleinschek, R., Scheidweiler, L., Defratyka, S., Stanisavljevic, M., Forstmaier, A., Dandocsi, A., Wolff, S., Dubravica, D., Wildmann, N., Kostinek, J., Jöckel, P., Nickl, A.L., Klausner, T., Hase, F., Frey, M., Chen, J., Dietrich, F., Necki, J., Swolkień, J., Fix, A., Roiger, A., Butz, A., 2019. Quantifying CH4 emissions from hard coal mines using mobile sun-viewing Fourier transform spectrometry. Atmos. Meas. Tech. 12, 5217–5230. https://doi.org/10.5194/amt-12-5217-2019

Lyapustin, A., Wang, Y., 2018. MODIS Multi-Angle Implementation of Atmospheric Correction (MAIAC) Data User ' s Guide 6.

Lyapustin, A., Wang, Y., Laszlo, I., Kahn, R., Korkin, S., Remer, L., Levy, R., Reid, J.S., 2011. Multiangle implementation of atmospheric correction (MAIAC): 2. Aerosol algorithm. J. Geophys. Res. Atmos. 116, 1–15. https://doi.org/10.1029/2010JD014986

Maasakkers, J.D., Jacob, D.J., Sulprizio, M.P., Turner, A.J., Weitz, M., Wirth, T., Hight, C., DeFigueiredo, M., Desai, M., Schmeltz, R., Hockstad, L., Bloom, A.A., Bowman, K.W., Jeong, S., Fischer, M.L., 2016. Gridded National Inventory of U.S. Methane Emissions. Environ. Sci. Technol. 50, 13123–13133. https://doi.org/10.1021/acs.est.6b02878

Mangino, J., Bartram, D., Brazy, A., 2002. Development of a methane conversion factor to estimate emissions from animal waste lagoons. 11th Int. Emiss. Invent. Conf.

Marklein, A., Meyer, D., Fischer;, M.L., Jeong;, S., Rafiq;, T., Carr;, M., Hopkins;, F.M., 2020. Facility scale inventory of dairy methane emissions in California: Implications for mitigation. Earth Syst. Sci. Data.

Marklein, A.R., Meyer, D., Fischer, M.L., Jeong, S., Rafiq, T., Carr, M., Hopkins, F.M., 2021. Facility-scale inventory of dairy methane emissions in California: Implications for mitigation. Earth Syst. Sci. Data 13, 1151–1166. https://doi.org/10.5194/essd-13-1151-2021

Marsha, A., Larkin, N.K., 2019. A statistical model for predicting PM 2.5 for the western United States . J. Air Waste Manage. Assoc. 69, 1215–1229. https://doi.org/10.1080/10962247.2019.1640808

Martin, M.V., Kahn, R.A., Tosca, M.G., 2018. A global analysis of wildfire smoke injection heights derived from space-based multi-angle imaging. Remote Sens. 10. https://doi.org/10.3390/rs10101609

Mass, C.F., Ovens, D., 2019. The northern California wildfires of 8–9 October 2017: The

Role of a Major Downslope Wind Event. Bull. Am. Meteorol. Soc. 100, 235–256. https://doi.org/10.1175/BAMS-D-18-0037.1

Matthaios, V.N., Lawrence, J., Martins, M.A.G., Ferguson, S.T., Wolfson, J.M., Harrison, R.M., Koutrakis, P., 2022. Quantifying factors affecting contributions of roadway exhaust and non-exhaust emissions to ambient PM10–2.5 and PM2.5–0.2 particles. Sci. Total Environ. 835, 155368. https://doi.org/10.1016/j.scitotenv.2022.155368

McMillan, A.M.S., Goulden, M.L., Tyler, S.C., 2007. Stoichiometry of CH4 and CO2 flux in a California rice paddy. J. Geophys. Res. Biogeosciences 112, 1–13. https://doi.org/10.1029/2006JG000198

McNabola, A., Broderick, B.M., Gill, L.W., 2009. The impacts of inter-vehicle spacing on in-vehicle air pollution concentrations in idling urban traffic conditions. Transp. Res. Part D Transp. Environ. 14, 567–575. https://doi.org/10.1016/j.trd.2009.08.003

Morawska, L., Thai, P.K., Liu, X., Asumadu-Sakyi, A., Ayoko, G., Bartonova, A., Bedini, A., Chai, F., Christensen, B., Dunbabin, M., Gao, J., Hagler, G.S.W., Jayaratne, R., Kumar, P., Lau, A.K.H., Louie, P.K.K., Mazaheri, M., Ning, Z., Motta, N., Mullins, B., Rahman, M.M., Ristovski, Z., Shafiei, M., Tjondronegoro, D., Westerdahl, D., Williams, R., 2018. Applications of low-cost sensing technologies for air quality monitoring and exposure assessment: How far have they gone? Environ. Int. 116, 286–299. https://doi.org/10.1016/j.envint.2018.04.018

Nieuwstadt, F.T.M., van Ulden, A.P., 1978. A numerical study on the vertical dispersion of passive contaminants from a continuous source in the atmospheric surface layer. Atmos. Environ. 12, 2119–2124. https://doi.org/10.1016/0004-6981(78)90166-X

Nieuwstadt, F.T.M., Van Ulden, A.P., 1980. A numerical study of the vertical dispersion of passive contaminants from a continuous source in the atmospheric surface layer. Atmos. Environ. 14, 267–269. https://doi.org/10.1016/0004-6981(80)90288-7

Ning, Z., Cheung, C.S., Lu, Y., Liu, M.A., Hung, W.T., 2005. Experimental and numerical study of the dispersion of motor vehicle pollutants under idle condition. Atmos. Environ. 39, 7880–7893. https://doi.org/10.1016/j.atmosenv.2005.09.020

Noble, C.A., Vanderpool, R.W., Peters, T.M., McElroy, F.F., Gemmill, D.B., Wiener, R.W., 2001. Federal reference and equivalent methods for measuring fine particulate matter. Aerosol Sci. Technol. 34, 457–464. https://doi.org/10.1080/02786820121582

OECD, 2020. Non-exhaust Particulate Emissions from Road Transport, Non-exhaust Particulate Emissions from Road Transport. https://doi.org/10.1787/4a4dc6ca-en

Ottmar, R.D., n.d. Smoke Management Guide for Prescribed and Wildland Fire.

Park, S.S., Kozawa, K., Fruin, S., Mara, S., Hsu, Y.K., Jakober, C., Winer, A., Herner, J., 2011. Emission Factors for High-Emitting Vehicles Based on On-Road Measurements of Individual Vehicle Exhaust with a Mobile Measurement Platform. J. Air Waste Manag. Assoc. 61, 1046–1056. https://doi.org/10.1080/10473289.2011.595981

Paugam, R., Wooster, M., Freitas, S., Val Martin, M., 2016. A review of approaches to estimate wildfire plume injection height within large-scale atmospheric chemical transport models. Atmos. Chem. Phys. 16, 907–925. https://doi.org/10.5194/acp-16-907-2016

Pournazeri, S., Tan, S., Schulte, N., Jing, Q., Venkatram, A., 2014. A computationally efficient model for estimating background concentrations of NOx, NO2, and O3. Environ. Model. Softw. 52, 19–37. https://doi.org/10.1016/j.envsoft.2013.10.018

Qian, W., Princevac, M., Venkatram, A., 2010. Using temperature fluctuation measurements to estimate meteorological inputs for modelling dispersion during convective conditions in urban areas. Boundary-Layer Meteorol. 135, 269–289. https://doi.org/10.1007/s10546-010-9479-y

Qu, Z., Jacob, D.J., Shen, L., Lu, X., Zhang, Y., Scarpelli, T.R., Nesser, H., Sulprizio, M.P., Maasakkers, J.D., Bloom, A.A., Worden, J.R., Parker, R.J., Delgado, A.L., 2021. Global distribution of methane emissions: A comparative inverse analysis of observations from the TROPOMI and GOSAT satellite instruments. Atmos. Chem. Phys. 21, 14159–14175. https://doi.org/10.5194/acp-21-14159-2021

Reid, C.E., Brauer, M., Johnston, F.H., Jerrett, M., Balmes, J.R., Elliott, C.T., 2016. Critical Review of Health Impacts of Wildfire Smoke Exposure 1334, 1334–1343.

Reid, S., Bai, S., Du, Y., Craig, K., Erdakos, G., Baringer, L., Eisinger, D., McCarthy, M., Landsberg, K., 2016. Emissions modeling with MOVES and EMFAC to assess the potential for a transportation project to create particulate matter hot spots. Transp. Res. Rec. 2570, 12–20. https://doi.org/10.3141/2570-02

Remer, L.A., Kaufman, Y.J., Tanré, D., Mattoo, S., Chu, D.A., Martins, J. V., Li, R.-R., Ichoku, C., Levy, R.C., Kleidman, R.G., Eck, T.F., Vermote, E., Holben, B.N., 2005. The MODIS Aerosol Algorithm, Products, and Validation. J. Atmos. Sci. 62, 947–973. https://doi.org/10.1175/jas3385.1

Rolph, G., Stein, A., Stunder, B., 2017a. Real-time Environmental Applications and Display sYstem: READY. Environ. Model. Softw. 95, 210–228. https://doi.org/10.1016/j.envsoft.2017.06.025

Rolph, G., Stein, A., Stunder, B., 2017b. Real-time Environmental Applications and Display sYstem: READY. Environ. Model. Softw. 95, 210–228. https://doi.org/10.1016/j.envsoft.2017.06.025

Saunois, Marielle, Bousquet, P., Poulter, B., Peregon, A., Ciais, P., Canadell, J.G., Dlugokencky, E.J., Etiope, G., Bastviken, D., Houweling, S., Janssens-Maenhout, G., Tubiello, F.N., Castaldi, S., Jackson, R.B., Alexe, M., Arora, V.K., Beerling, D.J., Bergamaschi, P., Blake, D.R., Brailsford, G., Brovkin, V., Bruhwiler, L., Crevoisier, C., Crill, P., Covey, K., Curry, C., Frankenberg, C., Gedney, N., Höglund-Isaksson, L., Ishizawa, M., Ito, A., Joos, F., Kim, H.S., Kleinen, T., Krummel, P., Lamarque, J.F., Langenfelds, R., Locatelli, R., Machida, T., Maksyutov, S., McDonald, K.C., Marshall, J., Melton, J.R., Morino, I., Naik, V., O'Doherty, S., Parmentier, F.J.W., Patra, P.K., Peng, C., Peng, S., Peters, G.P., Pison, I., Prigent, C., Prinn, R., Ramonet, M., Riley, W.J., Saito, M., Santini, M., Schroeder, R., Simpson, I.J., Spahni, R., Steele, P., Takizawa, A., Thornton, B.F., Tian, H., Tohjima, Y., Viovy, N., Voulgarakis, A., Van Weele, M., Van Der Werf, G.R., Weiss, R., Wiedinmyer, C., Wilton, D.J., Wiltshire, A., Worthy, D., Wunch, D., Xu, X., Yoshida, Y., Zhang, B., Zhang, Z., Zhu, Q., 2016. The global methane budget 2000-2012. Earth Syst. Sci. Data 8, 697–751. https://doi.org/10.5194/essd-8-697-2016

Saunois, M., Jackson, R.B., Bousquet, P., Poulter, B., Canadell, J.G., 2016. The growing role of methane in anthropogenic climate change. Environ. Res. Lett. 11. https://doi.org/10.1088/1748-9326/11/12/120207

Schneider, P., Castell, N., Vogt, M., Dauge, F.R., Lahoz, W.A., Bartonova, A., 2017. Mapping urban air quality in near real-time using observations from low-cost sensors and model information. Environ. Int. 106, 234–247.

Schulte, N., Snyder, M., Isakov, V., Heist, D., Venkatram, A., 2014. Effects of solid barriers on dispersion of roadway emissions. Atmos. Environ. 97, 286–295. https://doi.org/10.1016/j.atmosenv.2014.08.026

Shancita, I., Masjuki, H.H., Kalam, M.A., Fattah, I.M.R., Rashed, M.M., Rashedul, H.K., 2014. A review on idling reduction strategies to improve fuel economy and reduce exhaust emissions of transport vehicles. Energy Convers. Manag. 88, 794–807. https://doi.org/10.1016/j.enconman.2014.09.036

Siddans, R., Smith, A., 2018. Sentinel-5 precursor/TROPOMI Level 2 Product User Manual NPP Cloud 74.

Sifakis, N., Soulakellis, N., Sarigiannis, D., Tombrou, M., Schaefer, K., 2003. High spatial resolution satellites as a complement to atmospheric modeling and to ground

measurements for air-quality monitoring. Remote Sens. Clouds Atmos. VII 4882, 532. https://doi.org/10.1117/12.463725

Snyder, M.G., Venkatram, A., Heist, D.K., Perry, S.G., Petersen, W.B., Isakov, V., 2013. RLINE: A line source dispersion model for near-surface releases. Atmos. Environ. 77, 748–756. https://doi.org/10.1016/j.atmosenv.2013.05.074

Steiner, S., Bisig, C., Petri-Fink, A., Rothen-Rutishauser, B., 2016. Diesel exhaust: current knowledge of adverse effects and underlying cellular mechanisms. Arch. Toxicol. 90, 1541–1553. https://doi.org/10.1007/s00204-016-1736-5

Thiruvenkatachari, R.R., Ding, Y., González-Rocha, J., Carranza, V., Rojas Robles, N., Hopkins, F., Venkatram, A., 2023. Estimating inputs for dispersion modeling in mobile platform applications. Sci. Total Environ. 881. https://doi.org/10.1016/j.scitotenv.2023.163306

Thiruvenkatachari, R.R., Ding, Y., Pankratz, D., Venkatram, A., 2022. A field study to estimate the impact of noise barriers on mitigation of near road air pollution. Air Qual. Atmos. Heal. 15, 363–372. https://doi.org/10.1007/s11869-021-01104-9

Thorpe, A.J., Harrison, R.M., Boulter, P.G., McCrae, I.S., 2007. Estimation of particle resuspension source strength on a major London Road. Atmos. Environ. 41, 8007–8020. https://doi.org/10.1016/j.atmosenv.2007.07.006

Thorpe, A.K., Frankenberg, C., Green, R.O., Thompson, D.R., Aubrey, A.D., Mouroulis, P., Eastwood, M.L., Matheou, G., 2016. The Airborne Methane Plume Spectrometer (AMPS): Quantitative imaging of methane plumes in real time. IEEE Aerosp. Conf. Proc. 2016-June. https://doi.org/10.1109/AERO.2016.7500756

Ulfvarson, U., Alexandersson, R., Aringer, L., Svensson, E., Hogstedt, C., Holmberg, B., Rosén, G., Sorsa, M., Scandinavian, S., Ulfvarson, U., Alexandersson, R., Aringer, L., Svensson, E., Hedenstierna, G., Hogstedt, C., Holmberg, B., Rosen, G., 1987. Effects of exposure to vehicle exhaust on health Published by : the Scandinavian Journal of Work , Environment & Health , the Finnish Institute of Occupational Health , the Danish National Research Centre for the Working Environment , and the Norwegian Na 13, 505–512.

US-EPA, 2017. Annexes to the inventory of U.S. GHG emissions and sinks. U.S. Environmental Protection Agency. Inventory of U.S. Greenhouse gas emissions and sinks: 1990-2015.

US EPA, 2023a. Criteria Air Pollutants [WWW Document]. URL https://www.epa.gov/criteria-air-pollutants

US EPA, 2023b. Particulate Matter (PM) Basics [WWW Document]. URL https://www.epa.gov/pm-pollution/particulate-matter-pm-basics#:~:text=Particulate matter contains microscopic solids,even get into your bloodstream.

US EPA, 2023c. Health and Environmental Effects of Particulate Matter (PM) [WWW Document]. URL https://www.epa.gov/pm-pollution/health-and-environmental-effects-particulate-matter-pm

US EPA, 2023d. Smog, Soot, and Other Air Pollution from Transportation [WWW Document]. URL https://www.epa.gov/transportation-air-pollution-and-climate-change/smog-soot-and-other-air-pollution-transportation

US EPA, 2022. The 2022 EPA Automotive Trends Report: Greenhouse Gas Emissions, Fuel Economy, and Technology since 1975 (EPA-420-R-22-029, December 2022) 1–158.

US EPA, 2019. EPA Tools and Resources Webinar FRMs/FEMs and Sensors: Complementary Approaches for Determining Ambient Air Quality.

US EPA, 2018. Greenhouse Gas Emissions from a Typical Passenger Vehicle (EPA-420-F-18-008, April 2018) 1–5.

US EPA, 2016. Population and Activity of On - road Vehicles in MOVES2014.

US EPA, 2011a. AP-42 Background Documentation.

US EPA, 2011b. AP 42 Chapter 13: Miscellaneous Sources, English.

US EPA, 1995. Procedures for laboratory analysis of surface/bulk dust loading samples.

US EPA, 1993. Procedures for Sampling Surface/Bulk Dust Loading.

Van Donkelaar, A., Martin, R. V., Park, R.J., 2006. Estimating ground-level PM<inf>2.5</inf> using aerosol optical depth determined from satellite remote sensing. J. Geophys. Res. Atmos. 111, 1–10. https://doi.org/10.1029/2005JD006996

Varon, D.J., Jacob, D.J., McKeever, J., Jervis, D., Durak, B.O.A., Xia, Y., Huang, Y., 2018. Quantifying methane point sources from fine-scale satellite observations of atmospheric methane plumes. Atmos. Meas. Tech. 11, 5673–5686. https://doi.org/10.5194/amt-11-5673-2018

Varon, D.J., McKeever, J., Jervis, D., Maasakkers, J.D., Pandey, S., Houweling, S., Aben, I., Scarpelli, T., Jacob, D.J., 2019. Satellite Discovery of Anomalously Large Methane Point Sources From Oil/Gas Production. Geophys. Res. Lett. 46, 13507–13516. https://doi.org/10.1029/2019GL083798

Venkatram, A., 2008. Computing and displaying model performance statistics. Atmos. Environ. 42, 6862–6868. https://doi.org/10.1016/j.atmosenv.2008.04.043

Venkatram, A., 1988. on the Use of Kriging in the Spatial-Analysis of Acid Precipitation Data. Atmos. Environ. 22, 1963–1975. https://doi.org/10.1016/0004-6981(88)90086-8

Venkatram, A., Burns, L., Chen, C., Irwin, J., Johnson, M., 1998. Model testing and evaluation, in: Reinert, KH and Bartell, SM and Biddinger, GR (Ed.), ECOLOGICAL RISK ASSESSMENT DECISION-SUPPORT SYSTEM: A CONCEPTUAL DESIGN, SETAC SPECIAL PUBLICATIONS SERIES. pp. 39–44.

Venkatram, A., Fitz, D., Bumiller, K., Shuming, D., Boeck, M., Ganguly, C., 1999. Using a dispersion model to estimate emission rates of particulate matter from paved roads. Atmos. Environ. 33, 1093–1102. https://doi.org/10.1016/S1352-2310(98)00316-1

Venkatram, A., Heist, D., Isakov, V., Perry, S., Petersen, W., 2011. Development and evaluation of a model for dispersion of emissions from roads, in: HARMO 2011 - Proceedings of the 14th International Conference on Harmonisation within Atmospheric Dispersion Modelling for Regulatory Purposes.

Venkatram, A., Horst, T.W., 2006. Approximating dispersion from a finite line source. Atmos. Environ. 40, 2401–2408. https://doi.org/10.1016/j.atmosenv.2005.12.014

Venkatram, A., Princevac, M., 2008. Using measurements in urban areas to estimate turbulent velocities for modeling dispersion. Atmos. Environ. 42, 3833–3841. https://doi.org/10.1016/j.atmosenv.2007.12.061

Venkatram, A., Schulte, N., 2018. Urban Transportation and Air Pollution, Elsevier. Joe Hayton.

Venkatram, A., Snyder, M., Isakov, V., Kimbrough, S., 2013a. Impact of wind direction on near-road pollutant concentrations. Atmos. Environ. 80, 248–258. https://doi.org/10.1016/j.atmosenv.2013.07.073

Venkatram, A., Snyder, M.G., Heist, D.K., Perry, S.G., Petersen, W.B., Isakov, V., 2013b. Re-formulation of plume spread for near-surface dispersion. Atmos. Environ. 77, 846–855. https://doi.org/10.1016/j.atmosenv.2013.05.073

Venkatram, A., Snyder, M.G., Heist, D.K., Perry, S.G., Petersen, W.B., Isakov, V., 2013c. Re-formulation of plume spread for near-surface dispersion. Atmos. Environ. 77, 846–855. https://doi.org/10.1016/j.atmosenv.2013.05.073

Viatte, C., Lauvaux, T., Hedelius, J.K., Parker, H., Chen, J., Jones, T., Franklin, J.E., Deng, A.J., Gaudet, B., Verhulst, K., Duren, R., Wunch, D., Roehl, C., Dubey, M.K., Wofsy, S., Wennberg, P.O., 2017. Methane emissions from dairies in the Los Angeles Basin. Atmos. Chem. Phys. 17, 7509–7528. https://doi.org/10.5194/acp-17-7509-2017

Weitekamp, C.A., Kerr, L.B., Dishaw, L., Nichols, J., Lein, M., Stewart, M.J., 2020. A systematic review of the health effects associated with the inhalation of particle-filtered and whole diesel exhaust. Inhal. Toxicol. 32, 1–13. https://doi.org/10.1080/08958378.2020.1725187

Wu, G., Zhao, X., Hao, P., Luo, J., Ding, Y., 2022. Quantifying the Environmental and Health Impacts of Curbside Management for Emerging Multimodal Mobility Services.

Wu, J., M Winer, A., J Delfino, R., 2006. Exposure assessment of particulate matter air pollution before, during, and after the 2003 Southern California wildfires. Atmos. Environ. 40, 3333–3348. https://doi.org/10.1016/j.atmosenv.2006.01.056

Wunch, D., Toon, G.C., Sherlock, V., Deutscher, N.M., Liu, C., Feist, D.G., Wennberg, P.O., 2015. Documentation for the 2014 TCCON Data Release (Version GGG2014. R0), CaltechDATA.

Youssouf, H., Liousse, C., Roblou, L., Assamoi, E., 2014. Non-Accidental Health Impacts of Wildfire Smoke 11772–11804. https://doi.org/10.3390/ijerph111111772

Yura, E.A., Kear, T., Niemeier, D., 2007. Using CALINE dispersion to assess vehicular PM2.5 emissions. Atmos. Environ. 41, 8747–8757. https://doi.org/10.1016/j.atmosenv.2007.07.045

Zhang, W., Ji, Y., Zhang, S., Zhang, L., Wang, S., 2017. Determination of silt loading distribution characteristics using a rapid silt loading testing system in Tianjin, China. Aerosol Air Qual. Res. 17, 2129–2138. https://doi.org/10.4209/aaqr.2016.12.0593